REVIEW

Check for updates

Strategically engineering 2D MXene-based advanced adsorbents for sustainable wastewater remediation of dyes

Sahil Kohli, [ID] *†[a] Garima Rathee, [ID] †[b] Indrani Jha,[a] Lakshita Phor,[c] Harsh Sable [ID] [d] and Vishal Chaudhary [ID] *[e]

The exponential growth of the global population in the digital era has accelerated urbanization and industrialization, leading to severe complex water pollution from the discharge of toxic dyes into aquatic ecosystems. Two dimensional (2D) MXene-based nano-adsorbents recently emerged as promising candidates for developing sustainable wastewater remediation technologies due to their tunable physicochemical properties, including a high negative zeta potential, a large specific surface area, exceptional adsorption capacity, superior electrical and thermal conductivity, hydrophilicity, and rich surface chemistry. Strategic optimization approaches for MXenes, encompassing interlayer spacing modification, surface engineering, stoichiometric tuning, morphological control, bandgap engineering, membrane fabrication, hybridization, and functionalization, have significantly enhanced their adsorptive performance and dye removal efficiency for real-time wastewater treatment applications. This comprehensive review examines the latest advances in MXene-based nano-adsorbent engineering and their implementation as key components in wastewater treatment strategies for efficient dye removal from industrial effluents, providing fundamental insights into dye−MXene interactions to elucidate underlying complex removal mechanisms. The review highlights the sustainable characteristics of MXene-based nano-adsorbents, including their dye removal capacity, regeneration potential, recyclability, catalytic efficiency, and enhanced physicochemical properties, while addressing critical challenges, such as toxicity concerns, biocompatibility issues, and scalability limitations, that currently hinder their translation from the laboratory to the market. Innovative solutions are proposed through the integration of digital-age technologies, particularly artificial intelligence and machine learning approaches, with the implementation of these recommendations facilitating the establishment of MXene-based nano-adsorbents as sustainable alternatives to conventional commercial adsorbents. This aligns with the UN's Sustainable Development Goals and contributes to the principles of One Health, promoting global welfare.

1. Introduction

As industrialization progresses rapidly to cater to the needs of future generations, there is improper discharge of toxic pollutants from industrial settings, resulting in serious global One Health threats, including water pollution and damage to human health. In accordance with the World Health Organization (WHO), environmental contamination impairs the human respiratory, neurological, and immune systems, making people more susceptible to serious diseases, including monkeypox, coronavirus disease (COVID-19), and cancer. As a result, legislators, environmentalists, researchers, and industrialists have expressed concern about the need for environmental rehabilitation. It can be accomplished by monitoring and managing various contaminants (air, water, radiation, and solid) using specific methodologies.[1–6] Chemical water contaminants are classified as organic and inorganic pollutants. The former come primarily from human activity, such as sewage plants, agricultural runoff, and industrial effluents. Dye compounds are among the organic pollutants, while radionuclides and heavy metal ions are the most frequent inorganic

[a]*Department of Chemistry, School of Engineering and Technology, Manav Rachna International Institute of Research and Studies, Faridabad, Haryana-121004, India. E-mail: sahilkohli41@gmail.com, sahil.set@mriu.edu.in*

[b]*Department of Chemical Engineering, Universitat Politècnica de Catalunya, Barcelona, Spain*

[c]*Centre for Research Impact & Outcome, Chitkara University Institute of Engineering and Technology, Chitkara University, Rajpura 140401, Punjab, India*

[d]*School of Life and Applied Sciences, Maya Devi University, Dehradun, Uttarakhand-248011, India*

[e]*Centre for Theoretical Physics and Natural Philosophy, Nakhonsawan Studiorum for Advanced Studies, Mahidol University, Nakhonsawan, 60130, Thailand. E-mail: vishal.cha@mahidol.ac.th*

†Equal authorship: SK and GR.

pollutants found in water. These contaminants are mostly discharged by paper, paint, and textile factories. Most of these industries frequently discharge their effluent into water bodies, which can lead to several issues, including decreased solar penetration into the marine ecosystem, genotoxicity, carcinogenicity, and adverse effects on human wellness, habitats, and marine life.[7–10] Harmful molecules of dyes in water lead to mutagenicity, and the disruption of the main human tissues such as the liver, kidneys, reproductive system, and central nervous system.[11] As a result of industrial and human activity, dyes are regarded as dangerous pollutants since they can be found in surface water.[12] To protect the environment, it is crucial to eliminate these harmful toxins from the aquatic environment.[13]

Various technologies have been established in the past few years to effectively remove dye pollutants from water, including advanced oxidation,[14–16] catalytic ozonation,[17] flocculation and coagulation,[18] Fenton oxidation and electrocoagulation,[19] ion exchange,[20] membrane separation,[21] and photocatalysis.[22,23] These approaches have certain drawbacks (Fig. 1), including the production of contaminated sludge, difficulties with disposal and handling, scaling up problems, high energy consumption, increased colouration of effluents, financial constraints, intricate and complex removal mechanisms, clogged membranes, restricted flow rates, and the production of byproducts.[24]

Among these methods, adsorption is considered to be an effective substitute technique for de-colorizing wastewater owing to its easy handling, affordability, sustainability, and quick water treatment.[25–32] Furthermore, during the regeneration process, adsorption stops the creation of hazardous chemicals, which result in prevention from secondary contamination. For efficient adsorption, adsorbents with appropriate functionality and large surface areas are usually utilized for the adsorption process. A few porous materials such as MOFs, activated carbon, zeolites, chitosan, and kaolinite were prepared as adsorbents for environmental contaminants.[33,34] Hydrogel materials are also used as a superior adsorbent for the elimination of water-based contaminants.[35,36]

The research community has shown substantial interest in 2D materials owing to their distinct chemical and physical properties, which set them apart from their bulk counterparts. This difference became particularly evident after the groundbreaking discovery of graphene through mechanical exfoliation into single layers.[37] Following graphene's discovery, various 2D materials, including metal oxides, metal hydroxides, hexagonal boron nitrides, and TMDs, have been identified and their capability across various applications has been demonstrated.[38–42] These 2D materials are low-dimensional materials possessing enormous surface areas and have been recognized as the best adsorbents for a variety of con-
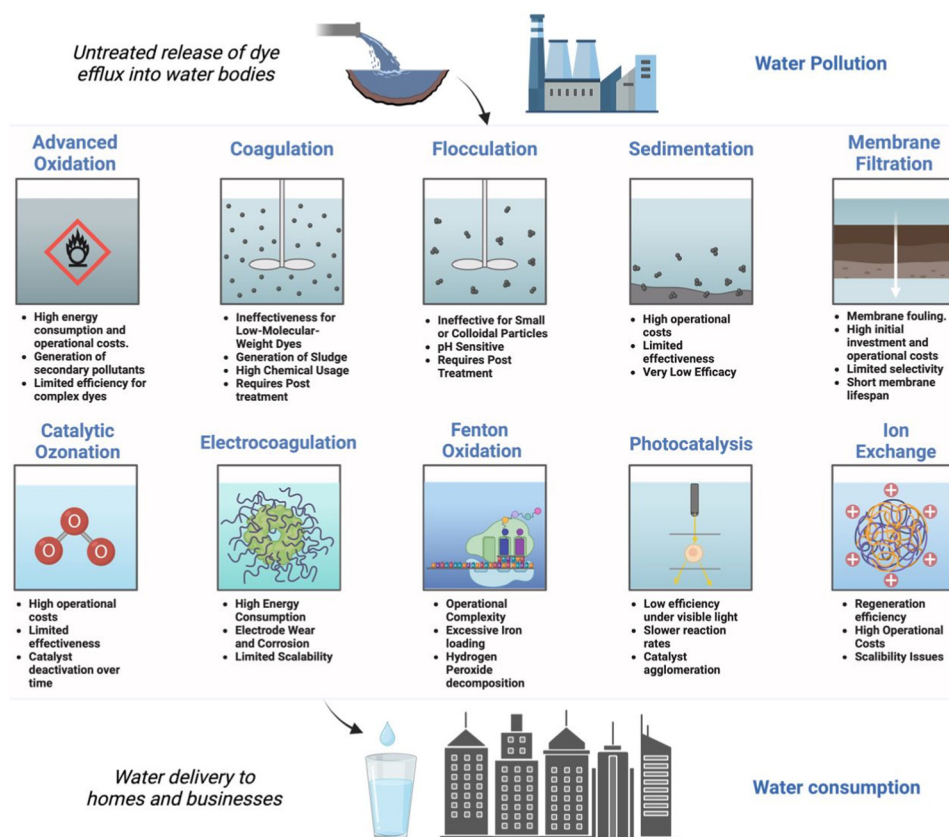

Fig. 1 Drawbacks of traditional methods employed for dye removal.

taminants. Examples of these materials include carbon-based nanomaterials such as graphene, ordered mesoporous silica, and phosphorenes.[43–45]

A number of nanomaterials have lately shown great potential in water purification due to their notable physicochemical properties. Among them, MXenes is an innovative family of cutting-edge nanomaterials with promising applications in water remediation. They are also referred to as 2D transition metal carbides, carbonitrides or nitrides. MXene's unique design, fine structure, remarkable stability, notable oxidation and chemical resistance, high conductivity, and environmental friendliness increased the curiosity of researchers recently.[46] They are ideal candidates for use in wastewater treatment applications due to their enhanced surface area and the availability of several functional groups, such as –OH and –O, on the MXene surface.[47] Their varied chemical composition, photocatalytic capabilities, 2D layered architecture, and active metallic hydroxide sites have made these materials stand out as excellent candidates for use in water purification systems.[48] MXene-based materials are also very useful in the adsorption of various organic dyes, which are toxic to the environment. Additionally, MXenes serve as raw materials for the fabrication of nanostructured MXene membranes, demonstrating beneficial usage in wastewater treatment methods.[49,50]

This review article addresses the potential use of MXenes, 2D transition metal carbides and nitrides in improving dye adsorption for wastewater treatment. MXenes are characterized by their unique surface chemistry, increased surface area, and superior conductivity, which make them a vital choice for eliminating hazardous dyes from industrial effluents. In this article, advancements in MXene-based adsorbents, including their physicochemical features, adsorption mechanisms that improve the efficacy of MXenes in dye removal operations, and the design and techniques for synthesizing for these adsorbents are discussed. Additionally, it highlights recent progress in integrating MXenes into composite materials and membrane systems to optimize performance. Furthermore, the regeneration, recyclability, challenges and recommendations are also addressed for a sustainable environment. This review explores the viability of MXenes as an eco-friendly and sustainable approach for water remediation, paving the way for future investigations and the expansion of sustainable wastewater management technologies.

2. Engineering structural and physicochemical properties of MXenes and related nanosorbents employed for dye removal

2.1. Fundamental structures of MXenes and their nanoadsorbents

MXenes are derived from MAX phases, which are ternary compounds of carbides or nitrides. They have the common formula $M_{n+1}AX_n$, where M signifies a transition metal (Cr, Ti), A corresponds to an element from either group 13 or 14 of the periodic table (e.g., Si, Al), X indicates nitrogen or carbon and n is typically 1, 2, or 3. These phases are characterized by densely arranged M layers, with X atoms occupying the octahedral sites within the layered hexagonal MAX phases. However, strong acids can easily etch away the A-layer due to the greater strength of M–X bonds compared to M–A bonds. After etching, the resulting MXene can be expressed as $M_{n+1}X_nT_x$, where T signifies surface terminal groups such as –OH, –O, and –F, and so on, and x is the termination number. This 2D material, which shares similarities with graphene, was given the name "MXene" because of its structure. The suffix "-ene" is taken from the word "graphene", while "MX" is derived from the material's structure. Additionally, there are a lot of edges and void spaces between the various layers, which help adsorbates to diffuse and enable integration with nanomaterials or polymers. Examples of widely used MXenes are Mo_2CT_x, T_2CT_x, $T_3C_2T_x$, and so on.[51]

The fundamental MAX phase and MXenes have the same hexagonal crystal structure. Typically, MAX phases are expressed as $M_{n+1}AX_n$ (n = 1–3), which yields M_2AX (211), M_3AX_2 (312), and M_4AX_3 (413) (Fig. 2a).[52,53] The "X" atoms fill the octahedral spaces created by the arrangement of "M" atoms of the transition metal organizing into octahedra in all MAX phases, resulting in M_6X interspersed with "A" element sheets and M_6X overlapping with "A" element sheets.[54] The only thing that separates the (211), (312), and (413) phases are the numbers of M atom layers between A atom layers. Conclusively, the MAX phase consists of alternating layers of MX and A. Ti_3AlC_2 has a unit cell that resembles a hexagon and a five-atomic sheet structure. Among the five atomic sheets, three Ti sublayers containing carbon atoms are located at the "octahedral interstitial sites", and a reactive Al layer links the two adjacent layers. The zone of surface terminating groups, the intralayer skeleton, and the interlayer make up the structure of $Ti_3C_2T_x$.[55]

2.2. Physicochemical properties of MXenes and their nanosorbents

The unique properties of MXene include its tunable high Young's modulus, band gap, and thermal and electric conductivities. Notably, the hydrophilic surfaces of MXenes, characterized by strong metallic conductivities, differentiate themselves from most 2D materials, such as graphene.[56–58] Finally, to optimize the properties and performance of their applications, various strategies can be employed, including (i) composition adjustments (such as the formation of solid solutions and variation of "M" and "X" elements), (ii) surface functionalization (achieved through thermal and chemical treatments), and (iii) structural and morphological modifications.[59–61] The primary features of the MXene family are outlined below.

2.2.1. Mechanical attributes of MXenes for effective adsorption. The mechanical properties of MXenes are crucial for their effectiveness as adsorbents for dye removal. The
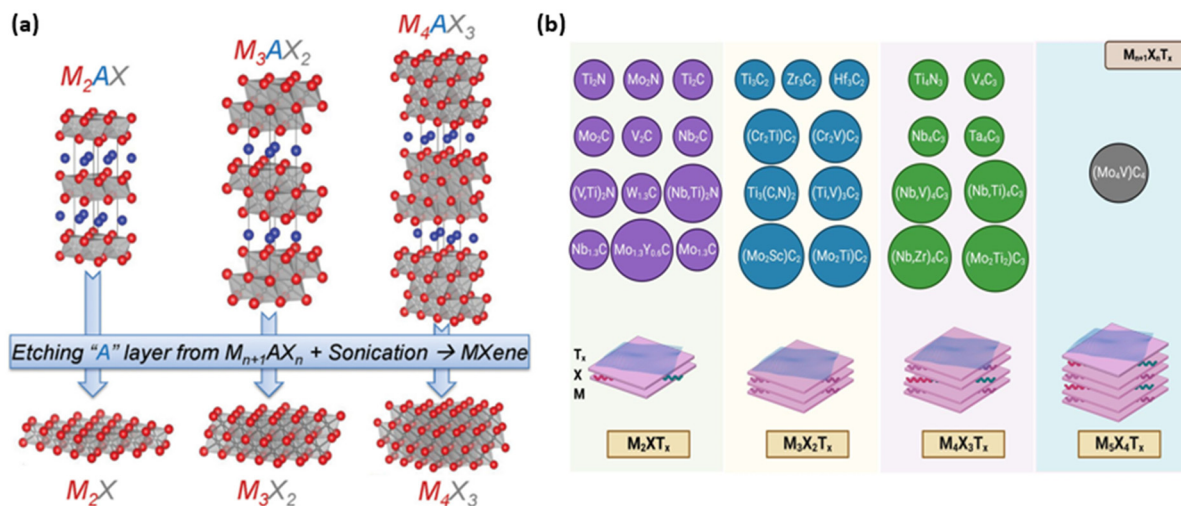
Fig. 2 (a) The structural arrangement of MAX phases and their associated MXenes. Reproduced with permission from ref. 53. Copyright (2013) John Wiley & Sons. (b) Various examples of different MAX phases.

Young's modulus, a critical indicator of mechanical strength, assesses a material's rigidity and its ability to resist elastic deformation. MXenes are widely recognized for their high Young's modulus values, generally spanning from tens to hundreds of gigapascals (GPa). For example, the $Ti_3C_2T_x$ MXene has a Young's modulus of approximately 330 GPa, while other MXenes, such as V_2C and Nb_2C, also exhibit similarly high values.[62] MXene membranes with a tip radius of 7 nm, demonstrate an effective Young's modulus and a tensile strength of 333 ± 30 GPa and 17.3 ± 1.6 GPa, respectively. Additionally, the Young's modulus of Ti_3C_2 is 502 GPa, as determined through molecular dynamics simulations.[63,64] The layer thickness significantly affects the tensile strength of MXenes. Luo *et al.* demonstrated that with increasing the thickness of the MXene film from 2.30 to 17.0 μm, the elastic modulus decreases from 17 GPa to 8 GPa, and the tensile strength reduces from 61 MPa to 36 MPa.[65] In addition to possessing a high Young's modulus, MXenes exhibit robust physical properties. MXenes exhibit tensile strengths typically ranging from several hundred to several thousand megapascals (MPa), indicating considerable robustness. For example, $Ti_3C_2T_x$ MXene is reported to possess a strength of approximately 400 MPa.[66] Liang *et al.* demonstrated that the addition of 3 wt% MXene enhanced the fracture mechanical strength of ceramics by 7.6 MPa m$^{1/2}$, marking a 36% increase compared to unmodified ceramics.[67]

This mechanical robustness is coupled with excellent flexibility due to their layered structure, which enables MXenes to bend and deform without compromising their structural integrity. Such properties are advantageous in wastewater treatment, where maintaining functionality under different conditions is essential. Flexibility is another essential aspect of mechanical behavior. MXenes have a layered structure that imparts a degree of flexibility, allowing them to bend and distort. The specific mechanical properties of MXenes can vary based on factors such as composition, doping, production methods, and the existence of defects or functional groups. Owing to their versatility, MXenes are appealing prospects for application in the adsorption of dyes.[68]

2.2.2. Electronic and electrical properties aiding effective dye removal. MXenes have distinct electronic and electrical properties that greatly improve their efficacy in dye adsorption applications. Modifying the stoichiometry, functional unit, or solid solution formation of MXenes can modify two of their primary attributes of interest: their electric and electronic properties. MXenes' metallic or semi-metallic conductivity allows for quick electron transfer processes, which can increase dye–adsorbent surface interactions. This conductivity facilitates charge transfer, promotes electrostatic interactions, and may improve the adsorption kinetics of anionic or cationic dyes. Experimentally, the pressed MXene discs exhibited electrical conductivities comparable to those of multi-layered graphene (with resistance varying from 22 to 339 Ω, based on the chemical formula and '*n*' index) and surpassed those of reduced graphene oxide (rGO) and CNTs.[53,69] Furthermore, the values of resistivity were found to increase with the functional groups and number of layers.[56,70,71] The calculated conductivities typically exhibit higher values than those measured experimentally.[72]

The electrical conductivity of $Ti_3C_2T_x$ ranged from 850 to 9880 S cm^{-1}, which could be attributed to variations in (i) defect concentration, (ii) surface functional groups, (iii) delamination yield, (iv) *d*-spacing between MXene flakes, and (v) lateral diameters influenced by the etching technique used.[73,74] Generally, reduced HF content and etching durations produce MXenes with fewer flaws and larger lateral dimensions, resulting in enhanced electronic conductivity (for instance, bigger flake sizes yielded conductivities five times greater than those of smaller MXenes).[75] Furthermore, environmental humidity may affect their conductivities,[76] indi-

cating potential application for relative humidity sensing materials.[77,78] An effective method to improve electrical characteristics is surface modification using alkaline and thermal treatments. They demonstrate conductivities that rise by up to two orders of magnitude. This augmentation results from the modification and/or elimination of functional groups and embedded molecules.[79–81] Also, the functional groups present on the surface might result in localized electronic states, which boost adsorption capacity *via* enhanced chemical interactions. The ability to control these electrical properties *via* chemical modifications or by changing the composition of MXenes enables tailored performances under various dye removal conditions. Overall, the favorable electrical properties of MXenes contribute to their potential as excellent adsorbents in wastewater treatment applications.

2.2.3. Optical attributes aiding effective dye removal efficacies. MXenes have unique optical characteristics that make them ideal for dye adsorption applications. Their metallic conductivity and configurable bandgaps enable efficient interactions with light, making them ideal for photocatalytic reactions. The functional groups present on the MXene surface can also affect light absorption, allowing for selective interactions with certain dyes based on their absorption spectra. Furthermore, the layered structure of MXenes can provide plasmonic effects, which increase the local electromagnetic fields around the material, enabling dye adsorption. This combination of optical features not only improves dye removal effectiveness but also provides opportunities for the development of new materials for environmental remediation and sensing applications.[53,82]

2.2.4. pH-responsive surface chemistry of MXenes and its role in selective dye removal. MXene surface charge behavior and zeta potential variations under different pH conditions represent a critical yet underexplored aspect that significantly influences dye selectivity in adsorption applications. The surface terminations of MXenes (primarily –OH, –O, and –F groups) exhibit pH-dependent protonation and deprotonation behaviors, leading to dynamic changes in surface charge density and zeta potential values. Under acidic conditions, MXenes typically exhibit positive zeta potentials due to the protonation of surface hydroxyl groups, whereas alkaline environments promote deprotonation, resulting in increasingly negative surface charges. This pH-responsive behavior directly governs the electrostatic interactions between MXene surfaces and ionic dyes, where cationic dyes show enhanced adsorption at higher pH values when MXene surfaces are negatively charged, and anionic dyes preferentially adsorb under acidic conditions when surfaces carry positive charges. Despite their fundamental importance for the rational design of selective dye removal systems, systematic investigations correlating MXene surface charge characteristics with dye selectivity mechanisms over comprehensive pH ranges remain limited, representing a significant knowledge gap that hinders optimization of MXene-based water treatment technologies.[61,83,84]

2.2.5. Adsorptive attributes of MXenes and nanosorbents make them ideal adsorbents. The adsorption properties influ-ence the performance of MXene-based adsorbents in removing colors from mixtures. Factors such as hydrophilicity, specific surface area (SSA), toxicity, porosity, uniformity, and various functional groups on the MXene adsorbent surface are key determinants in the adsorption of dyes.

2.2.5.1. Enlarged specific surface area for high adsorption. Adsorption is often a surface process; thus, as an adsorbent's SSA increases, the number of pollutants absorbed also increases. By increasing the surface area, several more active sites might be accessible for the likely adsorption of dyes. Usually, a large SSA provides additional active sites dedicated to the adsorption of pollutants, leading to a higher adsorption capacity. The large SSAs and negative surfaces of MXenes have made it possible for them to demonstrate possible adsorption capabilities.[85]

2.2.5.2. Abundant surface functional groups for better adsorption. The functional groups on MXene-derived adsorbents, which are readily available, can significantly contribute to the removal of dyes from aquatic environments. This is due to the robust binding interactions between the molecules of the cationic dye and the negatively charged functional moieties on the MXene adsorbents. These interactions frequently lead to an increase in the amount of dye that is taken up by the adsorbents. Similarly, the existence of surface-bound positive functional groups on MXene-derived adsorbents promotes the adsorption of anionic dyes through electrostatic interactions (attractive) between oppositely charged species. Since different surface functional moieties give MXenes with different chemical and physical features, their availability plays a significant part in the utilization of MXene-based adsorbents. Additionally, the molecular intercalation of cations or tiny organic interlayer spacing also enhance the material's capacity for adsorption as MXene adsorbents. The increased interlayer space can explain this; consequently, increased analyte exposure occurs with interlayer gaps and functional divisions.[86]

2.2.5.3. Significant wettability aiding efficient adsorption. Another aspect that substantially affects an adsorbent surface's power for adsorption is its wettability. The wettability of MXene-based adsorbents can significantly influence selective dye uptake. The wet etching technique utilizing (*in situ*) hydrogen fluoride is the most widely used synthesis method for producing MXenes. This procedure gives the surface of the 2D sheets a spectrum of O and OH containing moieties, making them hydrophilic.[87] As a result, MXenes show remarkable alignment with the liquid procedure in an aqueous media, underscoring their increased capability for forming material hybrids and managing wettability in systems.[88] Essentially, a liquid droplet's ability to wet the MXene surface depends on the interaction at the solid–liquid phases. Some additional factors that affect this interaction are electrostatic interactions, H-bonding, and van der Waals interactions.

2.2.5.4. Improving stability for practical prospects as nanosorbents. One of the main problems researchers face with MXenes is their stability. Density functional tight-binding calculations, supported by formation and cohesive energy studies as well as

ab initio simulations, have demonstrated that MXenes are stable. Specifically, hydroxylated MXene derivatives with varying atomic distributions of nitrogen (N) and carbon (C) represent stable phases with favorable thermodynamic properties. However, under real reaction conditions, the stability of MXenes and their surface topologies remain unknown.[89] Transition metal-containing layered MXenes have a remarkable combination of excellent metallic conductivity and rich, adaptable surface chemistry. MXenes become thermodynamically metastable as a result of this. Additionally, it is anticipated that MXenes' larger surface energy and low resistance to oxidation in oxygenated aqueous environments, even at room temperature, will lessen the electrical conductivity and passivate the reactive interface.[89] Furthermore, after storing delaminated $Ti_3C_2T_x$ MXene for two weeks, MXenes usually undergo oxidation, such as oxidation of the MXene titania layer to anatase TiO_2, which results in a color shift to off-white from greenish-black.[90] $Ti_3C_2T_x$, on the other hand, was shown to be stable in an argon or hydrogen environment up to 1473 K, demonstrating that it was able to maintain its stability even at higher temperatures.[70] The thermal stability of MXene ($Ti_3C_2T_x$) powders is demonstrated to be as low as 200 °C in oxygen, and as high as 800 °C under an argon atmosphere. At 200 °C in oxygen, the MXene surface oxidizes to produce amorphous carbon and anatase TiO_2.[70,91] Initially, the surfaces of MXene oxidize to form anatase crystals, preventing further oxidation. Then, as a result of anatase's enhanced O_2 diffusion, the leftover MXene was gradually oxidized at higher temperatures until anatase converted all of the MXene into CO_2, TiO_2, and rutile.[70]

2.2.5.5.   Toxicity related to MXene nanosystems. The toxicity profile of titanium-based MXenes presents a complex landscape requiring comprehensive evaluation across multiple biological systems and temporal scales. While non-toxic degradation products including C, N, and Ti break down into CO_2, N_2, and Ti compounds that are safe in trace amounts,[92] the true group toxicity of MXenes remains challenging to ascertain due to their varied compound classes and significant heterogeneity in X or M elements and surface chemistry (T_x).[93] $Ti_3C_2T_x$ demonstrates concentration-dependent cytotoxicity with differential effects on normal *versus* cancerous cell lines. Studies reveal higher toxicity against cancerous cells (A549 and A375) compared to normal cell lines (MRC-5 and HaCaT).[94,95] Neural stem cell studies indicate no observable adverse effects at 12.5 μg mL^{-1} but significant cytotoxicity at 25 μg mL^{-1} with compromised cell membrane integrity.[96] The primary toxicity mechanisms involve oxidative stress pathways generating reactive oxygen species (ROS), leading to cellular membrane damage and mitochondrial dysfunction.[97]

Surface termination chemistry significantly influences MXene biocompatibility profiles. Fluorinated $Ti_3C_2T_x$ synthesized *via* conventional HF etching exhibits enhanced cytotoxicity due to fluoride ion release, which promotes ROS generation.[98] Halogen-free $Ti_3C_2T_x$ produced through NaOH-based etching demonstrates superior biocompatibility with no noticeable cytotoxicity even at high concentrations. PEGylation alters protein corona formation and cellular take up mechanisms, with PEGylated MXenes showing modified biocompatibility profiles.[99]

Environmental persistence studies reveal $Ti_3C_2T_x$ stability in aquatic media for at least 4 days at concentrations of 5–20 mg L^{-1}, with no dissolution detected over 42 days.[100] Aquatic organism studies using zebrafish embryo models indicate LC_{50} values of 257.46 μg mL^{-1}, classifying $Ti_3C_2T_x$ as "practically non-toxic" under acute exposure conditions.[101] However, chronic exposure effects including developmental abnormalities and behavioral changes remain poorly characterized. Metabolomic analysis in *Daphnia magna* reveals metabolic disruption at sublethal concentrations, indicating potential ecosystem-level impacts.[102] The environmental behavior of MXenes involves complex transformation pathways influenced by water chemistry and redox conditions. Aggregation processes in natural waters alter bioavailability, while photodegradation generates titanium dioxide nanoparticles with unknown ecological implications.[100] Oxidative degradation over weeks to months may produce metabolites with different toxicity profiles compared to parent materials.

Comprehensive safety assessment using the safe and sustainable by design (SSbD) framework suggests $Ti_3C_2T_x$ can be safe and sustainable when properly designed and applied.[100] Life cycle assessment (LCA) studies identify synthesis impacts as major environmental concerns, particularly titanium precursor production and hazardous chemical usage.[103] Green synthesis alternatives using electrochemical etching reduce the environmental impact but require systematic toxicity evaluation. Current regulatory frameworks lack MXene-specific guidelines, creating knowledge gaps for commercial applications. Standardized testing protocols addressing unique physicochemical properties are needed for comprehensive risk assessment. Risk mitigation strategies include surface engineering for reduced toxicity, biocompatible coating systems, and real-time monitoring for environmental release detection. Critical research needs include long-term exposure studies, mechanistic toxicology investigations, and ecosystem-level impact assessments. Predictive toxicology models incorporating machine learning approaches can accelerate safety evaluation while reducing animal testing requirements. Integration of advanced characterization techniques will provide mechanistic insights that are essential for safe-by-design approaches.

3.   Methods for the synthesis of MXenes and their nanosorbents for dye removal

Most MXenes originate from the MAX phase, in which A atoms are embedded in MX layers while M and X atoms are positioned at the hexagonal crystal's centre and apex, respectively. After eliminating A atoms from MAX phases, MX layers could be maintained by utilizing this "laminar" structure. However, unlike graphene, which relies on weak van der Waals forces to

preserve the structure, the strong interlayer bonding in MXenes prevents mechanical exfoliation, making it impossible to produce 2D MXenes through this method.[104] Numerous methods have been introduced so far to prepare MXenes, which have numerous advantages and disadvantages (Fig. 3).

3.1. Top-down approaches

Utilizing precursors is a key part of the top-down technique for the synthesis of MXenes. Although $ScAl_3C_3$, $Hf_3(Al, Si)_4C_6$, and $Zr_3Al_3C_5$, are examples of non-MAX structures, Ti_3AlC_2 and Ti_2AlC are examples of structures that are frequently found in MAX. At the moment, MAX is the precursor that is used most frequently in the production of MXenes. In the MAX phase, the strength of M–X bonds is greater than that of M–A bonds. Multi-layered MXenes are produced as a result of breaking of the M–A connection in MAX during the synthesis process. This also results in element A being etched away from the parent structure. These multilayered MXenes are subsequently delaminated to yield single-layered MXenes. MXene's surface produces terminal groups like –OH, –F, and –O, to stabilize its structure. Mechanical stripping is commonly used in top-down methods of synthesis for 2D materials. Mechanical stripping alone is ineffective at breaking the precursor material's M–A bonds. Consequently, chemical stripping is the method of choice for the production of MXenes, whereas mechanical stripping is solely utilized for the production of single-layered MXenes by the manufacturer. Various etching methods can disrupt M–A bonds: electrochemical, alkali bases, fluorides, and Lewis acid molten salts.

3.1.1. HF/*in situ* HF-etching method. The two primary methods for preparing MXene are HF and *in situ* HF-etching (Fig. 4a).[105] The loosely layered accordion-like MXene structure was initially described by Gogotsi and colleagues, who selectively etched Al from bulk Ti_3AlC_2 in HF solution (50 wt%).[106] HF broke the Ti–Al bonds in the Al layers, dissolving them and

releasing a high volume of H_2. As a result, the reaction started off with a powerful bubbling phenomenon. Additionally, a large number of functional moieties, like –F, –OH, and –O moieties, were joined to the surface of Ti atoms, giving rise to high hydrophilicity and distinctive electrochemical properties. Following this, HF etching was used to successfully exfoliate Ti_2CT_x, V_2CT_x, and Mo_2CT_x.[107–109] It should be mentioned that the MAX phase's structural characteristics determine the etching conditions. Ti_2CT_x only needed to be treated for 10 h in 40 wt% HF, but Nb_2AlC needed 90 h of etching time in 50 wt% HF. The outcomes were verified using theoretical approaches. The calculation findings confirmed that, in order to etch Al from Nb_2AlC rather than Ti_2AlC, a longer period and greater concentrations of HF solution were required. This is due to the fact that the bond energy of Nb–Al, which is 1.21 eV, is marginally greater than that of Ti–Al, which is 0.98 eV.[110] It is important to note, though, that an overly aggressive etching process will produce more surface flaws, which could adversely affect the characteristics of MXene sheets.[111] Successful Al layer delamination significantly reduces the interlayer force, facilitating the easy separation of MXene layers from their neighbouring ones.

Many attempts have been made to create safer and milder production methods for HF due to its significant toxicity and high danger. Using a combination of HCl and LiF rather than HF solution allowed for the production of few-layer MXene with fewer surface flaws and greater interlayer spacing in 2014.[114] H^+ and F^- were liberated during the etching process to create HF *in situ*. Al atoms were replaced by intercalated metal ions and H_2O molecules, which encouraged the interlayer gap to expand and the interlayer interaction to diminish. Significantly, by adjusting the quantity of LiF and HCl, this new technique made it possible to regulate the size and quality of sheets.[115] The original etchant is also substituted with mixtures of acid (H_2SO_4) and other fluoride salts (KF,

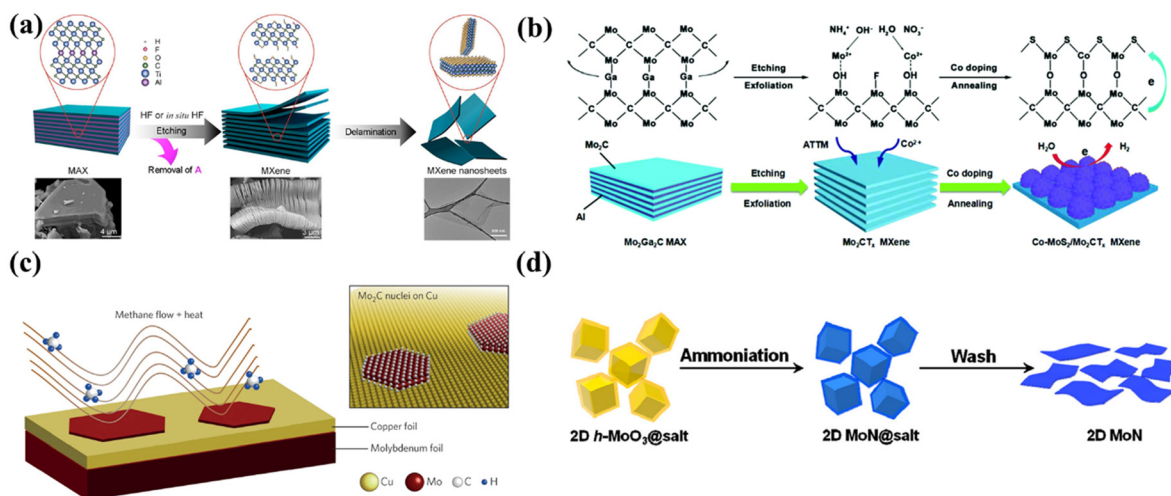**Fig. 3** Advantages and disadvantages of various methods of 2D MXenes.

Fig. 4 (a) Illustration of the process of etching and delamination of MXene. Reproduced with permission from ref. 105. Copyright 2019, Elsevier. (b) Schematic diagram for synthesizing the Co−MoS$_2$/Mo$_2$CT$_x$ nanohybrids. Reproduced with permission from ref. 107. (c) CVD growth of large-area α-Mo$_2$C thin layer on Cu substrate. Reproduced with permission from ref. 112. Copyright 2015, Springer Nature. (d) Schematic of the synthesis of 2D MoN. Reproduced with permission from ref. 113. Copyright 2015, American Chemical Society.

NaF, and CaF$_2$). The presence of –F groups further restricts the application of MXene in electrochemical fields, and the generation of HF cannot be entirely prevented by using these fluorinated salts.[116] Furthermore, a variety of organic compounds, including tetramethylammonium hydroxide (TMAOH) and dimethyl sulphoxide (DMSO), was used as an intercalation agent for converting the multi-layer MXene into a few-layer MXene. The intercalants enable stacked multi-layer MXene to delaminate into a few-layer or monolayer sheet through subsequent shaking or ultrasonication treatment.[71,117]

3.1.2. Molten salt etching method. Both *in situ* HF and HF etching are effective methods for generating carbide MXenes, although they perform poorly when etching nitride MXenes. Two concepts were proposed to illustrate the challenges involved in manufacturing nitride MXenes. Initially, the computational results indicated that Ti$_{n+1}$N$_n$ had a lower cohesive energy than Ti$_{n+1}$C$_n$, indicating lower stability. The energy required to form Ti$_{n+1}$N$_n$ is likewise greater than Ti$_{n+1}$C$_n$, indicating that the Al atoms are firmly bound in the Ti$_{n+1}$AlN$_n$ structure.[118] Gogotsi *et al.* used a combination of molten salts as etchants to produce nitride MXenes to get around these issues.[119] Specifically, Ti$_4$AlN$_3$ was initially mixed with molten salt (29 wt% LiF, 59 wt% KF, 12 wt% NaF) in a mass ratio of 1 : 1, and heated at 550 °C for 30 min under an Ar atmosphere. After that, more washing with H$_2$SO$_4$ and deionised water was needed to eliminate the fluorides that contained aluminum. The prominent broad peak (002) of Ti$_4$N$_3$T$_x$ shifted from 7.6° to 6.3°, as corroborated by XRD data, showing an extended interlayer distance. The EDX results also showed that no Al atoms were seen, indicating that nitride MXenes were successfully etched using the molten salt.

3.1.3. Fluorine-free method. Li and colleagues reported an alkali hydrothermal treatment process that yielded high-purity multilayered MXene without the use of fluorine.[120] Al(oxide)

hydroxides can dissolve completely at high temperatures and concentrations of NaOH. Additional delamination using DMSO or TMAOH together with an ultrasound approach can aid in the production of few-layer MXenes with smaller diameters.[121] In contrast to fluorine-assisted approaches, there are more O-containing groups than –F groups dispersed on the surface, which could improve the electrochemical operation. Treatment with an alkali prevents the production of HF. However, harsh environments might damage the internal structure and increase surface flaws. There is another method for creating MXene sheets besides conventional wet chemical etching, namely, electrochemical etching. Yang and colleagues developed an electrochemical etching technique using an organic mixture of NH$_4$Cl and TMAOH.[122] The counter electrode and working electrode were made of two bulk pieces, and only the working electrode was etched.

Chloride ions functioned as the Ti–Al bond breaker at a constant applied potential of 5 V, and NH$_4$OH that was produced assisted in extending the edges. Compared to conventional HF-etched MXene, the exfoliated sheets had an average lateral size of nearly 2 μm and were primarily single or double layers. Furthermore, Ti$_3$C$_2$T$_x$ sheets synthesized through electrochemical etching often have a stacked architecture that is comparable to that of bulk Ti$_3$AlC$_2$ without exhibiting any obvious expansion. This is due to the fact that the reaction process does not include the release of a significant amount of gas. It should be mentioned that the outcome of etched MXene is also greatly influenced by the choice of electrolytes. For instance, electrochemical treatment in solutions containing NaCl and HCl invariably produces amorphous carbon, which obstructs additional etching.[123] Sun and colleagues discovered that when MAX was treated with 2 M HCl aqueous electrolyte, a three-layer structural composite was produced.[124] The components of this hybrid were unetched MAX, carbon-

|

derived carbides (CDCs), and MXene, which required additional purification in order to get pure MXene sheets.

Above all, using particular etching techniques such as molten salt etching, HF etching, and other fluorine-free approaches, MXenes could be extracted from bulk MAX phases by exploiting the difference in intensities between M–X and M–A bonds. It should be mentioned that the M–A bond energies had a significant impact on the etching conditions, with longer etching times and higher etchant concentrations needed for stronger M–A bonds. Furthermore, the etching rate and reaction conditions are significantly influenced by the size of the MAX particles.[106] Attrition milling of the MAX powder beforehand could significantly cut down on the etching time while maintaining the overall yield.

3.2. Bottom-up approaches

Apart from the etching approach described above, various alternative bottom-up techniques have been developed to build ultrathin 2D highly crystalline MXenes, particularly for Mo$_2$C materials. These techniques include the chemical vapor deposition (CVD) method, template method, and PEPLD.[112,113,125–127]

3.2.1. Chemical vapor deposition method. CVD was utilized by Ren *et al.* to successfully synthesized ultrathin two-dimensional α-Mo$_2$C crystals, a few nanometers thick and with lateral dimensions of up to 100 μm (Fig. 4c). This procedure required the use of methane over a bilayer substrate made of copper and molybdenum foil. Furthermore, this CVD process has been expanded to produce ultrathin TaC and WC crystals from additional transition metals such as Ta and W. Notably, this approach has the benefit of producing MXenes with large lateral diameters and few flaws, which substantially simplifies the analysis of their intrinsic properties.[127] Despite the fact that the fabrication of MXene monolayers has not yet been achieved through this method, it presents the possibility of future research and advancements in bottom-up approaches for the synthesis of MXenes. MXene thickness and form can be controlled very precisely by the use of CVD. On the other hand, this procedure calls for highly specialized machinery and individuals who have received adequate training.[106]

3.2.2. Plasma-enhanced pulsed laser deposition method. The PELPD system is a step up from traditional pulsed laser deposition systems. The initial ultrathin films of Mo$_2$C synthesized using PELPD, made with methane plasma as the source of carbon, interacted with Mo vapor produced by a pulsed laser. Utilizing a sapphire substrate that was heated to 700 °C, this reaction was carried out in order to fabricate films of high-quality with thicknesses that could be altered by modifying the pulse rate of the laser.[113,125]

3.2.3. Template method. To synthesize 2D MoN, a salt-templated technique was employed. In this process, hexagonal 2D NaCl crystals coated with MoO$_3$ were first prepared, and then NH$_3$ was used to ammoniate them at 650 °C (Fig. 4d). As a result, 2D MoN@NaCl powder, in which MoN species combined with the NaCl matrix, were successfully synthesized. 2D nanosheets of MoN were produced by removing NaCl using de-ionized water afterward.[113] The high yield of the template approach is its main benefit over CVD. This method also provides the capacity to precisely regulate the surface functional moieties. It is crucial to recognize that energy input is necessary for the precursor to be converted into nitride or carbide, which adds to energy consumption.[126]

4. Rational engineering of MXene-based materials for enhanced dye removal performance

The rational engineering of MXene-based materials for enhanced dye removal performance represents a systematic approach for designing and optimizing these advanced adsorbents through targeted modifications that address specific limitations and enhance desired properties. As the field of MXene-based water treatment technologies has evolved, researchers have developed sophisticated strategies that go beyond the use of pristine MXenes to fabricate engineered materials with superior performance characteristics. These rational design approaches are guided by a fundamental understanding of structure–property relationships, adsorption mechanisms, and the specific requirements for effective dye removal from aqueous environments. The engineering strategies encompass four primary categories: surface functionalization to introduce particular chemical interactions, interlayer engineering to optimize structural accessibility, composite formation to achieve synergistic effects, and morphological control to enhance practical implementation. Each of these approaches addresses different aspects of the dye adsorption process, from molecular-level interactions to macroscopic material handling and system integration. A comparative analysis of the published literature reveals several vital aspects when examining the efficiency of various MXene-based materials in dye adsorption (Table 1). The information includes adsorption capacity or removal efficiency, experimental conditions, and the type of adsorption isotherms and kinetics models applied for removing different dyes from the aqueous environment using MXene-based materials. This comprehensive evaluation demonstrates that rational engineering approaches have successfully achieved remarkable improvements in adsorption performance, with engineered MXene-based materials exhibiting significantly enhanced adsorption capacities representing orders of magnitude enhancement compared to pristine MXenes. The systematic design and optimization of these materials not only advance our fundamental understanding of MXene chemistry and physics but also provide practical pathways toward the development of commercially viable water treatment technologies capable of addressing the growing global challenge of dye-contaminated wastewater.

4.1. Surface functionalization strategies

Surface functionalization is a key method for improving the adsorption capabilities of MXenes by changing their surface

Table 1 Comparison of different MXene-based materials for adsorption of various dyes

MXene	Dye	Adsorption capacity/% removal efficiency	Experimental conditions	Isotherms/ kinetics	Regeneration	Toxicity evaluation
Ti$_3$C$_2$T$_x$ [128]	MB	39	C_0 (MB) = 0.05 mg mL^{-1}, 25 °C, 20 h	Freundlich	• Ti$_3$C$_2$T$_x$ gradually oxidises to TiO$_2$ and Ti(OH)$_4$ in water, limiting reusability • Structural changes (layer expansion and disorder) occur after 20 h in dye solution • Material is not stable for long-term aqueous applications or storage	• No direct cytotoxicity or ecotoxicity tests were reported • Possible formation of TiO$_2$ NPs and fluoride leaching may raise concerns • Additional studies needed to assess environmental and biological safety
NaOH–Ti$_3$C$_2$T$_x$ [129]	MB	189	25 °C, pH = 6–6.5	Langmuir/ PSO	• No regeneration or reuse tests were conducted	• No cytotoxicity, ecotoxicity, or leaching tests were included
LiOH–Ti$_3$C$_2$T$_x$ [129]	MB	121	25 °C, pH = 6–6.5	Langmuir/ PSO	• Material performance stability over multiple cycles not studied	• Alkaline treatment may reduce fluoride (–F) groups, potentially improving biocompatibility
KOH–Ti$_3$C$_2$T$_x$ [129]	MB	77	25 °C, pH = 6–6.5	Langmuir/ PSO	• Suggests need for future work on recyclability	• Safety and environmental impact not evaluated
h-Ti$_3$C$_2$ [130]	MB	24	2 h	—	• No regeneration, desorption, or reuse cycles were tested or discussed • Long-term stability of the MXenes in dye removal applications not evaluated • Future studies should assess recyclability to validate practical applicability	• No direct toxicity, cytocompatibility, or environmental safety evaluations made • Indirect benefit: hydrothermal route avoids toxic HF, reducing synthesis hazards • Leaching or stability of AlF$_3$ by-products not assessed
Nb$_2$CT$_x$ [131]	MB	526.32	C_0 = 100–500 mg L^{-1}, 25 °C, pH = 7, dose = 1 g L^{-1}, 700 rpm	PSO	• No regeneration/reusability cycles tested • Long-term performance stability and recyclability are not addressed • Future studies should focus on desorption efficiency and material durability	• No toxicity (cytotoxicity or ecotoxicity) or leaching studies reported • HF used for etching may pose safety concerns unless thoroughly washed and neutralised • Environmental and biological safety remain unexplored
PAA$_2$ alk-MXene [132]	MB	193.92	C_0 = 60–90 mg L^{-1}, 25–55 °C, pH = 2–10	Langmuir/ PSO	• The adsorbent AA2-alk-MXene maintained over 85% dye removal efficiency after five adsorption–desorption cycles	• No direct cytotoxicity or ecotoxicity tests were reported in the study
PAA$_2$ alk-MXene [132]	CR	264.46	C_0 = 60–90 mg L^{-1}, 25–55 °C, pH = 2–10	Langmuir/ PSO	• Ethanol was used as the desorbing agent • Good reusability and structural stability	• Use of mild reagents like AA and NaOH suggests potentially low toxicity, although this was not experimentally verified • Biocompatibility and environmental safety remain unexplored
Ti$_3$C$_2$–SO$_3$H [133]	MB	111.11	T = 25 °C, pH = 7, dosage = 10 mg, C_0 = 50 mg L^{-1}	Langmuir/ PSO	• Regeneration or reuse experiments were not conducted • Long-term adsorbent stability was not assessed • No adsorption–desorption cycles reported	• Did not evaluate toxicity, cytotoxicity, or leaching risks • Use of NaF and arenediazonium salts may pose safety concerns • Environmental impact and biocompatibility remain unexplored
MXene-COOH@(PEI/PAA)$_n$ [134]	MB	81.9672	C_0 = 0–3 mg L^{-1}, 25 °C, dose = 10 mg per 50 mL	Langmuir/ PSO	• The removal efficiency decreased from 85.6% to 64.4% after 8 cycles • The material showed good stability and reusability	• Environmental safety and leaching of components were not assessed • The synthesis avoids heavy metals, but toxicity remains unevaluated
PHGC/MXene [135]	MB	555.56	C_0 = 50–100 mg L^{-1}, 298–308 K, pH = 11	Langmuir/ PSO	• PHGC/MXene hydrogel maintained over 90% removal efficiency for AB93 and MB after 12 regeneration cycles • NaHCO$_3$ and HCl were effective desorption agents for AB93 and MB, respectively • The material showed excellent reusability and economic regeneration	• No in vivo or in vitro toxicity studies were reported • Environmental impact and cytocompatibility were not evaluated • Safety validation is lacking for biomedical or large-scale applications
Cetyltrimethylammonium bromide-modified multi-layered Ti$_3$C$_2$T$_x$ MXene (CMM) [136]	MO	213	C_0 = 10–500 mg L^{-1}, 298 K, pH = 3–12, dose = 0–3.33 g L^{-1}	Langmuir/ PSO	• Adsorption capacity decreased slightly from 25.52 mg g^{-1} to 14.3 mg g^{-1} after 5 cycles • Ethanol used for desorption demonstrated effective dye elution • CMM maintained commendable reusability and structural integrity	• No direct toxicity assessment (e.g., cytotoxicity, ecotoxicity) was conducted in the study • Implicit safety suggested via use of ethanol in desorption and absence of harmful leachates

Table 1 *(Contd.)*

MXene	Dye	Adsorption capacity/ removal efficiency %	Experimental conditions	Isotherms/ kinetics	Regeneration	Toxicity evaluation
ABC/MX composite[137]	CR	1103.7	$C_0 = 50$–500 mg L^{-1}, pH = 1–11, 300 K–330 K, dose = 0.4 g L^{-1}	Freundlich model	• CR: high stability and reusability; >95% removal retained after 5 cycles • Cr(vi): performance dropped significantly from 88.44% to 55.53% after 1 cycle	• No *in vitro*, *in vivo*, or ecotoxicity tests were performed • However, authors emphasised that: • Bacterial cellulose (BC) is a renewable, biodegradable, and non-toxic biopolymer • Desorbed Cr(ii) is treated with Fe(ii) to form precipitates, reducing secondary pollution risk • Suggests low environmental burden under controlled usage but lacks direct toxicity proof
MXene-PEI[138]	MO	909.1	$C_0 = 120$–300 mg L^{-1}, 328 K, pH = 3	Langmuir/ PSO	• High stability and reusability over 5 cycles: • MB: removal decreased from 89.7% → 85.3% • Cr(vi): removal decreased from 93.4% → 87.2% • Structural integrity: maintained porous architecture and adsorption capacity	• No *in vitro* or *in vivo* toxicity tests • Materials (MXene, chitosan, alginate) are described as biocompatible and eco-friendly • No harmful by-products or leaching reported • Indicates low environmental impact but lacks formal toxicological validation
MX-PAN membrane[139]	MB	—	$C_0 = 10$ mg L^{-1}, 25 °C, pH = 7	—	• Reusability: • After 5 adsorption–desorption cycles: • Cr(vi): removal decreased from 91.7% to 86.3% • MB: removal declined from 95.4% to 89.5% • Retained adsorption capability and structure, demonstrating excellent recyclability	• No explicit cytotoxicity or environmental toxicity tests conducted • Components (MXene, lignocellulose, CNF) are natural or biocompatible • Emphasis on green synthesis and biodegradability • Suggests low toxicity potential, but lacks empirical toxicology evidence
SA/MXene nanofiber membranes[140]	MB	440	$C_0 = 50$–220 mg L^{-1}, 98 K–323 K, pH = 2–11, dose = 1–5 mg	Langmuir/ PSO	• Performance over cycles: • After 5 adsorption–desorption cycles: • Cr(vi): decreased from 93.6% → 84.7% • MB: decreased from 91.2% → 85.2% • Observation: slight decline but excellent reusability and structural robustness	• No direct cytotoxicity or environmental toxicity data • MXene and attapulgite considered relatively biocompatible materials • Use of mild regenerants (ethanol, NaOH) supports low environmental burden • Long-term stability of MXene against oxidation not discussed in toxicological terms
Ti$_3$C$_2$T$_x$ bound with terephthalate (T-MX)[141]	MB	209	pH = 7, RT, 100 mg L^{-1}	PSO	• Unique regeneration method: spent T-MX (after MB adsorption) is reconverted into MAX phase by adding only Al powder and applying mechanochemical (MC) ball milling • The MAX phase is then re-etched into MXene, confirming the closed-loop recyclability of the material • Pollutants and terephthalate pillars are carbonised and reused as the carbon source in the MAX phase	• No cytotoxicity or environmental safety data were presented • Concerns noted: • Potential contamination from milling tools (Fe, alloying metals) under acidic HF etching • These may bind to reactive Ti sites, requiring further toxicological investigation • Materials used (MXene, terephthalate) are otherwise not inherently toxic, and MC synthesis is solvent-free and greener
TMAOH delaminated Ti$_3$C$_2$T$_x$ MXene nanosheets[142]	MB	1026	$C_0 = 20$–80 mg L^{-1}, 318 K, pH = 6, dose = 0.01–0.06 g L^{-1}	Freundlich/ PSO	• Reusability was tested over 5 cycles using 1 M NaOH for desorption • Stable performance for 3 cycles with no significant loss in adsorption capacity • Slight drop after 3rd cycle likely due to material loss and structural degradation (ultrathin layers disrupted)	• No direct cytotoxicity or ecotoxicity tests were reported • Regeneration using NaOH and sedimentation by flocculation suggest potential for safe separation, but further biological evaluations are necessary for real-world application

Table 1 (Contd.)

MXene	Dye	Adsorption capacity/% removal efficiency	Experimental conditions	Isotherms/kinetics	Regeneration	Toxicity evaluation
MXene/PEI modified sodium alginate aerogel (MPA)[143]	CR	3568	Adsorbent dose: 10 mg	Langmuir/PSO	• MPA demonstrated excellent recyclability with 16.3% capacity loss for Cr(vi) after 5 cycles and only 4.29% loss for CR after 5 cycles	• No toxicity assessment or environmental impact evaluation was conducted in this study • MPA exhibited outstanding antibacterial properties with 99.99% bacterial killing efficiency against both $E.\ coli$ and $S.\ aureus$ after 2 h exposure
alk-MXene/CoFe$_2$O$_4$/CS[144]	MB	537.63	C_0 = 17–50 mg L^{-1}, 22–47 °C, pH = 2–12, dose = 10 mg per 25 mL	Langmuir/PSO	• The adsorbent maintained 83.7% Cr(vi) removal capacity and 95.71% CR removal efficiency after five regeneration cycles using NaOH/NaCl and ethanol desorption methods, respectively	• No toxicity assessment or environmental impact evaluation was conducted in this study
alk-MXene/CoFe$_2$O$_4$/CS[144]	RhB	1333.86	C_0 = 5–10 mg L^{-1}, 22–47 °C, pH = 2–12, dose = 10 mg per 25 mL	Langmuir/PSO	• The adsorbent demonstrated excellent recyclability with >80% removal efficiency maintained for RhB and MG dyes after 5 cycles, while CR retained ~66% efficiency	• The paper focused solely on adsorption performance without investigating potential environmental or health impacts of the synthesized materials
alk-MXene/CoFe$_2$O$_4$/CS[144]	CR	2095.9	C_0 = 5–10 mg L^{-1}, 22–47 °C, pH = 2–12, dose = 10 mg per 25 mL	Langmuir/PSO	• Magnetic separation using NdFeB magnet enabled easy recovery from aqueous solutions, with ethanol used as a desorption agent for regeneration cycles	
MXene (Ti$_3$C$_2$)/Fe$_3$O$_4$[145]	MB	9.85	C_0 = 1–40 mg L^{-1}, 25–55 °C, dose = 1 g L^{-1}	Freundlich/isotherm	• No regeneration or recyclability studies were conducted in this research • The study focused solely on adsorption performance at different temperatures without investigating the reusability of the 2D-MX@Fe$_3$O$_4$ adsorbent	• No toxicity assessment or environmental impact evaluation was performed in this study • The research concentrated on adsorption mechanisms and temperature effects without addressing potential health or environmental risks
Ti$_3$C$_2$T$_x$/NiFeMn-LDH@Gel[146]	CR	588.24	C_0 = 50–300 mg L^{-1}, 298–328 K, pH = 3–9	Freundlich/PSO	• The composite demonstrated excellent recyclability with 74.94% and 71.72% removal efficiency maintained for Cr(vi) and CR, respectively, after 5 cycles • Regeneration was achieved using 1 M NaCl/methanol solution with continuous stirring for 2 h, followed by drying at 50 °C for 8 h before reuse	• A comprehensive leaching test was conducted using the ICP-MS technique to detect potential metal leaching (Ni, Fe, Mn) over pH range 3–9 • Results showed almost constant metal content after adsorption processes, confirming the stability and safety of the composite for practical applications without significant metal leaching
AMXGO[147]	MG	1111.6	C_0 = 100–400 mg L^{-1}, 298 K–328 K, pH = 2–12	Freundlich/PSO	• The composite maintained >70% removal efficiency for both MG and CR after 5 cycles	• Zeta potential analysis showed stable surface charge (−20.54 to −52.00 mV, pH 2–12) without harmful ion leaching • XRD and FTIR confirmed no structural degradation after multiple cycles, ensuring material safety
MXene/COF[148]	MB	96.4%	Effective membrane area ~ 8.0 cm^2	—	• Regeneration used 5 mL detergent + 100 mL DI water, stirred for 3 h, washed to neutral pH, then freeze-dried • The membrane maintained >96% rejection and >243 L m^{-2} h^{-1} water permeance after 45 h of continuous operation	• XRD analysis confirmed no structural degradation with d-spacing remaining stable at ~1.46 nm after extended operation
MXene/COF[148]	CR	98.2%	Effective membrane area ~ 8.0 cm^2	—	• No specific regeneration process described – membrane showed excellent stability without requiring regeneration protocols	• Membranes showed excellent anti-swelling properties under pH 3–10 conditions, maintaining structural integrity without toxic leaching
MXene/COF[148]	MO	97.2%	Effective membrane area ~ 8.0 cm^2	—		
alk-MXene/ZIF composites[149]	CR	539.7	298–318 K, pH = 8	Elovich/PSO	• The composite maintained >85% removal efficiency for all three pollutants (CR, TC, MG) after 5 cycles	• XRD analysis confirmed stable crystalline structure with no significant peak shifts after air exposure for 45 days
alk-MXene/ZIF composites[149]	MG	7111.3	298–318 K, pH = 8	Elovich/PSO	• Regeneration achieved using anhydrous ethanol stirring for 2 h, followed by deionized water washing and freeze-drying	• Membrane filtration tests showed >90% removal maintained after 5 cycles, demonstrating material safety without water leaching
DSP-M[150]	RhB	678.19	C_0 = 2–100 mg L^{-1}, 30 °C–60 °C, pH = 7	Langmuir/PSO	• The composite maintained a stable performance with no specific regeneration protocol described, showing structural integrity after multiple adsorption–desorption cycles	• XPS analysis confirmed no harmful metal leaching or toxic byproduct formation during adsorption processes
DSP-M[150]	CR	754.41	5–200 mg L^{-1}, 30 °C–60 °C, pH = 7	Langmuir/PSO	• Material stability confirmed through XRD and FTIR analysis showing no structural degradation after repeated use	• Statistical physics modeling confirmed physical adsorption processes ($E < 8$ kJ mol^{-1}) involving safe hydrogen bonding, electrostatic forces, and van der Waals interactions
ZnS/CuFe$_2$O$_4$/MXene (ZSCFOM)[151]	DBM	377	0.02–4 g L^{-1}, 12 h, 75 rpm, 20 °C	Langmuir/PSO	• Good reusability with no significant reduction in DBM removal rate after three cycles	• Successfully applied to real environmental waters (tap, pond, river) with 100% removal of 0.05 g L^{-1} dyes

Table 1 (Contd.)

MXene	Dye	Adsorption capacity/% removal efficiency	Experimental conditions	Isotherms/ kinetics	Regeneration	Toxicity evaluation
ZnS/CuFe$_2$O$_4$/MXene (ZSCFOM)[151]	DBRN	390	0.02–4 g L^{-1}, 12 h, 75 rpm, 20 °C	Langmuir/ PSO	• Excellent thermal stability with minimal weight loss (0.23–0.38%) at 25–600 °C • Magnetic separation capability for easy recovery using CuFe$_2$O$_4$ component	• Photocatalytic process generates environmentally benign products through complete mineralization • Magnetic properties enable easy separation and recovery, preventing secondary contamination
PHGC/MXene[135]	AB93	207.47	$C_0 = 50$–100 mg L^{-1}, 298–308 K, pH = 2	Langmuir/ PSO	• Excellent reusability with removal rates remaining above 90% for AB93 and above 97% for MB after 12 cycles • Regeneration achieved using 0.1 mol L^{-1} NaHCO$_3$ solution for AB93 and 0.1 mol L^{-1} HCl solution for MB • Minimal decrease in performance (less than 3% compared to highest removal rate) demonstrating excellent stability • Both acidic and alkaline regeneration solutions proved effective for respective dye systems	• No comprehensive toxicity assessment of the PHGC/MXene composite material itself was conducted • Effective removal of toxic anionic (AB93) and cationic (MB) dyes from contaminated water • Successfully tested over different pH ranges (2–12) without significant material degradation • Non-toxic regeneration process using environmentally acceptable desorption agents (NaHCO$_3$ and HCl) • No adverse effects on hydrogel structure during multiple regeneration cycles • Material demonstrated biocompatibility based on constituent components
ZIF-8@IL-MXene/PNIPAM[152]	CV	325.03	$C_0 = 0.4$–2 mg L^{-1}, 25–45 °C, pH = 7	Freundlich/ PSO	• Good reusability with adsorption capacities decreasing to 79%, 91%, and 29% for 4-NP, CV, and Cu^{2+}, respectively, after five cycles • Desorption achieved via volume phase transition in deionized water at 35–40 °C (environmentally friendly process) • Decline in Cu^{2+} adsorption due to strong chelation bonds, which are difficult to break through phase transition	• Environmentally friendly synthesis and desorption processes without organic solvents • Successfully applied to multifunctional removal of phenols, dyes, and metal ions from industrial wastewater • VPTT range 33–35 °C enables safe temperature-responsive desorption process • No toxic byproducts reported during adsorption/desorption cycles
AMXGO[153]	CR	1133.7	$C_0 = 100$–400 mg L^{-1}, 298 K–328 K, pH = 2–12	Freundlich/ PSO	• Good reusability with removal efficiencies gradually decreasing over five cycles	• No significant effects from common cations (Na$^+$, K$^+$, Ca^{2+}, Mg^{2+}) and anions (Cl$^-$, NO$_3^-$, CO$_3^{2-}$, SO$_4^{2-}$) on dye removal
CMC composite[153]	AO7	367.9	$C_0 = 50$–500 mg L^{-1}, 25–45 °C, pH = 3–11	Sips/PSO	• AO7 showed least decrease in efficiency, followed by MO and CR after five cycles	• Successfully tested in different water matrices (deionized, tap, and lake water)
CMC composite[153]	MO	294.2	$C_0 = 50$–500 mg L^{-1}, 25–45 °C, pH = 3–11	Sips/PSO	• Gradual decrease attributed to incomplete desorption and loss of surface functional groups during the regeneration process	• Slightly reduced performance in tap and lake water due to competing ions and organic matter
CMC composite[153]	CR	628.5	$C_0 = 50$–500 mg L^{-1}, 25–45 °C, pH = 3–11	Sips/PSO		• Effective removal of carcinogenic, mutagenic, and toxic anionic azo dyes from contaminated water • No specific toxicity assessment of the CMC composite material itself was conducted
SC-PLA/PDA/MXene membrane[154]	MB	434.8	$C_0 = 0.5$–2 g L^{-1}	Langmuir/ PSO	• Good cycling stability demonstrated over 10 consecutive separation cycles for oil/water separation • Water flux remained stable at 1429.0 L (m^2 h)$^{-1}$ even after 10 cycles for E-N/W separation • Oil flux maintained at ~1862.0 L (m^2 h)$^{-1}$ for the first 4 cycles in E-W/N separation, then declined to 1563.3 L (m^2 h)$^{-1}$ (84.6% retention) after 10 cycles • Alcohol regeneration treatment used between cycles with good recovery performance • Excellent reusability for simultaneous oil and MB removal with water flux maintaining high levels after 6 reuse cycles • Minor performance decline attributed to porosity blocking by residual oil during separation process	• Biodegradable PLA-based composite material providing eco-friendly alternative to conventional polymer membranes • Eliminates potential secondary pollution from plastic debris entering water systems • No comprehensive toxicity assessment of the composite material conducted • Effective removal of toxic organic pollutants (MB) from contaminated water • Biocompatible polylactide substrate reduces environmental impact compared to non-degradable polymer membranes • Polydopamine and MXene components generally considered biocompatible based on the literature

Table 1 *(Contd.)*

MXene	Dye	Adsorption capacity/removal efficiency/%	Experimental conditions	Isotherms/kinetics	Regeneration	Toxicity evaluation
Fe$_2$O$_3$/BC/MXene[155]	MB	899.03	C_0 = 15–45 mg L^{-1}, 293–313 K, pH = 1–11	Langmuir/PSO	• Pb^{2+} sorption capacity: 99.91% → 90.99% after 5 cycles; MB: 98.63% → 89.47% • Desorption efficiency: Pb^{2+}: 96.8% → 78.32%; MB: 95.08% → 77.40% after 5 cycles • Easy separation using external magnetic field	• Biochar-based composite provides sustainable wastewater treatment • Effectively removes highly toxic lead and MB from water • Composite material itself not assessed for environmental/health impacts • Generally considered safe based on the literature
TiVCT$_x$/GAs[156]	MB	319.67	298–338 K, pH = 1–13	Langmuir/PSO	• Excellent cycling stability demonstrated over 5 successive adsorption–desorption cycles	• Leaching experiments confirmed that TiVCT$_x$/GAs adsorbent did not produce secondary pollution during the adsorption process
TiVCT$_x$/GAs[156]	RhB	303.45	298 K–338 K, pH = 1–13	Langmuir/PSO	• MB removal rate remained at around 95.8% after five cycles	• Effectively removes highly toxic organic contaminants including dyes and antibiotic drugs from wastewater
TiVCT$_x$/GAs[156]	CR	229.97	298 K–338 K, pH = 1–13	Langmuir/PSO	• High absorption capacity maintained even after five cycles of absorption–squeezing for oil/solvent removal	• No comprehensive toxicity assessment of the composite material itself conducted
TiVCT$_x$/GAs[156]	MO	217.87	298 K–338 K, pH = 1–13	Langmuir/PSO	• Easy regeneration through simple mechanical squeezing due to excellent elasticity of TiVCT$_x$/GAs	• Biocompatible components generally considered safe for environmental applications
MCF hybrid aerogel[157]	MB	356.97	C_0 = 3–100 mg L^{-1}, 303 K–333 K, pH = 11	Langmuir/PSO	• Limited regeneration assessment mentioned in the study	• No comprehensive toxicity assessment of the MCF composite material conducted
MCF hybrid aerogel[157]	CR	647.75	C_0 = 3–200 mg L^{-1}, 303–333 K, pH = 6	Langmuir/PSO	• No comprehensive cycling stability evaluation provided	• Focuses on removing highly toxic contaminants: MB causes DNA structure damage, cancer risk, heart rate acceleration, shock, and tissue necrosis • CR degradation produces benzidine, a recognized human carcinogen
					• Brief mention that physical adsorption is beneficial for reversible processes and adsorbent regeneration after desorption • Statistical physics modeling suggests physical interaction enables regeneration potential	• MCF designed as environmentally-friendly technology for hazardous dye elimination • No secondary pollution production during adsorption process confirmed through leaching experiments
Ni$_3$(HITP)$_2$/MXene/CS[158]	MB	424.99	10–400 mg L^{-1}, 298 K, pH = 2–9	Langmuir/PSO	• Five consecutive adsorption–desorption cycles conducted for reusability evaluation • Composite maintained excellent adsorption rate after five cycles for both Pb(II) and MB • Chemical adsorption nature may pose challenges for complete regeneration • Detailed regeneration protocols not clearly presented in the main text	• No comprehensive toxicity assessment of the composite material conducted • Composite uses biocompatible chitosan biopolymer as the base material • No secondary pollution or leaching studies reported
MXene with biomass activated carbon (CMAC)[159]	CR	1264.032	C_0 = 0–400 mg L^{-1}, 25–75 °C, pH = 6, dose = 10 mg per 100 mL	Langmuir/PSO	• Desorption and recyclability studies conducted using ethanol as the desorbing agent • CMAC mixed with 100 mL ethanol and stirred at 25 °C for 24 h • Good adsorption effect maintained for all three dyes after multiple desorption cycles • No significant loss of performance after several cycles • Economic benefit and high stability demonstrated for wastewater treatment applications	• No comprehensive toxicity assessment of the CMAC composite material conducted • Focus on removing highly toxic anionic azo dyes that are carcinogenic and mutagenic • CMAC composite uses biomass activated carbon as environmentally friendly base material • No secondary pollution or environmental impact studies reported
Macroporous cellulose nanocrystals (CNC)/MXene/PVA (C-CMP)[160]	MB	239.92	pH = 6, 338 K, 250 mg L^{-1}	Langmuir/PSO	• Adsorption–desorption experiment conducted for three cycles using 0.1 mol L^{-1} HCl for desorption • MB removal efficiency maintained above 80% after three cycles • Good recyclability of C-CMP composite foam confirmed • Slightly decreased efficiency attributed to strong interaction between MB and C-CMP • Residual dye from previous cycles may affect subsequent performance	• No comprehensive toxicity assessment of the C-CMP composite material conducted • Focus on removing highly toxic MB, which severely affects water transparency and dissolved oxygen • MB is difficult to degrade due to benzene ring structure and accumulates in drainage systems • Even 1 mg L^{-1} concentration severely impacts water quality • Composite uses biocompatible materials: cellulose nanocrystals and polyvinyl alcohol • No environmental impact or secondary pollution studies reported

C_0: concentration of dye

chemistry and charge properties. The natural surface terminations of MXenes (–F, –OH, $=$O) create reactive sites for various chemical modifications, allowing the addition of specific functional groups that can greatly enhance their selectivity, capacity, and stability for dye removal. These methods aim to modify the surface features of MXenes without significantly altering their layered structure, thus maintaining their unique 2D properties while adding new functionalities. Surface functionalization techniques include chemical modifications through covalent bonding of organic groups, alkali treatments to change surface terminations, organic coupling reactions to attach complex molecular structures, and surfactant modifications to adjust surface charge and hydrophilicity. Each approach provides distinct benefits, such as boosting electrostatic interactions, hydrogen bonding, π–π interactions, and other molecular interactions that affect dye adsorption. Successful surface functionalization not only improves adsorption performance but also enables the creation of pH-responsive materials, selective adsorbents for specific dyes, and systems with better regeneration ability, making them highly useful for practical water treatment.

Li and co-authors effectively synthesized Nb_2CT_x MXene with a particular surface area by etching Nb_2AlC with hydrofluoric acid (Fig. 5a). The Nb_2CT_x MXene produced is highly effective at adsorbing methylene blue (MB) and methyl orange (MO) dyes, achieving maximum capacities exceeding 500 mg g^{-1}. For starting concentrations of 100 and 200 mg g^{-1}, ~99% MO dye may be removed in ~30 min (Fig. 5d and e). However, MB dye removal requires just 5 min of contact time. Furthermore, the adsorption process of Nb_2CT_x MXene is governed by a pseudo-second-order kinetics model (Fig. 5b and c),

with chemisorption at the surface absorption active sites serving as the rate limiting factor.[131]

The elimination of MB and Congo red (CR) dyes from wastewater was accomplished by Li *et al.* by the fabrication of the AA-alk-MXene-based adsorbent. This was accomplished by attaching acrylic acid (AA) to alkalized single or several layered MXene nanosheets. The influence of pH, temperature, concentration of dye, contact time and AA dosage on adsorption was examined. The process of adsorption used the pseudo-second-order kinetic and Langmuir isotherm adsorption model. The highest adsorption capacity of an AA-modified sample (2 mL) for MB and CR was found to be 193.92 mg g^{-1} and 264.46 mg g^{-1}, respectively. Furthermore, hydrogen bonding, electrostatic attraction, and interlayer forces are likely the primary driving forces behind the adsorption mechanism of AA-alk-MXene (Fig. 6a and b).[132]

By modifying Ti_3C_2 to incorporate sulfonic groups through aromatic coupling–diazotization, Wei *et al.* achieved the fabrication of 2D MXenes. This was accomplished by removing the Al layer from Ti_3AlC_2 through a simple process. A further investigation into the adsorption behavior of functionalized Ti_3C_2 against MB was conducted under various experimental conditions, including pH, solution temperature, initial MB concentration, and contact time. The results demonstrated that Ti_3C_2–SO_3H achieved an adsorption performance of 111.11 mg g^{-1}. Kinetic and isotherm analyses revealed that the pseudo-first-order and Langmuir isotherm adsorption models were appropriate for explaining the experimental data. The deposition of MB onto adsorbent surfaces was endothermic, while dye adsorption was most effective when the aqueous solution was alkaline (Fig. 7).[133]
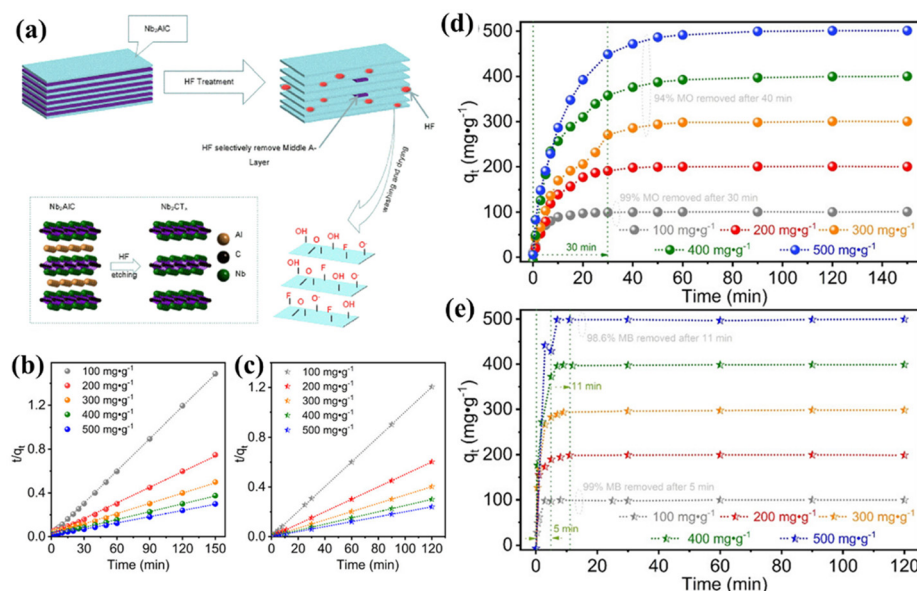

Fig. 5 (a) Schematic diagram of Nb_2CT_x MXene preparation by etching Nb_2AlC with HF solution. (b) and (c) Pseudo-second-order kinetics analysis for MO and MB adsorption by Nb_2CT_x at room temperature. (d) and (e) Relationship between the adsorption capacity of Nb_2CT_x and contact time at different initial MO and MB concentrations at room temperature, pH = 7, and 1 g L^{-1} Nb_2CT_x powder dose. Reproduced with permission from ref. 131 Copyright 2021, American Chemical Society.
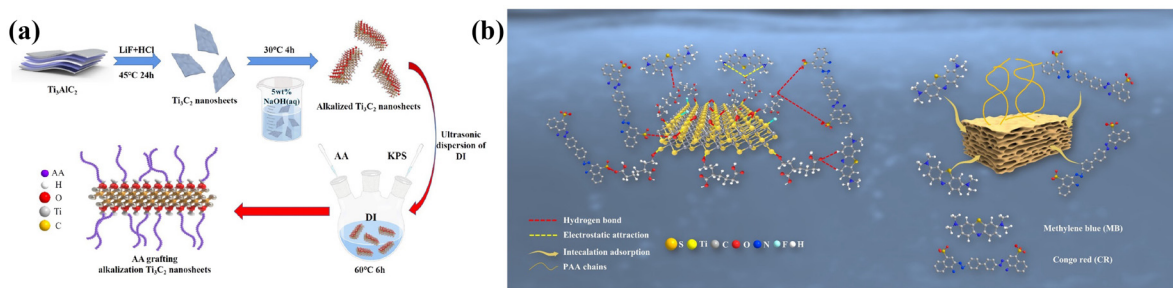
Fig. 6 (a) Schematic diagram for preparing AA-alk-MXene; (b) diagram of the adsorption mechanism of AA-alk-MXene for MB and CR. Reproduced with permission from ref. 132. Copyright 2022, Elsevier.
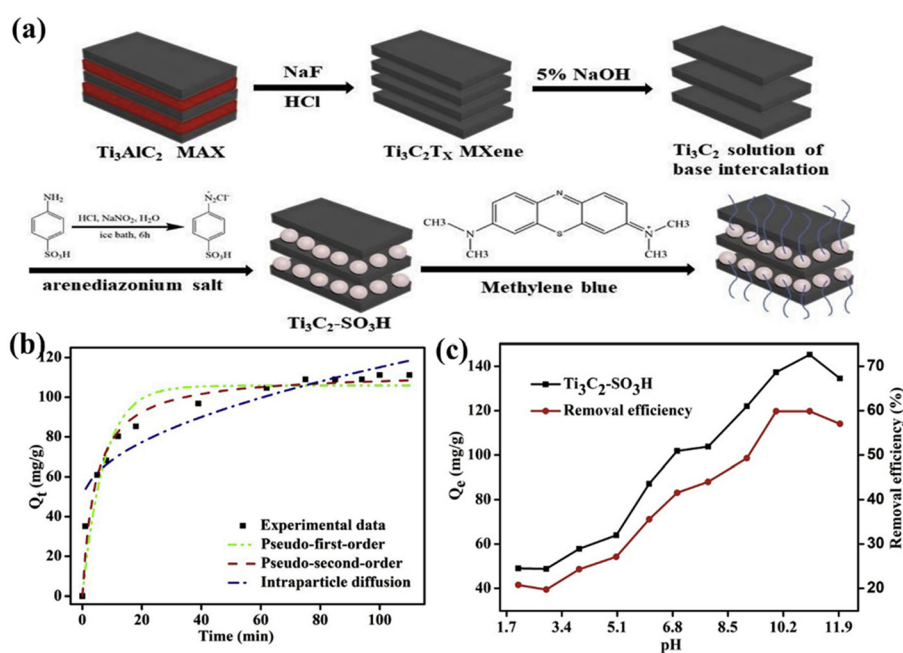

Fig. 7 (a) Schematic diagram for the preparation of $Ti_3C_2–SO_3H$ for MB removal. (b) The kinetic curves of $Ti_3C_2–SO_3H$ adsorption MB. (c) Effect of pH on the adsorption of MB onto $Ti_3C_2–SO_3H$. Reproduced with permission from ref. 133. Copyright 2019, Elsevier.

Kelishami *et al.* designed a cetyltrimethylammonium bromide (CTAB)-modified multi-layered $Ti_3C_2T_x$ MXene (CMM) from Ti_3AlC_2 precursor and was employed to remove MO (Fig. 8a and b). This material adsorbent resulted from an electrostatic combination of the cationic surfactant solution (CTAB) and negatively charged $Ti_3C_2T_x$ nanosheets. The accessible active sites were exposed as a result of this, which resulted in an increase in the spacing between the nanosheets and an increase in adsorption efficiency. The adsorbents were analyzed by using a few analytical techniques, and the impact of various parameters (contact time, pH, loading adsorbent, and initial concentration of dye) was investigated. The results of this study demonstrated that MO adsorbed CMM to its maximum capacity at an adsorbent dosage of 0.83 g L⁻¹, a contact time of 90 min, and a solution pH of 3. The results of the adsorption experiment were most accurately represented by the pseudo-second-order kinetic model ($R^2 = 0.9924$) and

the Langmuir isotherm ($R^2 = 0.9990$). Approximately 213.00 mg g⁻¹ was the maximum adsorption capacity that MO possessed. There is a possibility that the MO adsorption mechanism on CMM involves many interactions, including electrostatic adsorption, π–cation interactions, and hydrogen bonding.[136]

4.2. Interlayer engineering and spacing modification

Interlayer engineering and spacing modification represent critical strategies for optimizing the structural architecture of MXenes to enhance their dye adsorption capabilities. The layered nature of MXenes, with interlayer spaces typically ranging from 0.98 to 1.5 nm in their pristine form, provides unique opportunities for structural manipulation to accommodate different dye molecules and improve accessibility to adsorption sites. These approaches focus on controlling the interlayer distance through various techniques that expand, maintain, or systematically modify the spacing between
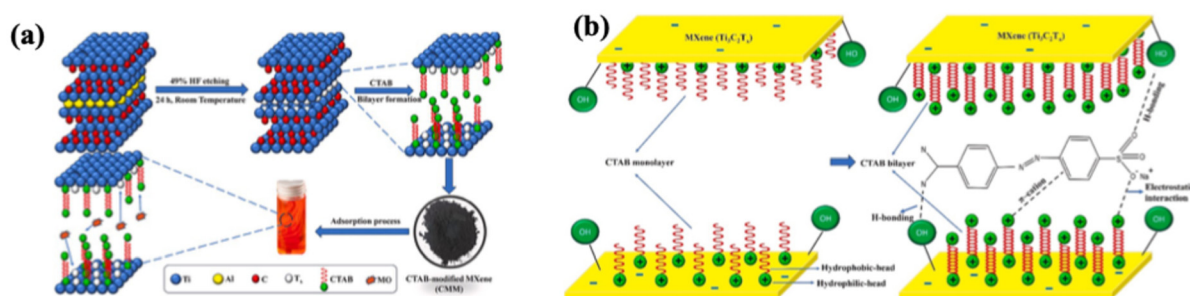
Fig. 8 (a) Illustration of the intercalation of CTAB in MXene (CMM) for the adsorption of MO; (b) CTAB monolayer and bilayer formation on MXene ($Ti_3C_2T_x$) sheets and adsorption mechanisms of MO by MXene sheets. Reproduced with permission from ref. 136. Copyright 2024, Elsevier.

MXene layers. Interlayer expansion techniques involve the insertion of molecules or ions that physically separate the layers, creating larger void spaces for enhanced accommodation of dye molecules. Ion intercalation methods utilize cations or anions to penetrate between layers, causing structural swelling and increased surface accessibility. Delamination strategies aim to entirely or partially separate multi-layered MXene structures into individual or few-layer nanosheets, maximizing the available surface area. Pillaring approaches involve the insertion of rigid molecular or ionic species that act as structural supports, maintaining controlled interlayer distances while preventing restacking. These interlayer engineering strategies are particularly effective because they directly address the accessibility limitations inherent in layered materials, enabling larger dye molecules to penetrate

the interlayer galleries and access previously unavailable adsorption sites. The controlled modification of interlayer spacing also facilitates size-selective adsorption, improves mass transfer kinetics, and enhances the overall adsorption capacity by creating a three-dimensional network of accessible adsorption sites throughout the material structure.

Gogotsi et al. tested $Ti_3C_2T_x$ stacked sheets bound by hydrogen bonds and/or van der Waals interactions for the adsorption of MB dye. $Ti_3C_2T_x$ showed an adsorption capacity of 39 mg g^{-1} for MB. The adsorption of MB on $Ti_3C_2T_x$ was most closely related to the Freundlich isotherm model.[128]

Through the use of an alkali solution, ZhengMing et al. described a straightforward method for increasing the interlayer gap of $Ti_3C_2T_x$ while modulating the surface functional groups of the material (Fig. 9a).[129] Using LiOH, the approach
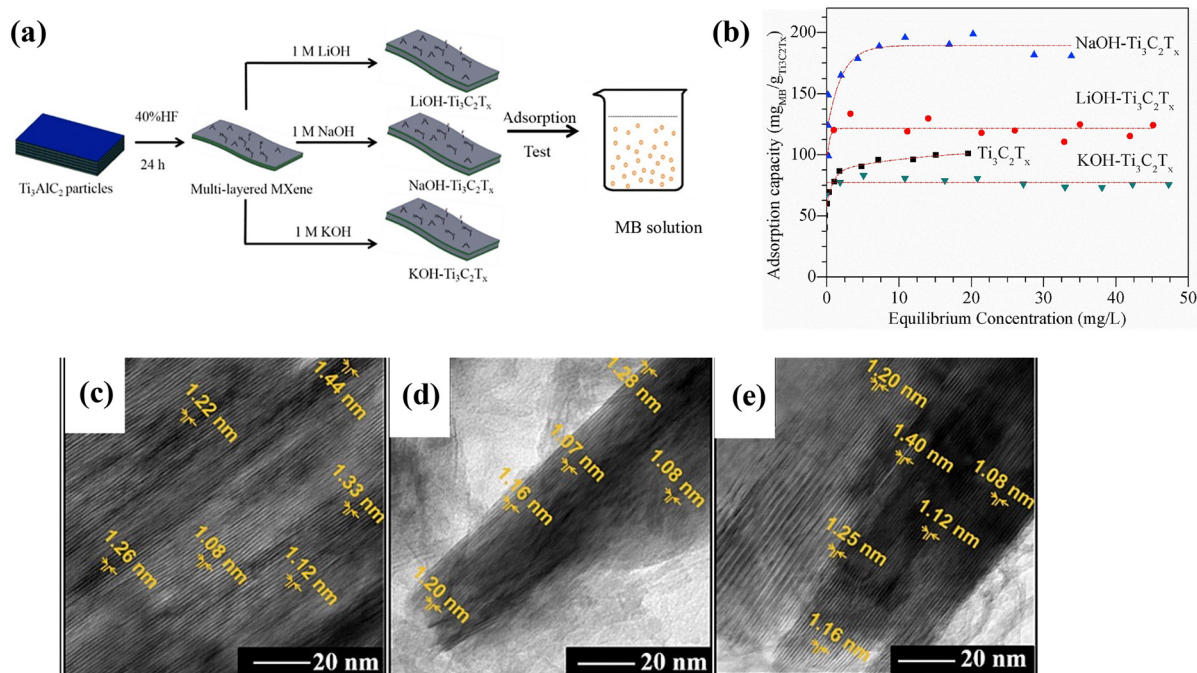

Fig. 9 (a) Illustration of the fabrication of different alkali-$Ti_3C_2T_x$ towards the adsorption of MB dye. (b) Adsorption isotherms of MB on $Ti_3C_2T_x$, LiOH–$Ti_3C_2T_x$, NaOH–$Ti_3C_2T_x$ and KOH–$Ti_3C_2T_x$. HRTEM images of (c) LiOH–$Ti_3C_2T_x$, (d) NaOH–$Ti_3C_2T_x$ and (e) KOH–$Ti_3C_2T_x$. Reproduced with permission from ref. 129. Copyright 2017, Elsevier.

is able to enhance the spacing between layers in $Ti_3C_2T_x$ MXene by 29%. Additionally, the modification of functional groups involves the transformation of –F into –OH. NaOH–$Ti_3C_2T_x$ and LiOH–$Ti_3C_2T_x$ MXenes are able to adsorb MB more quickly compared to other types of MXene adsorbents. Notably, NaOH–$Ti_3C_2T_x$ has the ability to adsorb maximum MB, with a capacity of 189 mg g^{-1}; this is attributed to the combination of intercalation adsorption and surface adsorption of the MXene (Fig. 9b). High-resolution transmission electron microscopy (HRTEM) images (Fig. 9c–e) reveal significant structural modifications following alkaline metal ion intercalation in LiOH–$Ti_3C_2T_x$, NaOH–$Ti_3C_2T_x$, and KOH–$Ti_3C_2T_x$ systems. The intercalation process involves alkaline metal ions (Li^+, Na^+, K^+) inserting between MXene layers, causing interlayer spacing expansion through electrostatic interactions and hydration shell formation. Structural expansion mechanisms include: direct ion insertion where alkaline cations occupy interlayer galleries, creating physical separation between $Ti_3C_2T_x$ sheets; hydration-induced swelling as intercalated ions attract water molecules, forming hydration shells that further increase interlayer distance; and surface functionalization changes where alkaline treatment converts surface –F terminations into –OH groups, enhancing hydrophilicity and water take up. The measured interlayer spacings show progressive expansion: LiOH–$Ti_3C_2T_x$ (~1.22–1.65 nm), NaOH–$Ti_3C_2T_x$ (~1.16–2.0 nm), and KOH–$Ti_3C_2T_x$ (~1.40–1.73 nm), correlating with ionic radius differences ($Li^+ < Na^+ < K^+$) and hydration characteristics. This structural expansion directly contributes to enhanced adsorption capacity by increasing the accessible surface area and creating larger pore channels for dye molecule accommodation, explaining the superior MB adsorption performance observed in alkaline-modified MXene systems.

Yu and co-workers developed a novel hydrothermal method utilizing less toxic etching agents such as $NaBF_4$, HCl for the synthesis of Ti_3C_2 MXene (h-Ti_3C_2). Because of the slow-release mechanism during hydrothermal treatment, h-Ti_3C_2 has a higher lattice parameter c, and a longer interlayer distance, as well as a better SSA than t-Ti_3C_2. The hydrothermal etching method avoids high-concentration HF and is more effective at synthesizing Ti_3C_2 flakes. Furthermore, the etching method can be used for other MXene compositions, for example, Nb_2C and h-MXenes show superior adsorption performances for MB, with a capacity of 24 mg g^{-1}.[130] Cagnetta and colleagues synthesized $Ti_3C_2T_x$ MXene layers pillared with terephthalate using an innovative MC etching approach that involved exfoliating a titanium MAX phase with a small volume of concentrated hydrofluoric acid using a high-energy ball mill. The obtained material has a larger SSA and strong adsorption capability of MB of 209 mg g^{-1} because of wider interlayer spaces between free carboxylate groups of terephthalate and MXene sheets. Also, dye adsorption with the material is best explained by a pseudo-second-order model.[141]

Yang *et al.* produced a suspension of $Ti_3C_2T_x$ MXene nanosheets using the intercalation and delamination of multilayered $Ti_3C_2T_x$ utilizing TMAOH. The prepared material showed excellent adsorption of cationic MB dye. The highest adsorption capacity, noted at 318 K, reached 1026 mg g^{-1}. This performance best fits with pseudo-second-order kinetic and Freundlich isotherm models. The mechanism of adsorption is mainly attributed to ion exchange and electrostatic attraction for MB removal.[142] By intercalating GO into an Alk-MXene layer, Li and co-workers were able to report a novel AMXGO absorbent. This absorbent demonstrated a high level of efficiency in the elimination of MG and anionic CR (Fig. 10). The results of FTIR, XRD, and SEM investigations showed that
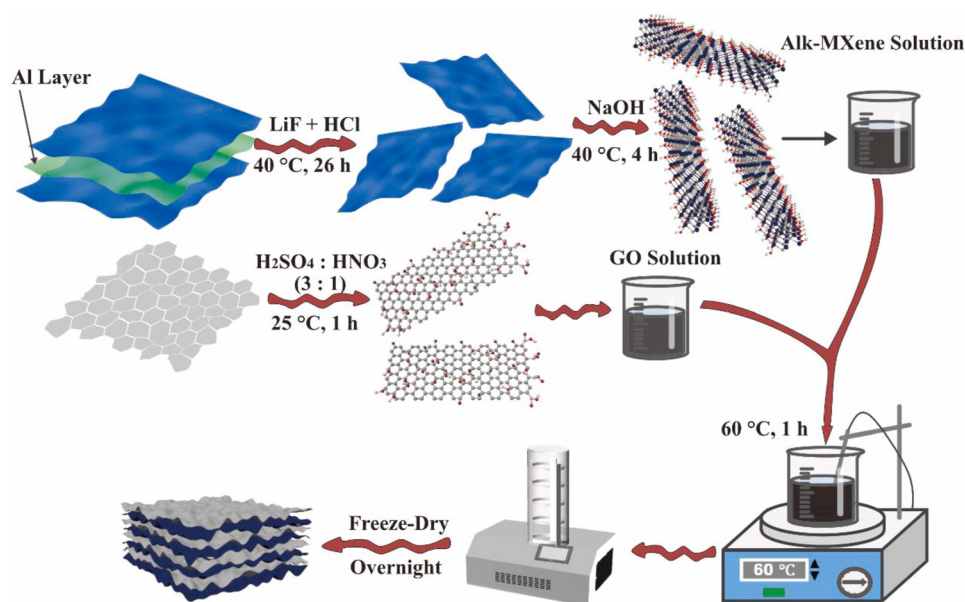

Fig. 10 Diagram for the preparation of AMXGO. Reproduced with permission from ref. 147. Copyright 2024, Elsevier.

the AMXGO absorbent possessed a characteristic 3D layer-by-layer structure with plentiful oxygen-bearing groups, and that its heat stability had greatly improved. Based on the results of the BET analysis, it was determined that the AMXGO1 adsorbent possessed a larger SSA ($16.686 \text{ m}^2 \text{ g}^{-1}$) and pore volume ($0.04733 \text{ cm}^3 \text{ g}^{-1}$). It was found that the adsorption performance was dependent on the mass ratio of Alk-MXene to GO, the starting dye concentration, pH, contact time, and temperature. The AMXGO1 absorbent, which had a mass ratio of $3:1$, had a maximum capacity to adsorb 1111.6 mg g^{-1} of MG and 1133.7 mg g^{-1} of CR, and it had dye removal rates that were greater than 92%. Both pseudo-second-order kinetic and Freundlich isotherm models are utilized to describe the adsorption behaviour of AMXGO1 for both CR and MG.[147]

4.3. Composite formation strategies

Composite formation strategies represent a versatile and powerful approach for developing advanced MXene-based adsorbents by synergistically combining the unique properties of MXenes with complementary materials to achieve enhanced dye removal performance. These strategies leverage the principle that the integration of different materials can result in synergistic effects that surpass the individual performance of constituent components, resulting in composites with superior adsorption capacities, improved selectivity, enhanced stability, and additional functionalities such as magnetic separability or pH responsiveness. The composite formation approaches can be systematically categorized based on the nature of the secondary materials integrated with MXenes. MXene–organic composites involve the combination of MXenes with organic polymers, biomaterials, or carbon-based materials, creating hybrid systems that benefit from the conductivity and surface chemistry of MXenes while gaining enhanced mechanical properties, biocompatibility, or specific functional groups from the organic components. MXene–inorganic composites integrate MXenes with metal oxides, hydroxides, or other inorganic materials, often resulting in enhanced adsorption capacity through increased surface area, additional adsorption sites, or new interaction mechanisms such as magnetic separation capabilities. Multi-hybrid systems represent the most sophisticated approach, combining MXenes with multiple different material types to create complex architectures that integrate the advantages of various components, such as combining organic polymers for flexibility, inorganic nanoparticles for functionality, and MXenes for conductivity and surface area. These hybridization strategies not only enhance the fundamental adsorption properties but also address practical considerations such as material recovery, regeneration efficiency, mechanical stability, and cost-effectiveness, making them particularly attractive for real-world water treatment applications where multiple performance criteria must be simultaneously optimized.

Peng *et al.* effectively synthesized MXene-based core–shell composites, MXene–COOH@(PEI/PAA)$_n$, using a layer-by-layer technique. Furthermore, these nanocomposites were studied using spectral and morphological techniques, revealing that they contained more reactive sites and mesoporous structures. The composites fabricated were able to efficiently adsorb MB dye after approximately 200 min, showing that the composites synthesized might be used as a highly efficient adsorbent. The observed data are well matched with a pseudo-second-order model and show a significant correlation coefficient of $R^2 > 0.99$, indicating that the core–shell composites have outstanding adsorption capabilities.[134]

PHGC/MXene, which was reported by Zhang *et al.* (Fig. 11a and b), exhibited a remarkably strong selectivity and cycling stability for ionic dyes across a range of pH values. PHGC/MXene showed exceptional adsorption selectivity and great pH-responsiveness in the mixed dye system. It was able to adsorb MB at a pH of 11.0, and methyl blue (AB93) at pH 2.0, achieving maximum adsorption capacities of 555.56 mg g^{-1} and 207.47 mg g^{-1}, respectively. The adsorption kinetics for these dyes were found to be in agreement with the two-level kinetic model that was proposed, while the Langmuir model demonstrated a good fit for the adsorption isotherms being studied. It was determined that electrostatic adsorption and hydrogen bonding were the primary processes responsible for the adsorption process, with van der Waals forces also making a contribution. Despite undergoing 12 rounds of desorption and regeneration, the clearance rates for MB and AB93 remained more than 90%.[135]
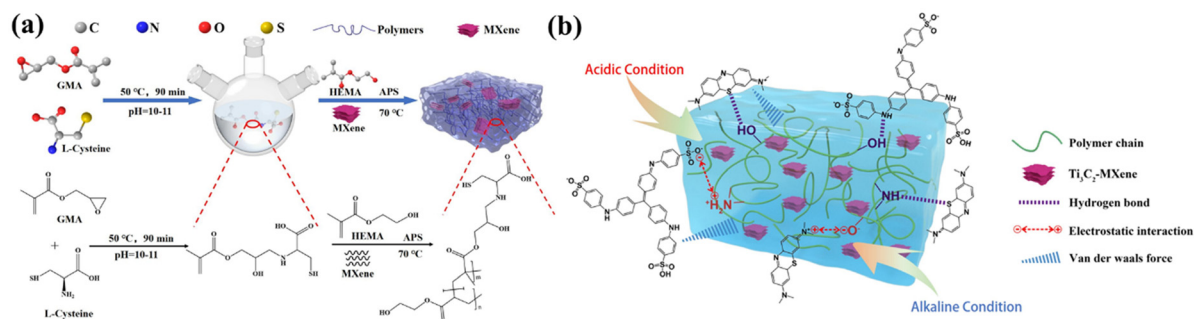

Fig. 11 (a) Schematic preparation of PHGC/MXene hydrogel; (b) adsorption mechanism diagram of PHGC/MXene for AB93 or MB. Reproduced with permission from ref. 135. Copyright 2019, Elsevier.

The amino-functionalized bacterial cellulose/$Ti_3C_2T_x$ MXene (ABC/MX) composites were synthesized by Wen and his colleagues by the utilization of an electrostatic self-assembly technique that comprised modifications with polydopamine (PDA) and polyethyleneimine (PEI) (Fig. 12a). Based on the findings of this research, the effective insertion of amino groups strengthens the interfacial contacts between nanofibers of BC and nanosheets of $Ti_3C_2T_x$; it also enhances the number of active sites for adsorption. With a maximal ability to adsorb 1103.7 mg g^{-1} of CR, the results demonstrate that the composite possesses a remarkable removal efficiency.[137] Using a chemical etching approach, Wang *et al.* reported a few-layer MXene. Subsequently, PEI was grafted onto the surface of the MXene through glutaraldehyde-assisted crosslinking (Fig. 12b). The adsorption properties of water-soluble dyes were extensively studied. The results indicated that grafting with PEI might improve MXene exfoliation and adsorption capacities. The modified MXene showed a remarkable ability to adsorb 909.1 mg g^{-1} of MO. Fig. 12c reveals the binding mechanism between the components of the MPEI composites. The pseudo-second-order kinetic and Langmuir isothermal adsorption models are the most appropriate for the adsorption processes of MO, which are spontaneously endothermic and chemisorption.[138]

Wang and co-authors synthesized a novel $CoFe_2O_4$/CS composite supported on alk-MXene magnetic adsorbent *via* a hydrothermal and self-assembly approach (Fig. 12d). Adding $CoFe_2O_4$/CS to alk-MXene can significantly increase the capacity for adsorbing anionic and cationic dyes. The prepared material showed a high adsorption capacity of up to 1333.9, 537.6, and 2095.9 mg g^{-1} for rhodamine B (RhB), malachite green (MG), and CR dyes, respectively. The higher adsorption performance of the composites is attributed to the synergistic effect of hydrogen bonding, π–π interactions, and electrostatic interactions.[144]

Zhang *et al.* used an *in situ* growth technique to synthesize a new 2D MXene coated with Fe_3O_4. The prepared material was analyzed for MB dye adsorption at different temperatures. This material exhibits superparamagnetic characteristics and a typical 2D lamellar structure. The elimination of MB occurred as an endothermic process, as evidenced by a maximum elimination capacity of 11.68 mg g^{-1} and 91.93% decolorization efficiency at 55 °C, considerably surpassing the performance at lower temperatures. Additionally, at high temperatures (40 and 55 °C), the adsorption isotherm demonstrated that the model which best fit for the removal method of MB was the Freundlich isotherm, but at low temperatures (25 °C), the Langmuir isotherm fit best. Through electrostatic attraction and hydrogen bonding at high temperatures, Ti–OH groups on the material's surface enhance MB decolorization. At 25 °C, surface adsorption by electrostatic interaction aids in the elimination of MB (Fig. 13).[145]

Eltaweil *et al.* fabricated $Ti_3C_2T_x$/NiFeMn-LDH@Gel composites in order to remove organic CR dye synthesized *via* a cross-linking reaction by incorporating $Ti_3C_2T_x$ MXene and NiFeMn-LDH into gelatin (Fig. 14a). The results showed that the adsorption ability of $Ti_3C_2T_x$/NiFeMn-LDH@Gel towards CR was significantly enhanced by raising the $Ti_3C_2T_x$ content in the matrix to 10%. With a q_{max} value of 588.24 mg g^{-1}, the Freundlich model offered the best explanation for the adsorption of CR. Moreover, the pseudo-second-order model was determined to be best for studying the adsorption kinetics of CR. The remarkable recyclability over multiple cycles confirms the composite's sustainability.[146]

Using a macroporous polymeric support, Yang *et al.* were able to effectively fabricated a flexible, rigid, and porous
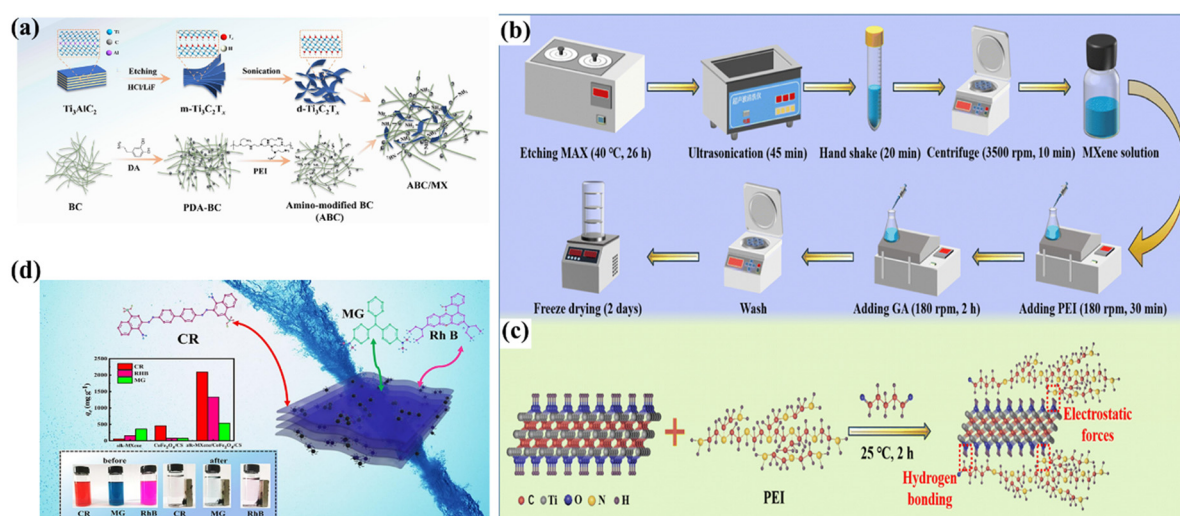

Fig. 12 (a) Schematic diagram of the preparation of ABC/MX composite. Reproduced with permission from ref. 137. Copyright 2024, Elsevier. (b) Synthesis procedure for the MPEI composites and (c) diagram of the inter-component microscopic combination mechanism in MPEI composites. Reproduced with permission from ref. 138. Copyright 2023, Royal Society of Chemistry. (d) Adsorption capacity of different dyes onto alk-MXene/$CoFe_2O_4$/CS composite. Reproduced with permission from ref. 144. Copyright 2023, Elsevier.
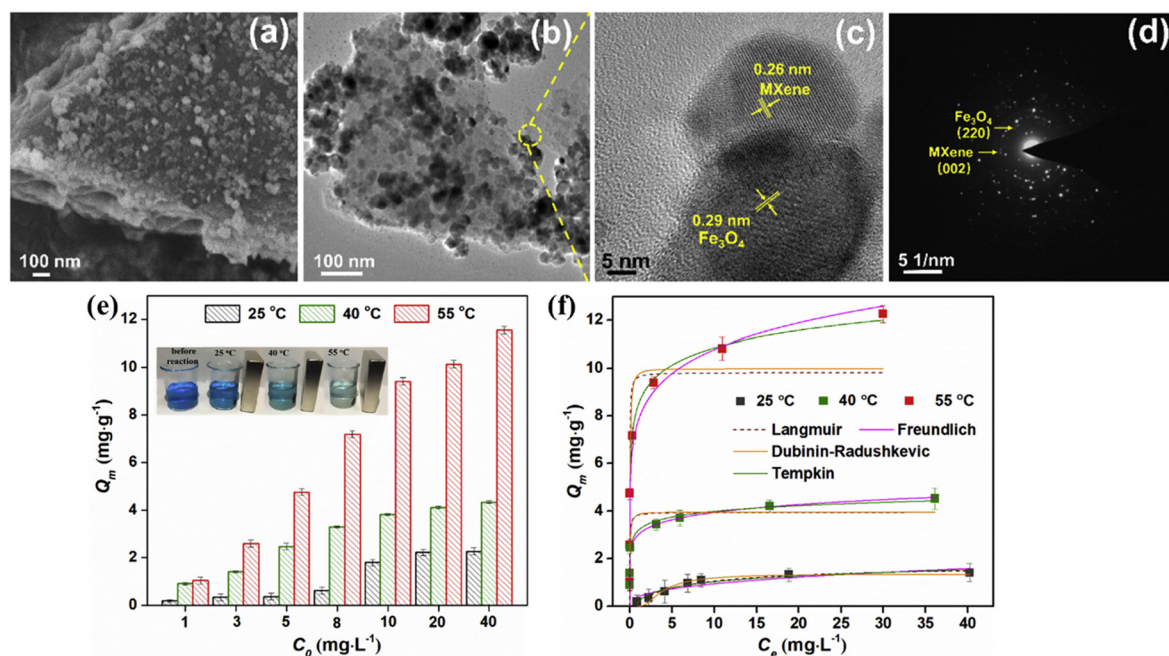
Fig. 13 (a) SEM, (b) TEM, (c) HRTEM, (d) SAED pattern of 2D-MX@Fe$_3$O$_4$ nanocomposites. (e) The removal capacity of MB over 2D-MX@Fe$_3$O$_4$ at 25, 40 and 55 °C. (f) Adsorption isotherms of 2D-MX@Fe$_3$O$_4$ for MB removal. Reproduced with permission from ref. 145. Copyright 2019, Elsevier.

MXene/COF hybrid flake. This flake is characterized by the presence of three 2D COF flakes that are bridged covalently on the surface of the MXene by an *in situ* growth process. COFs (TpTAPB, TpBD, TpPa) were synthesized *via* Schiff-base reactions using 1,3,5-triformylphloroglucinol with 1,3,5-tris(4-aminophenyl) benzene, benzidine and *p*-phenylenediamine monomers (Fig. 14b). Furthermore, interlayers of MXene (Ti$_3$C$_2$T$_x$) nanosheets expand adjacent interlayer spacing and introduce numerous sieving pores when COFs are intercalated into it. The optimized MXene/TpTAPB hybrid membrane, when utilized for eliminating organic dyes, exhibits a removal efficiency of 96.4% for AB93, 98.2% for CR, 97.2% for MO and 98.7% for chrome black T.[148]

Wang *et al.* synthesized the alk-MXene/ZIF composite, with small ZIF particles *in situ* synthesized on interlayer and on the alk-MXene surface (Fig. 14c). In the meantime, a stable intercalation framework is produced, allowing dye molecules to transfer mass more quickly. Adding ZIF particles increases the adsorption functional groups and SSA in the alk-MXene/ZIF composite. The composites achieved excellent adsorption values, with maximum capacities of 7111.3 and 539.7 mg g^{-1} for MG and CR, respectively. The impact of coexisting ions, temperature, concentration, contact time, and pH on the adsorption performance were studied. Adsorption kinetics studies demonstrated that dye adsorption onto the composite surface was consistent with the Elovich and pseudo-second-order kinetic models. Additionally, the adsorption mechanism of the adsorbent is mainly due to chemisorption.[149]

By integrating few-layer MXene and the hydrophilic biomaterial DASNP, followed by immobilization of DASNP onto few-layer MXene through a dialdehyde-based cross-linking technique, Li *et al.* were able to synthesize a novel environmentally friendly composite material known as DSP-M (Fig. 14d). The findings indicated that DSP-M had an outstanding adsorption efficiency for both adsorbates. Furthermore, the Langmuir maximum adsorption capacity for monomer adsorption for RhB was found to be 678.19 mg L^{-1}, while the capacity for CR was found to be 754.41 mg L^{-1}. These results were in agreement with the pseudo-second-order, intraparticle diffusion, and Langmuir models. For the purpose of conducting additional research on the adsorptive mechanism, the physics statistical model was utilized. The DSP-M characteristics post-adsorption and findings of the simulation suggested that RhB and CR removal by DSP-M occurred predominantly through a physical adsorption mechanism involving van der Waals interactions, electrostatic forces, and hydrogen bonding.[150]

Wang and co-authors designed ZnS/CuFe$_2$O$_4$/MXene (ZSCFOM) composites featuring ternary heterostructures *via* a solvothermal approach to efficiently adsorb azo dyes. The composite primarily achieved azo dye adsorption *via* electrostatic interactions and hydrogen bonding, with a maximum adsorption capacity of 377 mg g^{-1} for DBM and 390 mg g^{-1} for DBRN. The pseudo-second-order and Langmuir models were used to characterize the adsorption properties of ZSCFOM, suggesting that the adsorbate formed a monolayer on the ZSCFOM surface.[151]

Moreover, green methods have also been adopted to design MXene-based nanoadsorbents. Ijaz *et al.* synthesized an efficient and rapid Fe$_2$O$_3$/BC/MXene composite by functiona-
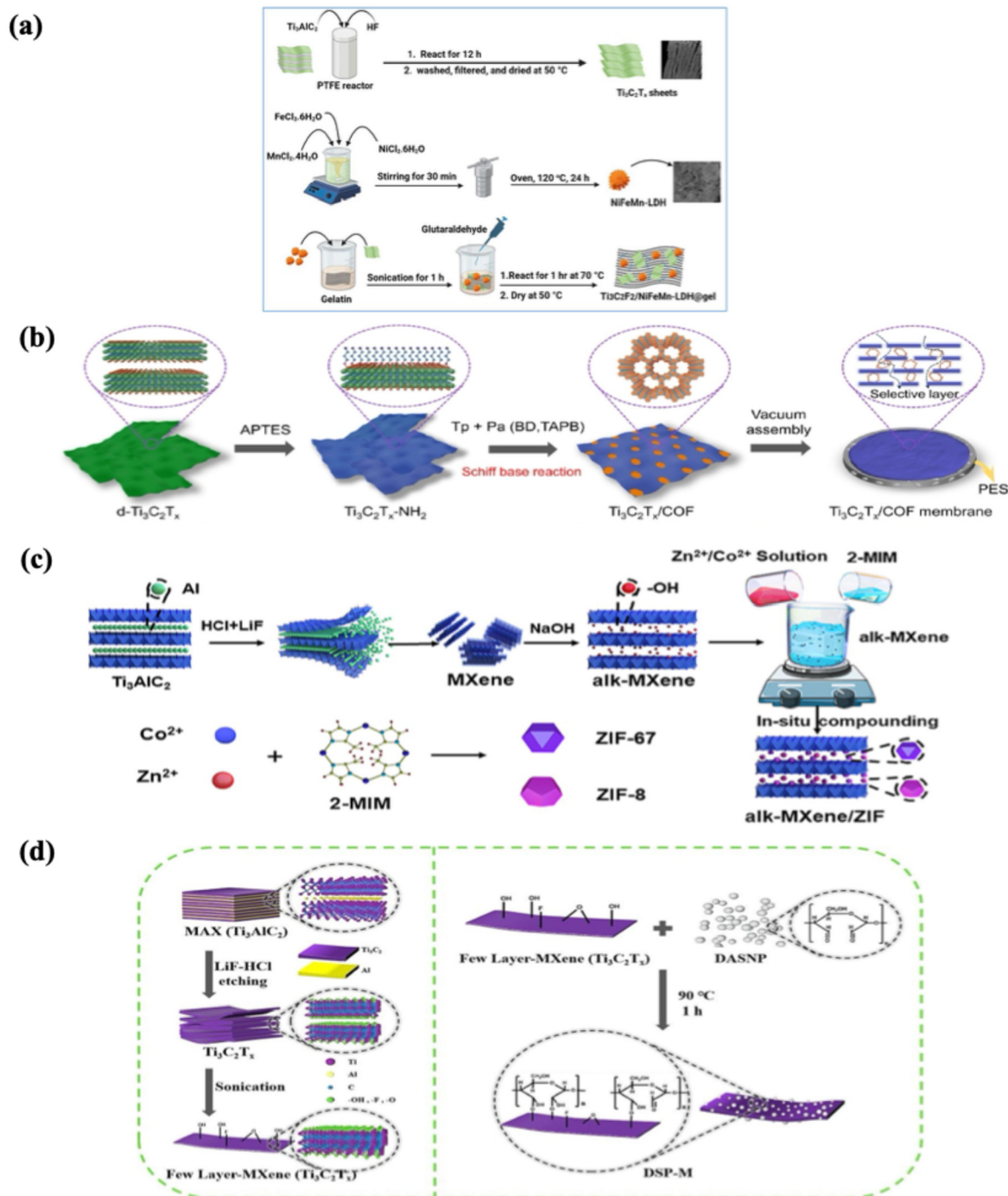
Fig. 14 (a) A schematic presentation of the synthesis of $Ti_3C_2T_x$/NiFeMn-LDH@Gel composite. Reproduced with permission from ref. 146. Copyright 2024, Elsevier. (b) Schematic illustration of the separation mechanism of MXene/COF in the dye wastewater purification process. Reproduced with permission from ref. 148. Copyright 2024, Elsevier. (c) Schematic preparation process for the alk-MXene/ZIF composite. Reproduced with permission from ref. 149. Copyright 2024, Elsevier. (d) Schematic illustration of the step-wise synthesis of DSP-M composite. Reproduced with permission from ref. 150. Copyright 2023, Elsevier.

lizing *Shorea faguetiana* biochar with Fe_2O_3 and MXene for selective adsorption. XPS and FTIR revealed that the Fe_2O_3/BC/MXene composites had more surface functional groups (F^-, C=O, CN, NH, and OH^-) than the original biochar. Characterization studies revealed that the intended modified

BC had a high MB adsorption capacity in wastewater. At 293 K, MB showed a q_m value of 899.03 mg g^{-1}. The adsorption followed a pseudo-second-order model ($R^2 = 1$) and the Langmuir isotherm. Surface electrostatic forces and hydrogen bonding helped to remove MB more efficiently. This demonstrates

monolayer adsorption on the $Fe_2O_3/BC/MXene$ composite, which is regulated by chemical adsorption.[155]

An effective, fast, and selective adsorption of MB was achieved by Imtiaz *et al.* through the development of $Ni_3(HITP)_2/MXene/CS$. This was accomplished by functionalizing chitosan biopolymer with MXene and 2D MOFs $(Ni_3(HITP)_2)$. The TEM image clearly shows irregularly-shaped MOFs and spherical CS particles adhered to the MXene surface. At 298 K, MB had a maximum adsorption capability of 424.99 mg g^{-1}, 400.59 mg g^{-1} at 308 K, and 305.80 mg g^{-1} at 318 K. The adsorption of MB on the $Ni_3(HITP)_2/MXene/CS$ composite followed the pseudo-second-order kinetic and Langmuir models. The composite has –OH, –F, –O, and N groups, which enable effective MB absorption *via* hydrogen bonding, electrostatic attraction, and complexation interaction.[158]

4.4. Morphological and structural control

Morphological and structural control strategies focus on engineering the macroscopic architecture and three-dimensional organization of MXene-based materials to optimize their performance in dye adsorption applications. Unlike surface functionalization or interlayer modifications that primarily alter chemical properties or nanoscale structures, these approaches target the overall physical form, porosity, and architectural arrangement of MXene materials to enhance mass transfer, improve accessibility, and facilitate practical implementation in water treatment systems. The controlled manipulation of morphology enables the creation of materials with tailored pore structures, enhanced mechanical properties, and optimized flow characteristics that are essential for real-world applications. Membrane fabrication represents a critical approach for creating selective barriers with controlled permeability and high surface area-to-volume ratios, enabling efficient dye removal while maintaining structural integrity under operational conditions. Aerogel formation involves the development of ultra-light weight, highly porous three-dimensional networks that maximize surface accessibility while providing excellent adsorption kinetics through interconnected pore channels. Nanofiber integration focuses on incorporating MXenes into fibrous architectures that combine high surface area with excellent mechanical flexibility and easy handling characteristics. The three-dimensional architectural design encompasses the creation of complex hierarchical structures that integrate multiple length scales, from nanoscale MXene sheets to macroscopic frameworks, enabling optimized mass transfer pathways and enhanced adsorption site utilization. These morphological control strategies are particularly valuable because they address critical practical considerations such as a pressure drop in flow-through systems, ease of material recovery and regeneration, mechanical durability under operational stresses, and scalability for industrial applications. By controlling the overall architecture and form factor of MXene-based adsorbents, these approaches bridge the gap between fundamental material properties and practical implementation requirements, enabling the development of efficient, robust, and economically viable water treatment technologies.

Dhar Purkayastha and co-author used vacuum filtering to produce 2D $Ti_3C_2T_x$ MXene on a porous PAN membrane, demonstrating its effective adsorption of MB. MX-PAN had an adsorption effectiveness of 85%, compared to 12% achieved by the PAN membrane. Adsorption efficiency increased dramatically after manufacturing the PAN membrane along with $Ti_3C_2T_x$ MXene nanoflakes.[139] Zhang *et al.* combined SA with d-$Ti_3C_2T_x$ nanosheets (MXene), then employed electrospinning and subsequent Ca^{2+}-mediated crosslinking for the production of various SA/MXene NMs. The impact of MXene in NMs on the MB adsorption ability was examined. SA/MXene NMs exhibited the ability to adsorb 440 mg g^{-1} of MB at an optimal MXene concentration of 0.74 wt%, surpassing electrospun SA NMs, pristine MXene, or SA/MXene composite beads with an equivalent MXene content. Moreover, the optimal SA/MXene NMs demonstrated high reusability. The Langmuir and pseudo-second-order models were in good agreement with the results, indicating that monolayer adsorption aligned with the mechanism of chemical adsorption.[140]

By using cross-linking approaches to incorporate PEI and amino-functionalized $Ti_3C_2T_x$ into the SA aerogel matrix, Wang *et al.* synthesized the MXene/PEI-modified SA aerogel. The plentiful active PEI groups, together with the reduction capabilities of MXene, considerably enhance the adsorption capacity of 3568 mg g^{-1} for CR; this is attributed to robust electrostatic attraction along with the synergistic effects of intercalation and surface adsorption. The results showed that the adsorption process for CR aligned well with the pseudo-second-order kinetic and Langmuir isotherm models. The mechanical strength of the aerogel was greatly enhanced by the double-network structure composed of polymeric PEI and SA, allowing for easy recycling without secondary contamination, with only a slight reduction in capacity following five cycles.[143]

The innovative nanocomposite hydrogel of ZIF-8@IL-MXene/poly(*N*-isopropylacrylamide) (NIPAM), which was fabricated by Xiong and his co-authors, was capable of successfully adsorbing crystal violet (CV) from wastewater (Fig. 15a). The formation of the composite hydrogel IL-MXene/PNIPAM was accomplished through *in situ* polymerization by grafting IL onto the MXene surface and subsequently introducing solutions of NIPAM monomer. This process was completed in a single step. Utilizing the *in situ* formation of ZIF-8 on pore walls of composite hydrogels, ZIF-8@IL-MXene/PNIPAM was produced. The prepared nanocomposite hydrogel displayed a maximum adsorption capacity for CV of 325.03 mg g^{-1} at ambient temperature, with a reduction to 91% following five cycles of adsorption–desorption. The results are in accordance with Freundlich and pseudo-second-order kinetics models, based on several interactions between molecules of adsorbent and hydrogel.[152]

By self-assembling CNTs, CTAB and MXene nanosheets, Ding *et al.* were able to synthesize a unique CMC three-dimensional composite. In order to determine whether or not the material produced could adsorb AO7, CR, and MO, the material was tested. In comparison with CNTs and MXene, the CMC composite had a greater capacity for the adsorption of
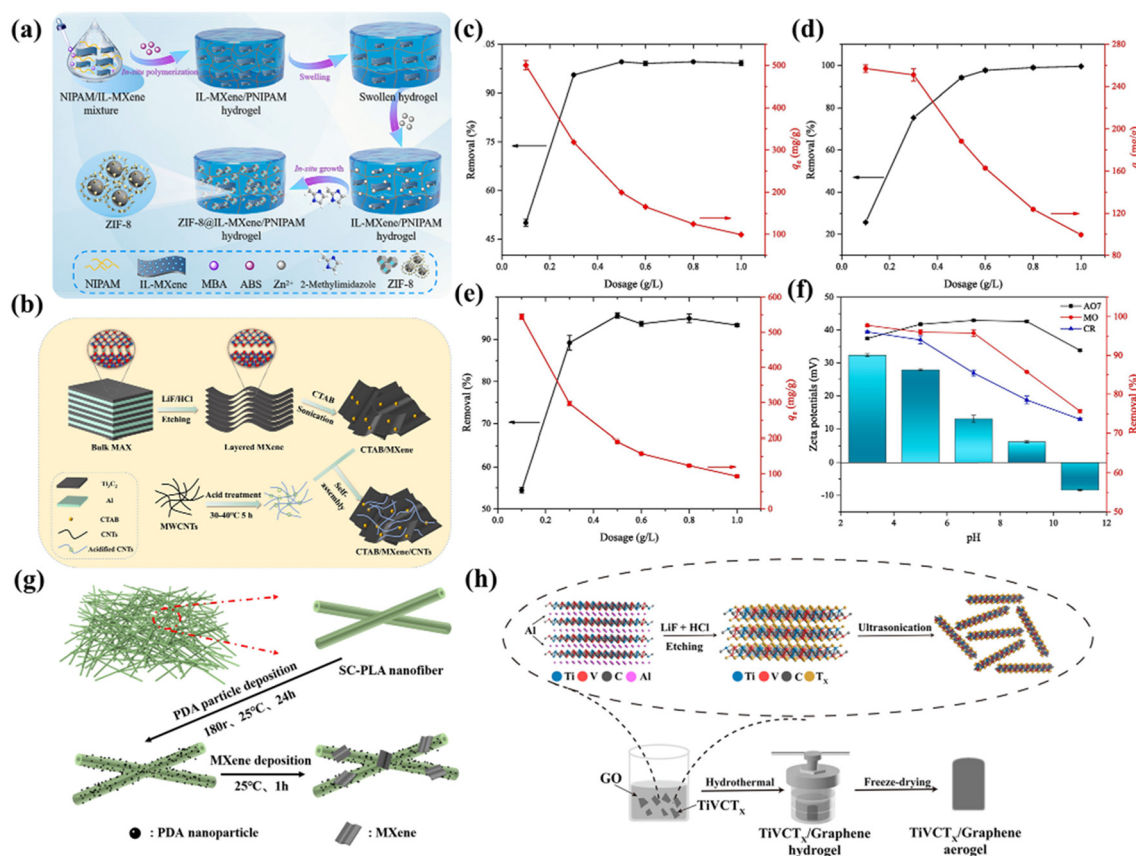
Fig. 15 (a) Schematic illustration of ZIF-8 grown *in situ* in composite hydrogels. Reproduced with permission from ref. 152. Copyright 2024, Elsevier. (b) Scheme of the preparation process for the CMC composite. (c)–(e) Effect of adsorbent dosage on the removal efficiency and adsorption capacity (q_e) of AO7, MO, and CR. (f) Effect of pH on the adsorption and zeta potentials of the CMC composite at different pH values. Reproduced with permission from ref. 153. Copyright 2024, Elsevier. (g) Fabrication procedures for composite fibers. Reproduced with permission from ref. 154. Copyright 2024, Elsevier. (h) Preparation process for TiVCT$_x$/Gas. Reproduced with permission from ref. 156. Copyright 2024, Elsevier.

AO7, CR, and MO with maximum adsorption capacities of 367.9, 628.5, and 294.2 mg g^{-1}, respectively. As the temperature increased, the adsorption capabilities of the CMC composite for AO7 and MO reduced, whereas the adsorption capabilities for CR increased. When it comes to the process of adsorption, the hydrogen bonding, π–π electron–donor–acceptor, and electrostatic interactions were all crucial contributors. The energy distribution of site analysis revealed that the CMC composite possessed more adsorption active sites than MXenes and CNTs. As a result, CMC composites possessed better adsorption capabilities for the anionic dyes that were being studied. It is possible that the changes in adsorption patterns for the anionic dyes can be attributed to the availability of adsorption sites as well as changes to the heterogeneity of the sites on the CMC surface. Based on the findings from the approximate site energy distribution analysis, it was found that the CMC composite had a greater number of adsorption active sites compared to MXene and CNTs. This indicates that the CMC composite possesses a superior adsorption capability for specific anionic dyes. The amount of accessible adsorption sites and the change in site heterogeneity on the CMC surface are two factors that can be attributed to the differences in adsorption behaviors that occur between three anionic dyes from different compounds (Fig. 15b–f).[153]

Wang and co-authors developed an innovative approach for modifying the electrospun polylactic acid fibrous membrane, improving its adaptability for the treatment of wastewater under challenging conditions. PLA fibre membranes were initially coated with PDA, followed by the deposition of MXene facilitated by PDA (Fig. 15g). The as-prepared SC-PLA/PDA/MXene membranes proved effective at MB adsorption, with a maximum adsorption capacity of 434.8 mg g^{-1}. MB adsorption by the membrane aligns closely with the pseudo-second-order kinetic and Langmuir models. The above circumstance also indicates that chemisorption predominates in the MB elimination process. In essence, the membrane and MB molecules exhibit π–π interactions and electrostatic attraction.[154]

Xing *et al.* fabricated TiVCT$_x$ MXene/graphene nanosheet-based aerogels, named TiVCT$_x$/GAs, *via a* simple self-assembly hydrothermal process, followed by freeze-drying (Fig. 15h). Combining bimetallic MXene and graphene aerogel in TiVCT$_x$/GAs provides a remarkable broad-spectrum dye removal capability from wastewater. TiVCT$_x$/GAs effectively adsorb different dyes, with capacities of 319.67, 229.97, 303.45, and 217.87 mg

g^{-1} for MB, CR, RB, and MO, respectively. Kinetics and thermodynamics studies confirm that the process of adsorption follows the pseudo-second-order kinetic and Langmuir adsorption models.[156]

MXene/carbon foam (MCF) hybrid aerogel was synthesized by Li and co-authors using $Ti_3C_2T_x$-MXene and MF. Both cationic and anionic dyes were used to investigate the removal properties of MCF. Several different methods of characterization were utilized in order to examine the physicochemical properties of MCF. Additionally, statistical physics models were utilized in order to gain a deeper comprehension of the dye adsorption mechanism it possessed. MCF was shown to have outstanding adsorptive efficiency against the harmful dyes CR and MB, with adsorption capacities of 647.75 mg g^{-1} and 356.97 mg g^{-1}, respectively. According to the findings, these capacities were better suited for the Langmuir and pseudo-second-order kinetic models. In addition, the saturated multilayer model was utilized in order to explore the molecular process underlying the adsorption systems of MCF-MB and MCF-CR components. Through a process that involved multi-anchoring (303 and 318 K), single connection (333 K), and mixed adsorption orientation, the findings of the numerical simulation demonstrate that MCF adsorbs the MB molecules in the form of dimers. In contrast, CR molecules were adsorbed as monomers through a process that included the mixed adsorption orientation (333 K), multi-anchored and pure non-parallel adsorption directions (303 K and 318 K), and adsorption directions that were not parallel to one another.[157]

Electrostatic self-assembly of 2D MXene nanosheets and biomass-activated carbon was used by Li et al. to reported a heterostructure adsorbent that they referred to as CMAC composite. This was accomplished in the presence of CTAB. This method prevented the re-stacking of MXene nanosheets, which resulted in a reduction in the multilayer plate structure of MXene and an increase in the layer spacing. This resulted in an increase in exposure of accessible active sites, which even more significantly improved the adsorption performance. As a consequence of the tests, it was shown that CMAC possessed an exceptional adsorption efficiency for CR, with adsorption capacities of 1264.032 mg g^{-1}. The Langmuir, intraparticle diffusion and pseudo-second-order kinetic models suit the dye adsorption data well. The adsorption mechanism is attributed to the combination of hydrogen bonding, physical adsorption, and electrostatic interactions.[159]

Li et al. developed a straightforward and eco-friendly foaming technique in order to produce a macroporous cellulose nanocrystal (CNC)/MXene/polyvinyl alcohol (PVA) (C-CMP) foam that possessed exceptional adsorption capabilities. Glutaraldehyde was utilized as a crosslinker to enhance the adsorption effectiveness of MB dye. The adsorption experiment revealed that MB had a maximum adsorption capacity of 239.92 mg g^{-1}. The adsorption performance corresponded well to the Langmuir isotherm and pseudo-second-order kinetic models. Thermodynamic studies showed that the process of adsorption was spontaneous and endothermic. The study demonstrated that the adsorption between MB and C-CMP was due to electrostatic interactions.[160]

5. Mechanism of adsorption fundamentals of MXene-based nano-adsorbents for dyes

When it comes to water filtration, adsorption is among the most effective and economical technologies available. On the basis of variations in the adsorption forces, adsorption is typically divided into two categories: chemical adsorption and physical adsorption. Physical adsorption primarily occurs due to van der Waals forces, which are frequently observed in MXene due to material's large SSA. A number of different processes, including electrostatic interactions, coordination, ion exchange, and hydrogen bonding, are included in chemical adsorption. Due to the fact that Ti–C–O$^-$ or Ti–C–OH$^-$ groups on MXene have the ability to interact with a wide variety of cations, electrostatic contact is a frequent mechanism in the process of the adsorption of MXene. Ion exchange or the development of inner-sphere complexes is encouraged by the presence of a considerable number of functional groups and the stratified structure. There are a variety of factors that influence the adsorption mechanisms of MXenes, including the exact kind of MXene, the properties of pollutants, and the natural aquatic environment. The adsorption mechanism for TiVCT$_x$/GAs, as proposed by Xing et al., is depicted in Fig. 16a. Integrating H-bonding, π–π interactions, and electrostatic attraction significantly influences adsorption. The structural features of TiVCT$_x$/GAs, such as their porous structure with a large SSA and the abundance of adsorption active sites given by bimetallic layers of TiVCT$_x$ and graphene sheets, also help to enhance the ability of TiVCT$_x$/GAs to adsorb MB dye.[156]

Furthermore, Purkayastha and co-authors produced MX-PAN membranes that might bind MB molecules to both F and OH/=O terminating groups of MXene. The molecular structure of MB dye is shown in Fig. 16b. The sulfur (S) or nitrogen (N) atoms in MB, carrying a positive charge, classify it as a cationic dye. After the aluminum atoms are removed from Ti_3AlC_2 (parent powder) via etching, various functional groups (–F and –OH/=O) attach simultaneously on the surface of $Ti_3C_2T_x$, resulting in a negative charge. These negative charges $[Ti–F]^{-1}$ and $[Ti–O]^{-1}$ can be cationic species sensors. As shown in Fig. 16c, MB molecules can interact with both F and OH/=O terminal groups. Therefore, a key mechanism for the adsorption of MB dye is electrostatic interaction between positively charged MB molecules and negatively charged $Ti_3C_2T_x$ MXene.[139]

Wang et al. explained that the adsorption of MG and CR on alk-MXene/ZIF composite could be ascribed to the hydrogen bonding, π–π, and electrostatic interactions. Additionally, the proposed adsorption mechanism is schematically illustrated in Fig. 16d.[149] To further understand the adsorption phenomenon, Li et al. explained the adsorption process of AMXGO for CR and MG, as shown in Fig. 16e. AMXGO dye adsorption involves various phenomena, including π–π conjugates, electrostatic forces, intercalation adsorption, as well as pore adsorption. Among the most significant impacts is the electrostatic force, which is generated by the negative hydroxyl and
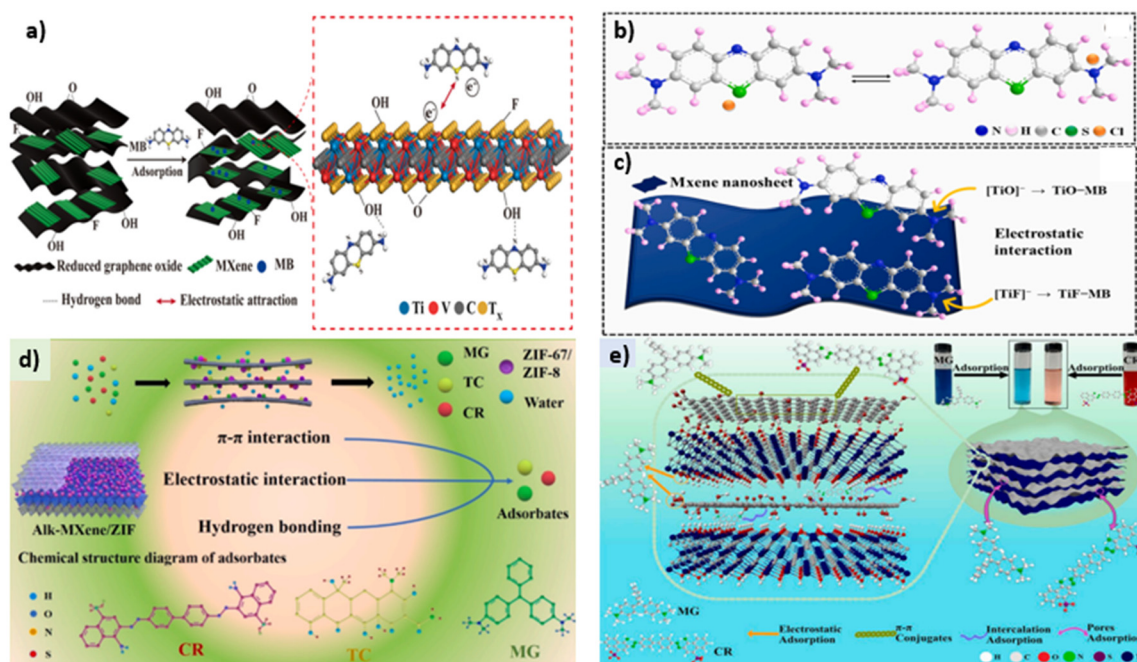
Fig. 16 (a) Schematic illustration of the adsorption mechanism of TiVCT$_x$/Gas. Reproduced with permission from ref. 156. Copyright 2024, American Chemical Society. (b) Molecular structure of MB. Reproduced with permission from ref. 139. Copyright 2023, Elsevier. (c) Schematic illustration of electrostatic interactions between Ti$_3$C$_2$T$_x$ MXene nanosheet and MB dye molecules. Reproduced with permission from ref. 139. Copyright 2023, Elsevier. (d) Schematic diagram of the adsorption mechanism of the alk-MXene/ZIF adsorbent. Reproduced with permission from ref. 149. Copyright 2024, Elsevier. (e) Adsorption mechanism of AMXGO adsorbents for MG and CR. Reproduced with permission from ref. 147. Copyright 2024, Elsevier.

carboxyl groups present on GO lamellae and Alk-MXene surfaces, which mix with cationic molecules. π–π conjugates have a considerable effect on CR adsorption because their structure contains six benzene rings, which is more than the three rings in the structure of the MG molecule. This also describes why AMXGO has superior adsorption efficacy toward anionic CR. Furthermore, the layer-by-layer structure of Alk-MXene and GO flakes in AMXGO favors intercalation adsorption of either CR or MG molecules. Furthermore, the AMXGO samples include numerous mesopores, which ultimately promote pore adsorption of CR and MG.[147]

While the fundamental adsorption mechanisms have been identified, a comprehensive mechanistic framework reveals the relative contributions and synergistic interactions among different adsorption pathways in MXene-based systems.[61] Electrostatic interactions represent the primary driving force for cationic dye adsorption, with mechanistic efficiency directly correlated to surface charge density and zeta potential values. Ti$_3$C$_2$T$_x$ MXenes exhibit highly negative surface charges due to abundant –OH, –O, and –F terminations, creating strong electrostatic fields capable of attracting cationic species over significant distances.[106] Quantitative analysis reveals that the electrostatic contribution accounts for the majority of the total adsorption energy for MB and rhodamine B, while representing a smaller fraction for anionic dyes like CR. pH-dependent studies demonstrate the optimal electrostatic interactions occur at near-neutral pH, where MXene surface deprotonation

maximizes the negative charge density while maintaining structural stability. π–π stacking mechanisms show high selectivity toward aromatic dye molecules, with an interaction strength proportional to the aromatic ring number and electron density distribution. Computational studies using density functional theory (DFT) calculations reveal significant binding energies for benzene ring interactions with Ti$_3$C$_2$T$_x$ surfaces, with substantially higher energies for multi-ring systems like CR. Distance-dependent analysis shows that optimal π–π interactions occur at specific separations, with a parallel orientation providing maximum orbital overlap. MXene surface hybridization enhances π-electron delocalization, creating favorable interaction sites for aromatic dye molecules.[161]

Hydrogen bonding exhibits remarkable complexity in MXene–dye systems, involving multiple donor–acceptor combinations and cooperative strengthening effects. Surface –OH and –O groups serve as hydrogen bond acceptors, while dye amino groups (–NH$_2$) and hydroxyl functionalities act as donors.[162] Spectroscopic analysis (FTIR and NMR) reveals moderate hydrogen bond strengths for individual interactions, with significantly enhanced cumulative effects for dyes with multiple bonding sites. Temperature-dependent studies show that hydrogen bonding contributions decrease substantially at elevated temperatures, indicating entropy-driven weakening of directional interactions. Ion exchange processes demonstrate high specificity toward charge-to-size ratios and hydration energies of exchangeable species.[163] Ti$_3$C$_2$T$_x$ interlayer cations

exhibit different exchange affinities for organic cations, with the following selectivity series: quaternary ammonium > primary ammonium > metal cations. Kinetic analysis reveals two-stage exchange processes: rapid surface exchange followed by slower interlayer diffusion. Stoichiometric studies confirm equivalent exchange ratios for monovalent dye cations, while multivalent species show complex exchange behaviors involving charge compensation mechanisms.

Physical adsorption through pore filling becomes dominant for microporous MXene derivatives and high molecular weight dyes. Pore size distribution analysis reveals optimal dye accommodation in mesopores, where molecular diffusion remains unrestricted while surface interactions are maximized. Molecular dynamics simulations demonstrate size-selective adsorption, with larger dye molecules showing reduced diffusion rates and surface-limited adsorption.[64] Multiple mechanisms operate simultaneously in real adsorption systems, creating cooperative enhancement effects that exceed individual contributions. Electrostatic pre-concentration brings dye molecules into proximity with MXene surfaces, facilitating secondary interactions including π–π stacking and hydrogen bonding. Computational analysis reveals cooperative binding energies significantly higher than additive individual contributions, indicating synergistic stabilization. Sequential mechanism analysis shows that electrostatic interactions dominate initial adsorption, followed by π–π stacking at intermediate saturation and pore filling at high saturation. Solution pH dramatically influences the mechanism prevalence and adsorption efficiency through surface chemistry modifications and dye speciation changes.[164]

Acidic conditions enhance protonation of the MXene surface groups, reducing electrostatic attractions but increasing hydrogen bonding opportunities. Alkaline conditions maximize electrostatic interactions but may destabilize MXene structures through excessive deprotonation. Thermal analysis reveals differential temperature dependencies among adsorption mechanisms, with electrostatic interactions showing minimal temperature dependence, while hydrogen bonding decreases significantly at elevated temperatures. Multi-component systems reveal mechanism-dependent selectivity patterns, with different dyes competing for specific interaction sites, indicating moderate to intense competition depending on the degree of overlap between mechanisms. This comprehensive mechanistic framework offers quantitative insights into MXene–dye interactions, facilitating the rational design of high-performance adsorbents through targeted mechanism optimization and synergistic enhancement strategies.

6. Regeneration and recyclability of adsorbents

Adsorbents, such as MXene, used for dye adsorption should be recyclable and regenerative due to their practical and sustainable environmental applications. Several approaches have been established to recover the adsorption ability of dye-loaded MXene adsorbents for reuse.[141] Thermal regeneration

comprises heating the adsorbents to encourage the desorption of dyes that have been absorbed. Chemical regeneration uses regenerants like alkalis, acids, organic solvents, or complexing agents to desorb the dyes from the adsorbent surface specifically.[165,166] Another approach is electrochemical regeneration, which uses an electrical potential to accelerate desorption with the advantage of selectivity and *in situ* regeneration. When the regenerant solution and dye-loaded adsorbents are mixed, and suitable desorption conditions are sustained, batch systems can perform these processes. The effectiveness of regeneration is evaluated based on the amount of dye removed and the recovery of adsorption capacity. MXene adsorbents' long-term viability as cost-efficient and sustainable solutions for dye removal applications is partially due to their effective regeneration and recyclability.[84,167]

For instance, the recyclability of $Ti_3C_2T_x$/NiFeMn-LDH@Gel was demonstrated after recycling five times and it was observed that the removal ratio of $Ti_3C_2T_x$/NiFeMn-LDH@Gel for CR adsorption remained at 71.72%, displaying the effective regeneration property for $Ti_3C_2T_x$/NiFeMn-LDH@Gel, as shown in Fig. 17a.[146] Likewise, the cycling stability of $TiVCT_x$/GAs, as illustrated in Fig. 17b, highlights its remarkable performance in dye adsorption applications. Over five cycles of the absorption–squeezing process, the material consistently maintains a high absorption capacity, indicating its durability and effectiveness at removing contaminants from wastewater.[156] The utilization of $NaHCO_3$ solution as a desorption agent for PHGC/MXene/AB93 results in a negligible reduction in the adsorption capacity of PHGC/MXene for AB93, even following 12 cycles of adsorption and desorption. The elimination rate is around 94% (Fig. 17c), with variations not exceeding 1.5%. Upon utilizing hydrochloric acid solution as a desorption agent for PHGC/MXene/MB, the PHGC/MXene's adsorption capacity for MB decreases by a minimal amount after 12 cycles of adsorption and desorption, while the efficiency of removal remains consistently higher than 97% (Fig. 17d). The results suggest that the removal rate decreases by at least 3% throughout the course of twelve cycles in comparison with its highest value. This suggests that PHGC/MXene hydrogel excels in both alkaline and acidic environments, demonstrating its versatility. In the case of PHGC/MXene/AB93 and PHGC/MXene/MB, respectively, solutions of sodium bicarbonate and hydrochloric acid demonstrate effective desorption characteristics. As a result, PHGC/MXene hydrogel is a stable, efficient, and renewable adsorbent that may be utilized for the treatment of wastewater that contains AB93 or MB.[135]

7. Comparative insights into the advantages and limitations of $Ti_3C_2T_x$ MXene in dye adsorption and photocatalytic applications

A comprehensive analysis of $Ti_3C_2T_x$ MXene variants and their performance characteristics is presented in Table 2, highlight-
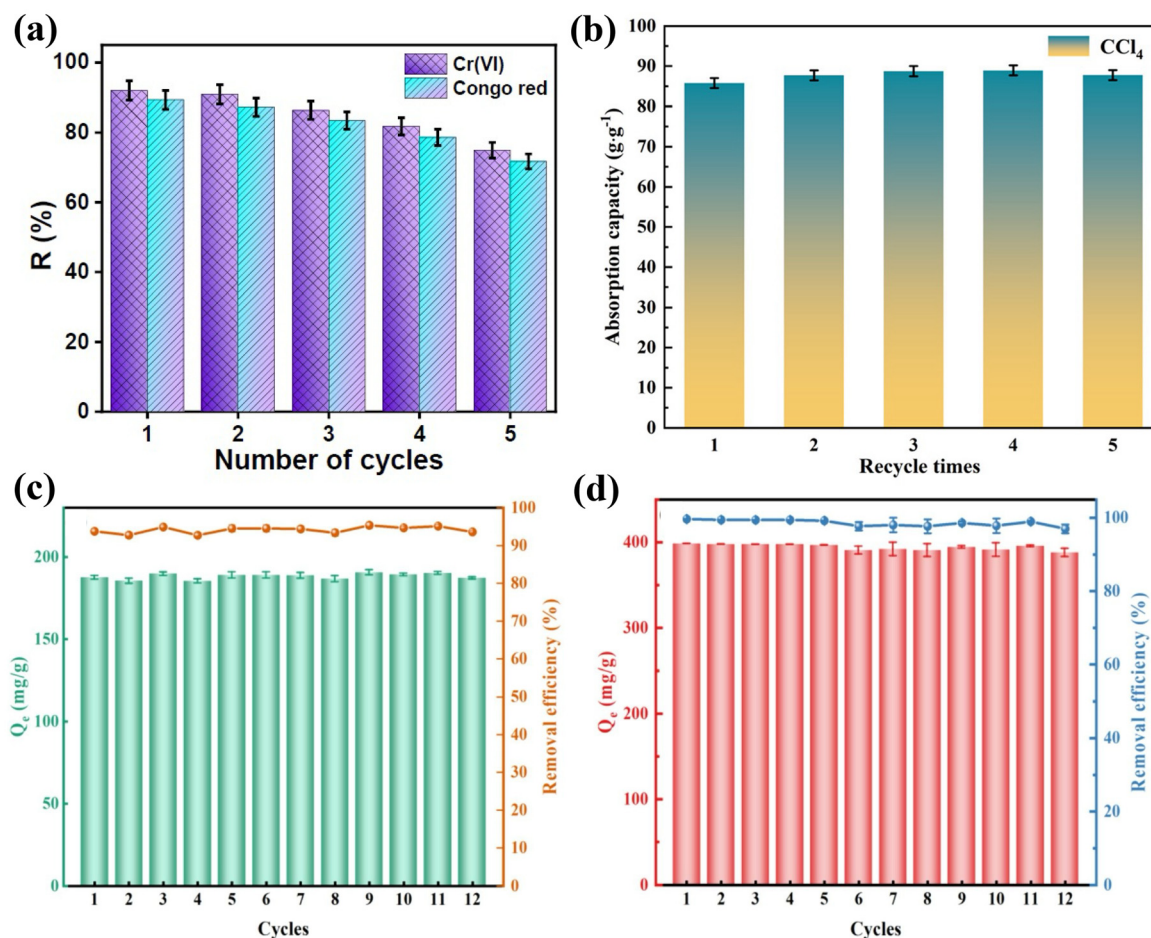
Fig. 17 Reusability tests for (a) $Ti_3C_2T_x$/NiFeMn-LDH@Gel against Cr(VI) and CR. Reproduced with permission from ref. 146. Copyright 2024, Elsevier. (b) $TiVCT_x$/Gas against CCl_4. Reproduced with permission from ref. 156. Copyright 2024, American Chemical Society. Studies on the regeneration of (c) AB93 and (d) MB by PHGC/MXene. Reproduced with permission from ref. 135. Copyright 2024, Elsevier.

ing both positive insights and critical limitations across different modification strategies. $Ti_3C_2T_x$ MXene represents a groundbreaking milestone as the first reported MXene system for dye removal and photocatalysis applications, establishing the foundation for an entire class of 2D materials in environmental remediation. The material exhibits exceptional electrostatic interaction capabilities with cationic dyes, particularly MB, by leveraging its inherent negative surface charge and rich surface chemistry to achieve a strong binding affinity. This electrostatic mechanism proves highly effective for irreversible adsorption, indicating robust dye–MXene interactions that prevent desorption under mild conditions.[128]

Photocatalytic versatility emerges as a distinctive advantage, with $Ti_3C_2T_x$ exhibiting effective UV-driven dye degradation for both MB and AB80, demonstrating dual functionality beyond conventional adsorbents. The heterogeneous adsorption behavior, confirmed through excellent Freundlich model fitting, indicates the presence of multiple binding sites with varying energies, providing flexibility in accommodating diverse dye molecules. This multi-site adsorption mechanism contributes to the material's broad applicability across different dye classes and concentrations.[128] Performance enhancement through strategic modifications demonstrates remarkable capabilities through surface functionalization strategies that dramatically amplify the $Ti_3C_2T_x$ performance. Alkali treatments using NaOH, LiOH, and KOH achieve remarkable improvements, with NaOH-treated $Ti_3C_2T_x$ demonstrating an exceptional adsorption capacity of 189 mg g^{-1} for MB, representing a nearly five-fold increase over the pristine material. This enhancement stems from interlayer spacing expansion (up to 29% increase) and surface chemistry modification through fluoride-to-hydroxyl group conversion (–F → –OH), creating more favorable binding sites.[129] Fluoride-free synthesis approaches using $NaBF_4$/HCl represent a significant advancement,[130] producing h-Ti_3C_2 with a superior surface area (44.6 vs. 8.9 m^2 g^{-1}) and enhanced exfoliation characteristics. This environmentally safer synthesis route eliminates hazardous HF usage while achieving better performance for MB adsorption, addressing both environmental concerns and performance requirements. The compliance of modified systems with the Langmuir model indicates a transition to monolayer adsorption, suggesting a more uniform distribution of binding sites.

Table 2 Key strengths and limitations of $Ti_3C_2T_x$ MXene for dye adsorption and photocatalysis

MXene	Positive insights	Negative insights
$Ti_3C_2T_x$ [128]	• First report on MXene for dye removal & photocatalysis • High MB adsorption *via* electrostatic interactions • Effective UV-driven dye degradation (MB & AB80) • Strong binding (irreversible adsorption) • Good fit with Freundlich model (heterogeneous sites)	• Poor stability in water; oxidises to TiO_2 • No toxicity or environmental safety data • Moderate adsorption capacity ($\sim$39 mg g^{-1}) • Complex mechanisms; needs further clarification • No real wastewater or reuse tests
NaOH/LiOH/KOH–$Ti_3C_2T_x$ [129]	• Alkali treatment (NaOH, LiOH) increased interlayer spacing (up to 29%) • Surface functionalisation (–F $\rightarrow$ –OH) improved adsorption capacity • NaOH–$Ti_3C_2T_x$ showed highest MB adsorption capacity (189 mg g^{-1}) • Follows Langmuir model, indicating monolayer adsorption • Faster dye removal rates compared to untreated MXene	• No data on reusability or long-term performance • Lack of toxicity and safety assessment • Some variants (*e.g.* KOH–$Ti_3C_2T_x$) showed lower capacity due to agglomeration • Intercalation effects not uniform; morphology-dependent performance
h-Ti_3C_2 [130]	• Developed a fluoride-free, HF-free hydrothermal synthesis route using $NaBF_4$/HCl • Resulting MXenes (h-Ti_3C_2, h-Nb_2C) had higher surface areas and better exfoliation • Improved adsorption performance for MB over HF-etched MXenes • Larger interlayer spacing and higher BET surface area (44.6 *vs.* 8.9 m^2 g^{-1}) • Broader applicability: method extended to Nb_2C MXene synthesis	• No reusability or recyclability tests conducted • No quantification of maximum adsorption capacity (only removal % shown) • Performance tested only for MB; limited scope (*e.g.* no heavy metals, real water) • No mechanistic insight into selectivity or adsorption modelling (*e.g.* isotherms) • Adsorption only moderate ($\sim$24 mg g^{-1} for MB) compared to other MXenes
Nb_2CT_x [131]	• High specific surface area ($\sim$44.69 m^2 g^{-1}) and layered morphology support efficient adsorption • Very high adsorption capacities: MB = 526 mg g^{-1}, MO = 500 mg g^{-1} • Follows pseudo-second-order kinetics, indicating chemisorption at active sites • Faster adsorption for MB (99% removal in 5–11 min) • Excellent efficiency for both cationic and anionic dyes	• No data on regeneration, recyclability, or real wastewater testing • Adsorption isotherms (Langmuir, Freundlich) did not fit well; mechanistic modelling limited • Slight surface oxidation observed; long-term MXene stability not assessed
PAA_2 alk-MXene [132]	• Adsorbent showed high adsorption capacities of 264.46 mg g^{-1} for CR and 193.92 mg g^{-1} for MB • Adsorption followed the Langmuir isotherm and pseudo-second-order kinetics • The material retained its adsorption efficiency after multiple cycles • Surface functionalisation introduced beneficial –COOH and –OH groups and increased interlayer spacing	• The study did not evaluate performance in real wastewater or multi-component dye systems • Toxicity or leaching of components was not assessed • Only two dyes (MB and CR) were tested, limiting the generality of the findings
Ti_3C_2–SO_3H [133]	• Functionalisation with sulfonic groups increased adsorption capacity from 21.10 mg g^{-1} to 111.11 mg g^{-1} • Adsorption followed Langmuir isotherm and pseudo-second-order kinetics • Adsorption capacity reached 723.35 mg g^{-1} with increased MB concentration • Surface chemistry and interlayer spacing were enhanced through diazonium modification	• No regeneration or recyclability testing was conducted • The study only tested MB; no multicomponent or real wastewater systems • Safety and environmental aspects were not addressed • Adsorbent stability and scalability were not discussed
MXene-COOH@(PEI/PAA)$_n$ [134]	• Adsorption followed pseudo-second-order kinetics and Langmuir isotherm (monolayer adsorption) • Good selectivity and performance across three dyes (MB, ST, NR) • Composites are easily separable and structurally stable	• Adsorption tested only in single dye systems, not in complex wastewater • Decline in adsorption capacity upon recycling may limit long-term use • Synthesis and LbL process may be time-consuming on the industrial scale
PHGC/MXene [135]	• PHGC/MXene hydrogel exhibited pH-responsive selectivity, with adsorption capacities of 555.56 mg g^{-1} for MB and 207.47 mg g^{-1} for AB93 • High reusability and performance across acidic and alkaline conditions	• No real wastewater or multi-dye solution testing was conducted • Potential biodegradability or leaching behaviour of MXene was not assessed

Table 2 (Contd.)

MXene	Positive insights	Negative insights
Cetyltrimethylammonium bromide-modified multi-layered $Ti_3C_2T_x$ MXene (CMM)[136]	• The system demonstrated rapid adsorption and strong ionic dye interaction • High adsorption capacity: up to 213.00 mg g^{-1} • Effective in a broad pH range, especially at pH 3 • Adsorption follows Langmuir isotherm and pseudo-second-order kinetics • Mechanisms include electrostatic attraction, π–cation interaction, and hydrogen bonding • Maintains functionality in the presence of common co-existing ions	• Toxicity and environmental compatibility remain unexplored • Surface area decreased after CTAB modification (from 5.02 to 2.06 m^2 g^{-1}) • No biological toxicity or environmental risk data provided • Decreased adsorption efficiency after multiple reuse cycles
ABC/MX composite[137]	• Electrostatic attraction, reduction, chelation, hydrogen bonding • Excellent selectivity and ion interference resistance • Thermally enhanced adsorption (endothermic; capacity ↑ with temperature) • Stable for real-world application: minimal impact from co-ions and long-term storage	• Cr(VI) regeneration is limited due to MXene oxidation • No cytotoxicity or leaching data; safety in biomedical or food applications not assured • Performance slightly affected by HPO_4^{2-} due to competitive adsorption • MXene's known susceptibility to oxidation may limit long-term use in oxidative environments • Complex DFT-supported adsorption models require experimental validation in multicomponent matrices
MXene-PEI[138]	• Fast adsorption kinetics: equilibrium within 20–60 min • Mechanisms: electrostatic attraction, redox reaction (Cr(VI) → Cr(III)), π–π stacking, hydrogen bonding • Thermally and mechanically stable structure • Effective even in the presence of competing ions • Easy handling and reusability due to aerogel form	• No biological toxicity evaluation for MXene oxidation products or long-term exposure • Oxidation of MXene over cycles not deeply discussed • Desorption agents (ethanol, NaOH) could impact cost or scalability • No real wastewater or multi-contaminant system testing
MX-PAN membrane[139]	• Fast kinetics: equilibrium achieved in 30–60 min • Mechanisms: electrostatic interactions, hydrogen bonding, π–π interactions, redox transformation • Excellent mechanical strength and porosity from aerogel architecture • Effective in the presence of co-existing ions (Cl$^-$, SO_4^{2-}, CO_3^{2-}) • Scalable and sustainable fabrication method using wood waste and green chemistry	• No biological or environmental toxicity validation of MXene degradation products • Oxidation stability of MXene during long-term use not addressed • Real wastewater validation not included • Performance slightly decreased with coexisting PO_4^{3-} ions
TMAOH delaminated $Ti_3C_2T_x$ MXene nanosheets[142]	• Exceptional adsorption capacity of 1026 mg g^{-1} at 318 K, among the highest reported for MXenes • Fast adsorption kinetics, reaching equilibrium in 10 min • Mechanism confirmed: electrostatic interaction and ion exchange (TMA$^+$ ↔ MB$^+$) dominate • Highly dispersible suspension prevents restacking, ensuring active surface availability • High performance in MNM (membrane form): up to 96% removal efficiency with good dye flux (52 L m^{-2} h^{-1} at 0.6 mg cm^{-2} loading) • Good tolerance to pH range (2–10) and monovalent salts	• Performance decreases in the presence of multivalent cations (Ca^{2+}, Al^{3+}) due to competition and electrostatic shielding • Adsorption capacity decreases slightly after several reuse cycles due to partial loss and delamination damage • No real wastewater or biological testing provided, performance in complex matrices remains unproven • Freeze-drying reduces performance, dry-state materials are less effective due to aggregation
alk-MXene/CoFe$_2$O$_4$/CS[144]	• Ultra-high adsorption capacities achieved: 2095.9 mg g^{-1} for CR, 1333.9 mg g^{-1} for rhodamine B, and 537.6 mg g^{-1} for Malachite Green, among the highest reported for similar adsorbents • The system demonstrated versatility in removing both cationic and anionic dyes simultaneously with rapid kinetics (equilibrium within 60–120 min) and excellent magnetic separability	• Limited recyclability scope with significant capacity loss for anionic dyes (34% loss for CR vs. <20% for cationic dyes) indicating preferential performance toward cationic species • No environmental safety assessment conducted, and complex multi-step synthesis process involving multiple components (alkalized MXene, CoFe$_2$O$_4$, chitosan) may limit practical scalability and cost-effectiveness

Table 2 (Contd.)

MXene	Positive insights	Negative insights
MXene (Ti_3C_2)/Fe_3O_4 [145]	• Multiple synergistic mechanisms including electrostatic interactions, π–π stacking, and hydrogen bonding provided comprehensive dye removal capability with good structural stability after cycling • Temperature-enhanced performance with 91.93% removal efficiency at 55 °C compared to lower temperatures, demonstrating excellent high-temperature adsorption capability (11.68 mg g^{-1} maximum capacity) • The system exhibited superparamagnetic properties (20.3 emu g^{-1}) enabling easy magnetic separation and recovery from aqueous solutions with good stability (zeta potential −48 mV)	• Limited scope with testing only on single cationic dye (MB) and no comprehensive evaluation across different dye types or real wastewater conditions • No recyclability assessment conducted, leaving questions about long-term performance, stability, and practical applicability, with potential concerns about magnetic material leaching and structural integrity over multiple cycles
AMXGO[147]	• Multiple adsorption mechanisms identified including electrostatic attraction, hydrogen bonding (Ti–OH···N), and surface interactions, with temperature-dependent mechanism shifts from physisorption (25 °C) to chemisorption (55 °C) • Ultra-high adsorption capacities: 1111.6 mg g^{-1} for MG and 1133.7 mg g^{-1} for CR, among highest for MXene-based adsorbents • Excellent versatility with >92% removal for both cationic and anionic dyes, plus selective separation capability • Multiple adsorption mechanisms with 3.5× surface area increase compared to pristine MXene	• Limited real-world testing – only synthetic single-dye solutions, not actual industrial wastewater • Complex multi-step synthesis and long equilibrium times (24–48 h) limit scalability and cost-effectiveness
ZIF-8@IL-MXene/PNIPAM[152]	• First hydrogel achieving simultaneous high-efficiency adsorption of phenols, dyes, and metal ions (198.40, 325.03, and 285.65 mg g^{-1}, respectively) • Excellent mechanical properties withstanding ten repeated compressions without damage • 100× increase in specific surface area through ZIF-8 incorporation • Novel ionic liquid grafting approach for MXene stabilization and functionality	• Complex multi-step synthesis requiring precise control of ZIF-8 growth conditions and IL grafting • Significant decrease in Cu^{2+} regeneration efficiency (29% after 5 cycles) due to irreversible chelation • Limited scalability due to multiple synthesis stages and specialized materials (ionic liquids, ZIF-8 precursors) • Reduced swelling ratios with ZIF-8 growth potentially limiting accessibility to binding sites
SC-PLA/PDA/MXene membrane[154]	• Outstanding dual functionality combining excellent oil/water separation and organic dye adsorption capabilities • High flux performance with maximum water flux of 3009.2 L (m^2 h)$^{-1}$ and oil flux of 6397.9 L (m^2 h)$^{-1}$ for pure liquids • Exceptional MB adsorption capacity of 434.8 mg g^{-1} following the Langmuir model • Excellent photothermal conversion ability enhancing separation efficiency under light irradiation (water flux: 9428.4 L (m^2 h)$^{-1}$, oil flux: 12 498.1 L (m^2 h)$^{-1}$) • Superior amphiphilic properties enabling effective separation of different emulsion types (oil-in-water and water-in-oil) • Novel polydopamine-assisted MXene deposition strategy ensuring uniform distribution and stable attachment • Simultaneous removal capability for both oil and organic pollutants in single-step process • Ultrahigh oil/water separation efficiency of 99.12% with excellent selectivity	• Complex multi-step synthesis involving electrospinning, polydopamine self-polymerization, and MXene deposition requiring precise control • Limited long-term stability assessment under continuous industrial operating conditions • Gradual performance decline in oil flux during extended cycling due to irreversible pore blocking by residual oil • Temperature and light dependency for optimal performance may limit operational flexibility in varying environmental conditions • No comprehensive economic analysis or cost-effectiveness evaluation compared to conventional separation methods • Limited testing on real industrial wastewater with complex compositions – most studies conducted using synthetic solutions • Potential scalability challenges for large-scale industrial applications not thoroughly addressed • Performance optimization requires specific conditions (pH, temperature, light irradiation), which may complicate real-world implementation

Table 2 *(Contd.)*

MXene	Positive insights	Negative insights
	• Good mechanical properties with tensile strength above 4.5 MPa maintaining structural integrity	• Incomplete removal during regeneration treatment leading to gradual accumulation of contaminants affecting long-term performance
TiVCT$_x$/GAs[156]	• Outstanding broad-spectrum removal capabilities: 319.67, 303.45, 229.97, 217.87, and 283.38 mg g^{-1} for MB, RhB, CR, MO, and TCH, respectively	• Complex multi-step synthesis involving hydrothermal treatment, freeze-drying, and hazardous HF acid for MXene preparation
	• Superior performance compared to other adsorbents in comparative analysis	• Limited long-term stability assessment with only 5-cycle regeneration study
	• Excellent compatibility with harsh environments including wastewater containing multiple dyes/drugs and inorganic salts	• Performance dependency on pH, temperature, and light conditions may limit operational flexibility
	• Remarkable photothermal conversion ability reaching 95.0 °C within 1 min under sunlight irradiation	• No comprehensive economic analysis or cost-effectiveness evaluation provided
	• Large absorption capacity for oils and solvents ranging from 40–90 g g^{-1}	• Mostly tested on synthetic wastewater rather than real industrial effluents
	• Spontaneous and endothermic adsorption process following Langmuir model and pseudo-second-order kinetics	• Endothermic nature requires higher temperatures for optimal performance, which may increase operational costs

Chemical functionalization through sulfonic acid modification (Ti_3C_2–SO_3H) showcases a dramatic capacity enhancement from 21.10 to 111.11 mg g^{-1}, with a concentration-dependent performance reaching 723.35 mg g^{-1} under optimized conditions. This diazonium-mediated surface modification enhances both surface chemistry and interlayer spacing, creating highly active adsorption sites.[133] Surfactant modification using cetyltrimethylammonium bromide (CTAB) achieves a capacity of 213.00 mg g^{-1} while maintaining broad pH tolerance, particularly effective at pH 3.[136] Critical performance limitations and stability challenges reveal that oxidative instability represents the most significant limitation of $Ti_3C_2T_x$ systems, with poor stability in aqueous environments leading to oxidation to TiO_2.[128] This fundamental degradation pathway compromises long-term performance and material integrity, which is particularly problematic for continuous water treatment applications. The oxidation susceptibility extends across all $Ti_3C_2T_x$ variants, indicating a material-level challenge requiring protective strategies or alternative compositions.

The limited adsorption capacity in its pristine form presents significant competitive disadvantages, with the baseline $Ti_3C_2T_x$ achieving only ~39 mg g^{-1}, substantially lower than that of high-performing adsorbents.[128] Even modified variants like h-Ti_3C_2 show a moderate performance (~24 mg g^{-1}), indicating inherent capacity limitations that require extensive modification for competitive performance.[130] Surface area reduction following certain modifications, such as CTAB treatment (5.02 to 2.06 m^2 g^{-1}), demonstrates trade-offs between functionalization and accessible surface area.[136] Mechanistic complexity across $Ti_3C_2T_x$ systems requires further clarification,[128] with multiple interaction pathways including electrostatic attraction, π–cation interactions, hydrogen bonding,[136] and ion exchange contributing to overall performance. This complexity makes performance prediction and optimization

challenging, particularly in multi-component systems where competing interactions may alter dominant mechanisms. Scalability and practical implementation barriers pose significant challenges, particularly due to the complexity of synthesis, which requires multi-step modifications. Alkali treatments,[129] chemical functionalization,[133] and surfactant modifications[136] introduce additional processing steps, chemical consumption, and potential environmental concerns. The time-consuming nature of layer-by-layer assembly and precise control requirements for modification procedures limit industrial scalability and cost-effectiveness.[134]

Regeneration limitations across $Ti_3C_2T_x$ systems present economic and environmental concerns. Decreased adsorption efficiency after multiple reuse cycles, observed in CTAB-modified systems, indicates structural degradation or irreversible binding.[136] Desorption agent requirements (ethanol, NaOH) increase operational costs and waste generation, while incomplete regeneration leads to a gradual decline in performance. Real-world validation gaps represent critical knowledge deficits, with most studies conducted using synthetic single-dye solutions rather than complex industrial wastewaters. Performance degradation in the presence of multivalent cations (Ca^{2+}, Al^{3+}) and competing anions highlights selectivity challenges in realistic water matrices. The lack of comprehensive real wastewater testing limits practical applicability assessment.

Environmental and safety considerations highlight critical research gaps, with the assessment of toxicity and biocompatibility representing urgent needs. No systematic evaluation of $Ti_3C_2T_x$'s environmental impact or human health effects exists, while the toxicity of oxidation products, leaching behavior, and long-term environmental fate remain uncharacterized, raising concerns about its widespread deployment. Surface modification agents, such as CTAB and sulfonic acid groups,

introduce additional chemical complexity, requiring safety evaluation. Environmental concerns surrounding HF-based synthesis necessitate safer alternatives, with fluoride-free routes showing promise but requiring further optimization.[130] Waste generation from synthesis processes and regeneration procedures requires a comprehensive life cycle assessment to evaluate their overall environmental impact. Challenges associated with disposing of spent MXene materials and their oxidation products necessitate a systematic investigation.

Future directions and innovation opportunities suggest that enhancing oxidative stability represents the highest priority research direction, requiring protective coating strategies, alloy composition optimization, or control of operational conditions. Encapsulation approaches, such as those using protective polymer layers or composite formation with stable matrices, could address degradation issues while maintaining functional performance. Performance optimization strategies should focus on synergistic modification approaches combining interlayer engineering, surface functionalization, and morphological control. AI-guided design can accelerate composition–structure–property relationship discoveries, enabling the rational optimization of $Ti_3C_2T_x$ variants for specific applications. Scale-up engineering focusing on continuous flow systems, automated synthesis procedures, and regeneration optimization will bridge the laboratory-to-industry gap. Economic feasibility studies incorporating material costs, pro-

cessing requirements, and performance benefits are essential for commercial viability assessment. Comprehensive environmental impact evaluation through life cycle assessment will guide sustainable development and regulatory compliance for $Ti_3C_2T_x$-based water treatment technologies.

8. Benchmarking MXene-based adsorbents against established materials for sustainable dye remediation

To compare performance and demonstrate MXenes' potential in wastewater treatment, Table 3 provides a detailed quantitative comparison of 2D MXenes with well-known adsorbents, including MOFs, COFs, activated carbon, graphene-based materials, and CNTs for dye removal. The data, sourced from peer-reviewed studies between 2004 and 2024, highlight the outstanding adsorption abilities of MXene-based adsorbents under various conditions. TMAOH–$Ti_3C_2T_x$ achieved the highest adsorption capacity of 1026 mg g^{-1} for MB, a 2.5 times increase over that of commercial activated carbon (400 mg g^{-1}) and a significant edge over GO (250–300 mg g^{-1}) and multi-walled CNTs (400 mg g^{-1}) in similar settings.[142,168] Likewise, MXene/biomass activated carbon composites showed excellent

Table 3 Adsorption capacities of MXenes *vs.* conventional adsorbents for organic dyes

Adsorbent material	Dye	Adsorption capacity (mg g^{-1})	Contact time	pH	Temp. (°C)	Initial conc. (mg L^{-1})
MXenes (2D transition metal carbides)						
TMAOH–$Ti_3C_2T_x$[142]	MB	1026	Rapid	7	45	100
$Ti_3C_2T_x$@sodium alginate[171]	MB	969	60 min	10	25	300
$Ti_3C_2T_x$/carbon foam[157]	MB	357	120 min	7	30	200
$Ti_3C_2T_x$/carbon foam[157]	CR	648	120 min	7	30	300
MXene/biomass AC[159]	CR	>1400	180 min	7	25	500
NaOH–$Ti_3C_2T_x$[129]	MB	189	120 min	7	25	100
$Ti_3C_2T_x$/loofah carbon[169]	MB	175	60 min	7	25	200
$Ti_3C_2T_x$/loofah carbon[169]	CR	93	60 min	7	25	150
Activated carbon						
Commercial PAC (Norit)[168]	MB	400	120 min	6–7	25	200
Commercial PAC (Norit)[168]	CR	500	120 min	6–7	25	250
Tea seed shell AC[172]	MB	325	180 min	6–7	25	200
Water-activated AC[173]	MB	149	5 min	6.5–7	25	100
Palm kernel shell AC[174]	MB	15	60 min	7	25	100
Ashitaba waste AC[175]	CR	200–300	180 min	7	25	200
Walnut shell AC[175]	MB	150–200	180 min	7	25	150
Graphene-based materials						
Graphene oxide[176]	MB	250–300	60 min	7	25	100
Graphene oxide[175]	Rhodamine B	200–250	60 min	7	25	100
GO–AC composite[177]	MB	300–400	120 min	7	25	200
CNTs						
Multi-walled CNTs[168]	MB	400	120 min	6–7	25	200
Multi-walled CNTs[168]	CR	500	120 min	6–7	25	250
Functionalized CNTs[178]	MB	350–450	90 min	7	25	150
Metal–organic frameworks (MOFs)						
ZIF-67/GO composite[179]	Malachite green	250–350	180 min	7	25	200
Al-based MOF[180]	MB	180–250	120 min	7	25	100
MOF-199[181]	Various odorants	22.6 ± 42.3	60 min	7	25	Variable
Covalent organic frameworks (COFs)						
TpStb–SO$_3$Na COF[170]	Cationic dyes	400–500	60 min	7	25	200
Various COFs[182]	MB	200–400	120 min	7	25	100–300

performance for CR, removing over 1400 mg g^{-1}, much higher than that of commercial activated carbon (500 mg g^{-1}) and functionalized CNTs (500 mg g^{-1}).[159,169] MXenes' best performance comes from their unique dual adsorption process, which includes surface adsorption and intercalation, along with abundant surface functional groups (–OH, =O, –F), and adjustable surface chemistry that fosters strong electrostatic interactions with both cationic and anionic dyes. MXenes show quick kinetics, reaching equilibrium in 5–120 min *versus* 60–300 min for traditional adsorbents, and they can be reused with over 90% efficiency after multiple cycles. Although MOFs and COFs perform well in some cases, like TpStb–SO$_3$Na COF achieving high capacities for certain cationic dyes, MXenes offer greater versatility, faster kinetics, and wider applicability across diverse dye types and conditions, making them the most promising new adsorbents for sustainable wastewater treatment.[170]

9. Challenges, recommendations and future perspectives

Although MXene-based materials are often employed to remove dyes from the environment, studies on these materials are still in their initial phases due to numerous problems encountered by researchers. The theoretical concept of using MXene-based materials has expanded faster, but the experimental aspect remains slower. However, several challenging issues still need to be carefully considered. In order to realize their real-world relevance and commercial viability in large-scale water treatment applications, it will be necessary to take steps toward scaling up MXenes and nanocomposites based on MXene.

Current MXene-based dye removal technologies operate at Technology Readiness Level (TRL) 3–4, as characterized by laboratory-scale proof-of-concept and component validation in controlled environments.[61] While fundamental adsorption mechanisms are well-understood and performance optimization has been demonstrated in synthetic solutions, significant gaps remain in real-world validation, system integration, and scalable manufacturing processes.[183] Real wastewater performance presents the most critical challenge, as industrial effluents contain complex mixtures of organic contaminants, salts, suspended particles, heavy metals, and fluctuating pH that can drastically reduce MXene's adsorption capacity and selectivity compared to single-component laboratory studies. Fouling mechanisms from biological waste, organic matter, and inorganic scaling result in surface deactivation and pore blockage, reducing the recyclable capacity over operational cycles.[90] Cost and scalability barriers arise from expensive, hazardous synthesis methods using HF or LiF/HCl, with material costs of $50–200 kg^{-1} compared to $1–10 kg^{-1} for conventional adsorbents.[184] Environmental impact assessment through life cycle analysis (LCA) reveals carbon footprints of 5–15 kg CO$_2$ equivalent per kg MXene, primarily from energy-intensive synthesis processes.[103] Advancement to TRL 6–7

requires pilot-scale demonstrations, comprehensive techno-economic analysis, and the development of green synthesis alternatives to establish commercial feasibility.

Several vital areas require attention to fully harness the capabilities of MXene-based materials in dye removal and other applications:

1. Improvements in the etching procedure: traditional etching methods for synthesizing MXenes often employ hazardous chemicals that can harm the environment. Therefore, exploring and creating more ecologically friendly techniques for the etching process are critical. This transition could make MXene production safer and more sustainable and increase its appeal for industrial applications in which environmental restrictions are growing more stringent.

2. Research on toxicity: another critical area of exploration is the potential toxicity of MXene-based materials. Understanding how these materials interact with the environment and human health is essential, especially for therapeutic applications. Comprehensive studies assessing the biocompatibility and environmental impact of MXenes will help establish safety protocols and regulatory frameworks, ensuring their responsible use in various applications, including medicine and environmental remediation.

3. Surface characterization: the surface characteristics of MXene-based materials play a significant role in their adsorption abilities. Gaining a deeper understanding of these properties, including surface area, functional groups, and morphology, can lead to modifications that enhance their performance in dye removal. Tailoring the surface chemistry of MXenes could optimize their interaction with various dye molecules, thereby improving their efficiency as adsorbents (Fig. 18).

4. Lifespan of recycled materials and advanced integration strategies: finally, further research is needed to evaluate the lifespan and reusability of recycled MXene-based materials in real applications. Understanding how these materials degrade over time and how they operate after several cycles of usage is critical to determine their feasibility in long-term applications. Investigating and creating methods for the regeneration of MXenes could considerably improve their use in various applications, including wastewater treatment, energy storage, and sensing technologies. Integrating AI and ML can transform the development of MXene materials. These technologies may be utilized to forecast material degradation trends, enhance synthesis procedures, and formulate more effective recycling methods. ML models may evaluate massive datasets to discover trends and recommend ideal settings for material regeneration, therefore eliminating trial-and-error experimentation.

5. Performance in real wastewater: the majority of MXene research has been carried out using artificial dye solutions in controlled lab settings. Real wastewater streams, on the other hand, are far more complicated and frequently include a combination of organic contaminants, salts, suspended particles, heavy metals, and fluctuating pH. These conflicting elements have the potential to drastically lower MXenes' adsorption capability and selectivity. Therefore, assessing MXene-based
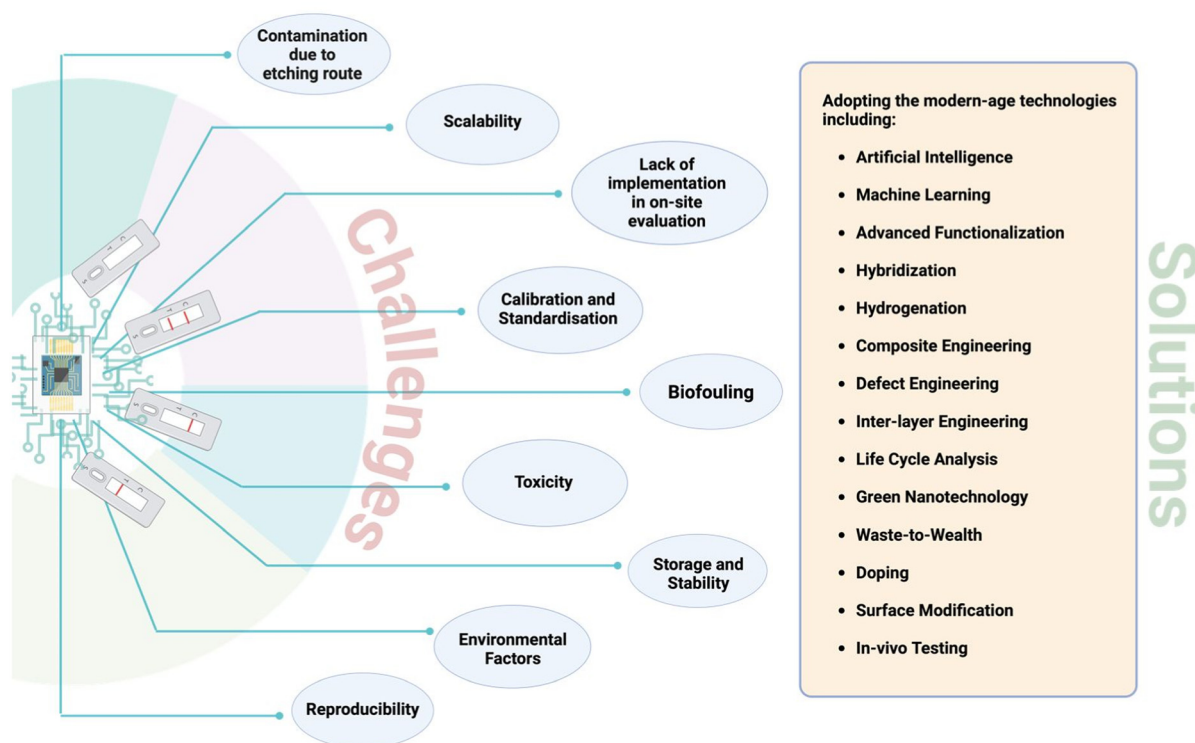
Fig. 18 Challenges and solutions for employing MXene-based materials in the adsorption of dyes.

systems in realistic wastewater environments must be a top priority for future research in order to confirm their resilience, effectiveness, and longevity.

6. Fouling and long-term stability: MXenes are prone to fouling from biological wastes, organic matter, and other wastewater particles, which can result in surface deactivation, pore blockage, and decreased recyclable capacity. To ensure constant performance over several cycles, fouling must be addressed *via* surface functionalization, hybrid coating techniques, or integration with antifouling polymers. Additionally, MXene degradation under extended exposure to aquatic environments, particularly under variable redox conditions, remains a significant but little-studied problem.

7. Cost and scalability: top-down etching techniques that use dangerous chemicals like HF or LiF/HCl are among the current MXene production methods that are expensive, dangerous, and challenging to scale. Additionally, purification and post-synthesis delamination processes require a lot of energy and time. To move MXene manufacturing from the laboratory to commercial scale, it will be essential to develop low-cost, scalable, and environmentally friendly synthesis methods, such as electrochemical etching, green exfoliation processes, and continuous flow systems.

8. Environmental impact and sustainability: MXenes are intriguing prospects for green remediation solutions, but their total environmental impact must be carefully evaluated. To assess energy use, chemical use, emissions, and end-of-life disposal or recyclability, LCA studies are crucial. To guarantee environmental and regulatory compliance, issues with leach-

ing, nanoparticle release, and ecotoxicity should also be addressed using thorough risk assessment frameworks. Furthermore, performing a LCA is essential for identifying the environmental impacts of MXene-based materials throughout their life span, from synthesis to disposal. Such a technique guarantees that the materials are sustainable and effective, in agreement with the overall green chemistry initiatives. Evaluating the LCA would make MXenes more attractive for firms embracing eco-friendly technology.

For biomedical and environmental applications, *in vivo* cytotoxicity analysis is significant in determining the toxicity of MXenes. Such tests would ensure the safer use of MXenes in real-world applications, such as sensing and wastewater treatment, and guarantee no risk to human health or ecosystems. Advanced characterization solutions including real-time monitoring capabilities, molecular docking studies, and computational simulation technologies, combined with emerging force measurement techniques and advanced X-ray methodologies, could significantly improve the activity and reusability assessment of the MXene system. Force measurement approaches, particularly atomic force microscopy (AFM) and nanoindentation techniques, enable precise quantification of interfacial interactions between MXene surfaces and target molecules, providing critical insights into adsorption mechanisms at the nanoscale. These force-based methodologies can map surface heterogeneity, measure adhesion forces, and characterize the evolution of mechanical properties during cycling processes, offering an unprecedented understanding of structure–property relationships in MXene systems.[185]

Although MXene-based materials hold great promise for environmental applications, addressing these challenges through focused research will be crucial for translating theoretical advancements into practical solutions. By improving synthesis methods, assessing toxicity, understanding surface properties, and evaluating lifespan, the full potential of MXenes can be realized, paving the way for innovative approaches for dye removal and other environmental challenges. Despite years of investigation of MXenes, these materials are still in their early phases of development. Standardization is still required to produce MXene, an attractive material with stable characteristics, including higher biocompatibility, uniform dispersion, prolonged strength, and higher efficiency compared to other 2D materials.[61] Industry–academia collaboration is essential for developing large-scale MXene-based materials, including encapsulated adsorbents, membranes, and electrodes, with increased hazardous removal efficiency. This will enable the production and deployment of low-cost MXene-based adsorbent solutions for wastewater treatment in residential and commercial areas.

Artificial intelligence (AI), machine learning (ML) and complex physics based data modelling technologies offer transformative potential for advancing MXene-based water treatment systems through multiple specific applications.[186] ML algorithms can predict optimal MXene compositions and surface functionalization strategies by analyzing structure–property relationships from experimental datasets, with density functional theory (DFT) calculations combined with ML models enabling the screening of thousands of potential MXene variants to identify high-performance candidates before experimental synthesis.[187] Gaussian process regression and random forest algorithms have been successfully applied to predict adsorption capacities based on surface area, functional group density, and interlayer spacing parameters,[188] while neural network models can optimize synthesis conditions, including etching time, temperature, and chemical concentrations to achieve target material properties.[189] Support vector machine (SVM) and artificial neural network (ANN) models demonstrate capability for predicting dye removal efficiency based on water quality parameters including pH, ionic strength, competing ions, and dye concentrations,[190] with ensemble learning methods such as XGBoost and random forest showing superior accuracy at predicting breakthrough curves and saturation points for MXene-based filtration systems.[191]

Real-time process optimization represents another critical application area, where adaptive control algorithms integrated with IoT sensor networks enable dynamic optimization of treatment parameters.[192] Reinforcement learning agents can continuously adjust flow rates, pH levels, and regeneration cycles based on real-time performance feedback, while digital twin models combining physics-based simulations with ML algorithms provide predictive maintenance capabilities and optimal operational strategies.[193,194] Deep learning architectures including convolutional neural networks (CNNs) can analyze microscopy images to predict material degradation and performance decline over operational cycles,[195] with computer vision systems powered by deep learning enabling effluent quality analysis through spectroscopic data interpretation. Time-series forecasting models using LSTM networks predict treatment system performance and identify potential failures before critical thresholds are reached,[196] while anomaly detection algorithms monitor unusual patterns in adsorption behavior that may indicate material degradation or system malfunction.

5G technology enables ultra-low latency communication between distributed sensor networks and central control systems, facilitating real-time optimization of multiple treatment units, while edge computing capabilities enable on-site ML inference for immediate decision-making without cloud dependency.[197,198] IoT sensors equipped with selective dye detection capabilities provide high-resolution monitoring of specific contaminants, enabling precision treatment protocols that automatically adjust based on real-time water quality parameters.[199] Cloud-based platforms integrate multi-site data for comprehensive performance analysis and predictive modeling, with blockchain technology ensuring data integrity and traceability for regulatory compliance and performance verification. Specific implementation examples include predictive maintenance models that analyze pressure drop patterns, flow rate variations, and energy consumption trends to schedule optimal regeneration cycles, and multi-objective optimization algorithms that balance treatment efficiency, energy consumption, and operational costs to minimize total system expenses.[200]

Future prospects include quantum machine learning algorithms that may accelerate the discovery of materials by exploring vast chemical spaces more efficiently than classical computers, automated laboratory systems guided by AI algorithms conducting high-throughput synthesis and screening experiments with minimal human intervention, and integration of genomics data with ML models to predict ecological impacts and optimize MXene designs for environmental compatibility.[201] Federated learning frameworks enable collaborative model training across multiple treatment facilities while preserving data privacy and proprietary information, while augmented reality interfaces provide operators with real-time system status and maintenance guidance through smart glasses and mobile applications.[202] This comprehensive AI/ML integration represents a paradigm shift toward intelligent water treatment systems that continuously learn, adapt, and optimize their performance, ultimately enabling more efficient, cost-effective, and sustainable MXene-based environmental remediation technologies capable of autonomous operation and predictive performance optimization across diverse water treatment scenarios.

10. Conclusion

In conclusion, MXenes are demonstrated to be an emerging class of promising two-dimensional adsorbents for the adsorption of various dyes in an aqueous environment. There are various methods for synthesizing MXenes. Presently, the top-down method involving hydrofluoric acid etching is the most

commonly used method. Although this approach is less expensive, there is more environmental harm risk. Their high surface areas, active surface terminal groups, hydrophilicity, and distinct combination of layered structures result in excellent adsorption properties. However, oxidative and aggregative properties make effective adsorption and regeneration difficult. As a result, further modifications are needed. Surface modification, blending, and stripping are some modification methods for MXenes. Blending, in particular, can improve the adsorption efficiency, stability, oxidation resistance, hydrophilicity, and other essential features of MXene materials.

This review has highlighted substantial developments in the design and fabrication of MXene-based adsorbents, their adsorption capacity, their physicochemical properties, and adsorption mechanisms of MXenes, including chemical, physical, and electrostatic interactions for the removal of toxic dyes from the aqueous environment. Overall, MXenes are a cutting-edge advance in water treatment, providing an alternative route to more sustainable and effective solutions for dye-contaminated water. Furthermore, with the integration of modern technologies such as IoT, AI, ML, complexities science, network analysis and 5G communications, MXene-based nanosorbents have the potential to be next-generation material-based intelligent environmental technologies that form smart and connected societies and cities.

Conflicts of interest

The authors declare no conflicts of interest.

Abbreviations

2D	Two dimensional
3D	Three dimensional
AA	Acrylic acid
AB93	Methyl blue
AI	Artificial intelligence
BC	Bacterial cellulose
BD	Benzidine
BET	Brunauer–Emmett–Teller
CDCs	Carbon-derived carbides
CNTs	Carbon nanotubes
COF	Covalent organic framework
CR	Congo Red
CTAB	Cationic surfactant solution
CVD	Chemical vapor deposition
DASNP	Dialdehyde starch nanoparticles
DBM	Direct brown M
DBRN	Direct black RN
DMSO	Dimethyl sulphoxide
EDX	Energy-dispersive X-ray
FTIR	Fourier-transform infrared spectroscopy
GPa	Gigapascals
GO	Graphene oxide

HRTEM	High-resolution transmission electron microscopy
IL	Ionic liquid
LCA	Life cycle assessment
LDH	Layered double hydroxides
MB	Methylene blue
MG	Malachite Green
ML	Machine learning
MO	Methyl orange
MOF	Metal–organic framework
MPa	Megapascals
NMs	Nanofiber membranes
PA	*p*-Phenylenediamine
PAN	Polyacrylonitrile
PDA	Polydopamine
PEI	Polyethylenimine
PEPLD	Plasma-enhanced pulsed laser deposition
PLA	Polylactic acid
rGO	Reduced graphene oxide
RhB	Rhodamine B
ROS	Reactive oxygen species
SA	Sodium alginate
SAED	Selected area electron diffraction
SEM	Scanning electron microscopy
SSA	Specific surface area
SSbD	Safe and sustainable by design
TAPB	1,3,5-Tris(4-aminophenyl) benzene
TMAOH	Tetramethylammonium hydroxide
TP	1,3,5-Triformylphloroglucinol
UN	United Nations
XPS	X-ray photoelectron spectroscopy
XRD	X-ray diffraction
ZIF	Zeolitic imidazolate framework

Data availability

No primary research results, software or code have been included and no new data were generated or analysed as part of this review.

Acknowledgements

References

1 A. Khosla, Sonu, H. T. A. Awan, K. Singh, Gaurav, R. Walvekar, Z. Zhao, A. Kaushik, M. Khalid and V. Chaudhary, *Adv. Sci.*, 2022, **9**, 2203527, DOI: **10.1002/advs.202203527**.

2 D. Pathania, S. Kumar, P. Thakur, V. Chaudhary, A. Kaushik, R. S. Varma, H. Furukawa, M. Sharma and A. Khosla, *Sci. Rep.*, 2022, **12**, 11431, DOI: **10.1038/s41598-022-14984-3**.

3 Sonu and V. Chaudhary, *ECS Sens. Plus*, 2022, **1**, 043401, DOI: **10.1149/2754-2726/ac92ed**.

4 S. Shekhar, A. K. Yadav, A. Khosla and P. R. Solanki, *ECS Sens. Plus*, 2022, **1**, 043602, DOI: **10.1149/2754-2726/ac9227**.

5 T. Suzuki, T. Hidaka, Y. Kumagai and M. Yamamoto, *Nat. Immunol.*, 2020, **21**, 1574–1585, DOI: **10.1038/s41590-020-0802-6**.

6 T. T. T. Toan and D. M. Nguyen, *ECS Sens. Plus*, 2022, **1**, 021604, DOI: **10.1149/2754-2726/ac8436**.

7 C. Valli Nachiyar, A. D. Rakshi, S. Sandhya, N. Britlin Deva Jebasta and J. Nellore, *Case Stud. Chem. Environ. Eng.*, 2023, 7, 100339, DOI: **10.1016/j.cscee.2023.100339**.

8 J. Blair, G. Rathee, A. Puertas-Segura, L. M. Pérez and T. Tzanov, *Environ. Res.*, 2025, **279**, 121783, DOI: **10.1016/j.envres.2025.121783**.

9 G. Rathee, H. Chugh, S. Kohli, R. K. Gaur and R. Chandra, *Mater. Adv.*, 2023, **4**, 1456–1472, DOI: **10.1039/d2ma01081j**.

10 H. Sable, V. Kumar, V. Singh, S. Rustagi, S. Chahal and V. Chaudhary, *Coord. Chem. Rev.*, 2024, **518**, 216079, DOI: **10.1016/j.ccr.2024.216079**.

11 Y. Zhou, J. Lu, Y. Zhou and Y. Liu, *Environ. Pollut.*, 2019, **252**, 352–365, DOI: **10.1016/j.envpol.2019.05.072**.

12 E. F. D. Januário, T. B. Vidovix, N. d. C. L. Beluci, R. M. Paixão, L. H. B. R. da Silva, N. C. Homem, R. Bergamasco and A. M. S. Vieira, *Sci. Total Environ.*, 2021, **789**, 147957, DOI: **10.1016/j.scitotenv.2021.147957**.

13 Y. Pan, S. Sanati, R. Abazari, A. Jankowska, J. Goscianska, V. Srivastava, U. Lassi and J. Gao, *Coord. Chem. Rev.*, 2025, **522**, 216231, DOI: **10.1016/j.ccr.2024.216231**.

14 S. X. Chin, K. S. Lau, S. Zakaria, C. H. Chia and C. Wongchoosuk, *Polymers*, 2022, **14**, 5165, DOI: **10.3390/polym14235165**.

15 P. V. Nidheesh, M. Zhou and M. A. Oturan, *Chemosphere*, 2018, **197**, 210–227, DOI: **10.1016/j.chemosphere.2017.12.195**.

16 L. Bilińska and M. Gmurek, *Water Resour. Ind.*, 2021, **26**, 100160, DOI: **10.1016/j.wri.2021.100160**.

17 S. Khamparia and D. K. Jaspal, *Front. Environ. Sci. Eng.*, 2017, **11**, 8, DOI: **10.1007/s11783-017-0899-5**.

18 A. K. Verma, R. R. Dash and P. Bhunia, *J. Environ. Manage.*, 2012, **93**, 154–168, DOI: **10.1016/j.jenvman.2011.09.012**.

19 S. Thakur and M. S. Chauhan, *Water Quality Management: Select Proceedings of ICWEES-2016*, 2018, pp. 117–129. DOI: **10.1007/978-981-10-5795-3_11**.

20 M. M. Hassan and C. M. Carr, *Chemosphere*, 2018, **209**, 201–219, DOI: **10.1016/j.chemosphere.2018.06.043**.

21 P. Moradihamedani, *Polym. Bull.*, 2022, **79**, 5659–5675, DOI: **10.1007/s00289-021-03603-2**.

22 S. Sarkar, N. T. Ponce, A. Banerjee, R. Bandopadhyay, S. Rajendran and E. Lichtfouse, *Environ. Chem. Lett.*, 2020, **18**, 1569–1580, DOI: **10.1007/s10311-020-01021-w**.

23 M. Hasanpour and M. Hatami, *J. Mol. Liq.*, 2020, **309**, 113094, DOI: **10.1016/j.molliq.2020.113094**.

24 M. Khatami and S. Iravani, *Comment. Inorg. Chem.*, 2021, **41**, 213–248, DOI: **10.1080/02603594.2021.1922396**.

25 K. T. Kubra, M. S. Salman and M. N. Hasan, *J. Mol. Liq.*, 2021, **328**, 115468, DOI: **10.1016/j.molliq.2021.115468**.

26 M. Naushad, A. A. Alqadami, A. A. Al-Kahtani, T. Ahamad, M. R. Awual and T. Tatarchuk, *J. Mol. Liq.*, 2019, **296**, 112075, DOI: **10.1016/j.molliq.2019.112075**.

27 C. Cai, R. Wang, S. Liu, X. Yan, L. Zhang, M. Wang, Q. Tong and T. Jiao, *Colloids Surf., A*, 2020, **589**, 124468, DOI: **10.1016/j.colsurfa.2020.124468**.

28 R. Xing, W. Wang, T. Jiao, K. Ma, Q. Zhang, W. Hong, H. Qiu, J. Zhou, L. Zhang and Q. Peng, *ACS Sustainable Chem. Eng.*, 2017, **5**, 4948–4954, DOI: **10.1021/acssuschemeng.7b00343**.

29 G. Rathee, A. Puertas-Segura, J. Blair, J. Rathee and T. Tzanov, *Prog. Mater. Sci.*, 2025, **150**, 101403, DOI: **10.1016/j.pmatsci.2024.101403**.

30 G. Rathee, N. Singh and R. Chandra, *ACS Omega*, 2020, **5**, 2878–2888, DOI: **10.1021/acsomega.9b03785**.

31 G. Rathee, S. Kohli, A. Awasthi, N. Singh and R. Chandra, *RSC Adv.*, 2020, **10**, 18595–18605, DOI: **10.1039/d0ra02766a**.

32 G. Rathee, A. Awasthi, D. Sood, R. Tomar, V. Tomar and R. Chandra, *Sci. Rep.*, 2019, **9**, 16225, DOI: **10.1038/s41598-019-52849-4**.

33 M. J. K. Ahmed and M. Ahmaruzzaman, *J. Water Process Eng.*, 2016, **10**, 39–47, DOI: **10.1016/j.jwpe.2016.01.014**.

34 M. Ahmaruzzaman, *Adv. Colloid Interface Sci.*, 2011, **166**, 36–59, DOI: **10.1016/j.cis.2011.04.005**.

35 S. A. Khan, D. Hussain, N. Abbasi and T. A. Khan, *Chemosphere*, 2022, **289**, 133232, DOI: **10.1016/j.chemosphere.2021.133232**.

36 S. A. Khan, N. Abbasi, D. Hussain and T. A. Khan, *Langmuir*, 2022, **38**, 8280–8295, DOI: **10.1021/acs.langmuir.2c00702**.

37 K. S. Novoselov, A. K. Geim, S. V. Morozov, D. Jiang, Y. Zhang, S. V. Dubonos, I. V. Grigorieva and A. A. Firsov, *Science*, 2004, **306**, 666–669.

38 L. Y. Yuan, Z. Q. Bai, R. Zhao, Y. L. Liu, Z. J. Li, S. Q. Chu, L. R. Zheng, J. Zhang, Y. L. Zhao, Z. F. Chai and W. Q. Shi, *ACS Appl. Mater. Interfaces*, 2014, **6**, 4786–4796, DOI: **10.1021/am405584h**.

39 R. Ma and T. Sasaki, *Adv. Mater.*, 2010, **22**, 5082–5104, DOI: **10.1002/adma.201001722**.

40 J. N. Coleman, M. Lotya, A. O'Neill, S. D. Bergin, P. J. King, U. Khan, K. Young, A. Gaucher, S. De, R. J. Smith, I. V. Shvets, S. K. Arora, G. Stanton, H. Y. Kim,

K. Lee, G. T. Kim, G. S. Duesberg, T. Hallam, J. J. Boland, J. J. Wang, J. F. Donegan, J. C. Grunlan, G. Moriarty, A. Shmeliov, R. J. Nicholls, J. M. Perkins, E. M. Grieveson, K. Theuwissen, D. W. McComb, P. D. Nellist and V. Nicolosi, *Science*, 2011, **331**, 568–571, DOI: **10.1126/science.1194975**.

41 K. S. Novoselov, A. K. Geim, S. V. Morozov, D. Jiang, M. I. Katsnelson, I. V. Grigorieva, S. V. Dubonos and A. A. Firsov, *Nature*, 2005, **438**, 197–200, DOI: **10.1038/nature04233**.

42 K. V. Wong and B. Bachelier, *J. Energy Resour. Technol.*, 2014, **136**, 021601, DOI: **10.1115/1.4024917**.

43 O. P. Chen, Y. J. Lin, W. Z. Cao and C. T. Chang, *Mater. Lett.*, 2017, **190**, 280–282, DOI: **10.1016/j.matlet.2017.01.030**.

44 S. Wang, H. Sun, H. M. Ang and M. O. Tadé, *Chem. Eng. J.*, 2013, **226**, 336–347, DOI: **10.1016/j.cej.2013.04.070**.

45 F. Perreault, A. Fonseca De Faria and M. Elimelech, *Chem. Soc. Rev.*, 2015, **44**, 5861–5896, DOI: **10.1039/c5cs00021a**.

46 Y. Fan, L. Li, Y. Zhang, X. Zhang, D. Geng and W. Hu, *Adv. Funct. Mater.*, 2022, **32**, 2111357, DOI: **10.1002/adfm.202111357**.

47 F. A. Janjhi, I. Ihsanullah, M. Bilal, R. Castro-Muñoz, G. Boczkaj and F. Gallucci, *Water Resour. Ind.*, 2023, **29**, 100202, DOI: **10.1016/j.wri.2023.100202**.

48 Y. Ibrahim, M. Meslam, K. Eid, B. Salah, A. M. Abdullah, K. I. Ozoemena, A. Elzatahry, M. A. Sharaf and M. Sillanpää, *Sep. Purif. Technol.*, 2022, **282**, 120083, DOI: **10.1016/j.seppur.2021.120083**.

49 I. Ihsanullah and M. Bilal, *Appl. Mater. Today*, 2022, **29**, 101674, DOI: **10.1016/j.apmt.2022.101674**.

50 I. Ihsanullah and M. Bilal, *Chemosphere*, 2022, **303**, 135234, DOI: **10.1016/j.chemosphere.2022.135234**.

51 S. Yu, H. Tang, D. Zhang, S. Wang, M. Qiu, G. Song, D. Fu, B. Hu and X. Wang, *Sci. Total Environ.*, 2022, **811**, 152280, DOI: **10.1016/j.scitotenv.2021.152280**.

52 X. Jiang, A. V. Kuklin, A. Baev, Y. Ge, H. Ågren, H. Zhang and P. N. Prasad, *Phys. Rep.*, 2020, **848**, 1–58, DOI: **10.1016/j.physrep.2019.12.006**.

53 M. Naguib, V. N. Mochalin, M. W. Barsoum and Y. Gogotsi, *Adv. Mater.*, 2014, **26**, 992–1005, DOI: **10.1002/adma.201304138**.

54 Q. Tao, M. Dahlqvist, J. Lu, S. Kota, R. Meshkian, J. Halim, J. Palisaitis, L. Hultman, M. W. Barsoum, P. OÅ. Persson and J. Rosen, *Nat. Commun.*, 2017, **8**, 14949, DOI: **10.1038/ncomms14949**.

55 Y. C. Zhou, X. H. Wang, Z. M. Sun and S. Q. Chen, *J. Mater. Chem.*, 2001, **11**, 2335–2339, DOI: **10.1039/b101520f**.

56 K. Huang, Z. Li, J. Lin, G. Han and P. Huang, *Chem. Soc. Rev.*, 2018, **47**, 5109–5124, DOI: **10.1039/c7cs00838d**.

57 I. Persson, A. el Ghazaly, Q. Tao, J. Halim, S. Kota, V. Darakchieva, J. Palisaitis, M. W. Barsoum, J. Rosen and P.OÅ. Persson, *Small*, 2018, **14**, 1703676, DOI: **10.1002/smll.201703676**.

58 X. Wang, L. Wu, H. Gao and X. Zhang, *Sci. Sin.: Chim.*, 2018, **29**(18), 7633–7644.

59 F. Kong, X. He, Q. Liu, X. Qi, Y. Zheng, R. Wang and Y. Bai, *Electrochim. Acta*, 2018, **265**, 140–150, DOI: **10.1016/j.electacta.2018.01.196**.

60 J. Halim, J. Palisaitis, J. Lu, J. Thörnberg, E. J. Moon, M. Precner, P. Eklund, P. O. A. Persson, M. W. Barsoum and J. Rosen, *ACS Appl. Nano Mater.*, 2018, **1**, 2455–2466, DOI: **10.1021/acsanm.8b00332**.

61 B. Anasori, M. R. Lukatskaya and Y. Gogotsi, *2D metal carbides and nitrides (MXenes) for energy storage*, Jenny Stanford Publishing, 2023, pp. 677–722. DOI: **10.1038/natrevmats.2016.98**.

62 A. Lipatov, H. Lu, M. Alhabeb, B. Anasori, A. Gruverman, Y. Gogotsi and A. Sinitskii, *Sci. Adv.*, 2018, **4**, eaat0491, DOI: **10.1126/sciadv.aat0491**.

63 J. Zhang, N. Kong, S. Uzun, A. Levitt, S. Seyedin, P. A. Lynch, S. Qin, M. Han, W. Yang, J. Liu, X. Wang, Y. Gogotsi and J. M. Razal, *Adv. Mater.*, 2020, **32**, 2070180, DOI: **10.1002/adma.202070180**.

64 V. N. Borysiuk, V. N. Mochalin and Y. Gogotsi, *Nanotechnology*, 2015, **26**, 265705, DOI: **10.1088/0957-4484/26/26/265705**.

65 S. Luo, S. Patole, S. Anwer, B. Li, T. Delclos, O. Gogotsi, V. Zahorodna, V. Balitskyi and K. Liao, *Nanotechnology*, 2020, **31**, 395707, DOI: **10.1088/1361-6528/ab94dd**.

66 Y. Gogotsi, *Matter*, 2022, **5**, 381–384, DOI: **10.1016/j.matt.2021.12.006**.

67 B. Liang, X. Liao, Q. Zhu, M. Yu, J. Li, B. Geng, K. Liu, D. Jia, Z. Yang and Y. Zhou, *Ceram. Int.*, 2021, **47**, 27730–27735, DOI: **10.1016/j.ceramint.2021.06.198**.

68 J. Yin, N. Liu and Y. Gao, *J. Inorg. Mater.*, 2024, **39**(2), 179–185, DOI: **10.15541/jim20230397**.

69 R. Li, L. Zhang, L. Shi and P. Wang, *ACS Nano*, 2017, **11**, 3752–3759, DOI: **10.1021/acsnano.6b08415**.

70 K. Wang, Y. Zhou, W. Xu, D. Huang, Z. Wang and M. Hong, *Ceram. Int.*, 2016, **42**, 8419–8424, DOI: **10.1016/j.ceramint.2016.02.059**.

71 O. Mashtalir, M. Naguib, V. N. Mochalin, Y. Dall'Agnese, M. Heon, M. W. Barsoum and Y. Gogotsi, *Nat. Commun.*, 2013, **4**, 1716, DOI: **10.1038/ncomms2664**.

72 X. H. Zha, J. Yin, Y. Zhou, Q. Huang, K. Luo, J. Lang, J. S. Francisco, J. He and S. Du, *J. Phys. Chem. C*, 2016, **120**, 15082–15088, DOI: **10.1021/acs.jpcc.6b04192**.

73 H. Wang, Y. Wu, J. Zhang, G. Li, H. Huang, X. Zhang and Q. Jiang, *Mater. Lett.*, 2015, **160**, 537–540, DOI: **10.1016/j.matlet.2015.08.046**.

74 C. J. Zhang, B. Anasori, A. Seral-Ascaso, S. H. Park, N. McEvoy, A. Shmeliov, G. S. Duesberg, J. N. Coleman, Y. Gogotsi and V. Nicolosi, *Adv. Mater.*, 2017, **29**, 1702678, DOI: **10.1002/adma.201702678**.

75 X. Tang, X. Guo, W. Wu and G. Wang, *Adv. Energy Mater.*, 2018, **8**, 1801897, DOI: **10.1002/aenm.201801897**.

76 M. Ghidiu, S. Kota, V. Drozd and M. W. Barsoum, *Sci. Adv.*, 2018, **4**, eaao6850, DOI: **10.1126/sciadv.aao6850**.

77 E. S. Muckley, M. Naguib, H. W. Wang, L. Vlcek, N. C. Osti, R. L. Sacci, X. Sang, R. R. Unocic, Y. Xie,

M. Tyagi, E. Mamontov, K. L. Page, P. R. C. Kent, J. Nanda and I. N. Ivanov, *ACS Nano*, 2017, **11**, 11118–11126, DOI: 10.1021/acsnano.7b05264.

78 E. S. Muckley, M. Naguib and I. N. Ivanov, *Nanoscale*, 2018, **10**, 21689–21695, DOI: 10.1039/c8nr05170d.

79 J. Halim, S. Kota, M. R. Lukatskaya, M. Naguib, M. Q. Zhao, E. J. Moon, J. Pitock, J. Nanda, S. J. May, Y. Gogotsi and M. W. Barsoum, *Adv. Funct. Mater.*, 2016, **26**, 3118–3127, DOI: 10.1002/adfm.201505328.

80 G. Ying, S. Kota, A. D. Dillon, A. T. Fafarman and M. W. Barsoum, *FlatChem*, 2018, **8**, 25–30, DOI: 10.1016/j.flatc.2018.03.001.

81 M. Lu, H. Li, W. Han, J. Chen, W. Shi, J. Wang, X. M. Meng, J. Qi, H. Li, B. Zhang, W. Zhang and W. Zheng, *J. Energy Chem.*, 2019, **31**, 148–153, DOI: 10.1016/j.jechem.2018.05.017.

82 T. Voisin, M. D. Grapes, T. T. Li, M. K. Santala, Y. Zhang, J. P. Ligda, N. J. Lorenzo, B. E. Schuster, G. H. Campbell and T. P. Weihs, *Mater. Today*, 2020, **33**, 10–16, DOI: 10.1016/j.mattod.2019.11.001.

83 Y. Ying, Y. Liu, X. Wang, Y. Mao, W. Cao, P. Hu and X. Peng, *ACS Appl. Mater. Interfaces*, 2015, **7**, 1795–1803, DOI: 10.1021/am5074722.

84 A. Shahzad, K. Rasool, W. Miran, M. Nawaz, J. Jang, K. A. Mahmoud and D. S. Lee, *ACS Sustainable Chem. Eng.*, 2017, **5**, 11481–11488, DOI: 10.1021/acssuschemeng.7b02695.

85 M. Bilal, I. Ihsanullah, M. Younas and M. Ul Hassan Shah, *Sep. Purif. Technol.*, 2022, **278**, 119510, DOI: 10.1016/j.seppur.2021.119510.

86 M. Sajid, *Anal. Chim. Acta*, 2021, **1143**, 267–280, DOI: 10.1016/j.aca.2020.08.063.

87 L. P. Yu, L. Lu, X. H. Zhou and L. Xu, *Adv. Mater. Interfaces*, 2023, **10**, 2201818, DOI: 10.1002/admi.202201818.

88 A. Maleki, M. Ghomi, N. Nikfarjam, M. Akbari, E. Sharifi, M. A. Shahbazi, M. Kermanian, M. Seyedhamzeh, E. Nazarzadeh Zare, M. Mehrali, O. Moradi, F. Sefat, V. Mattoli, P. Makvandi and Y. Chen, *Adv. Funct. Mater.*, 2022, **32**, 2203430, DOI: 10.1002/adfm.202203430.

89 Z. Othman, H. R. Mackey and K. A. Mahmoud, *Chemosphere*, 2022, **295**, 133849, DOI: 10.1016/j.chemosphere.2022.133849.

90 C. J. Zhang, S. Pinilla, N. McEvoy, C. P. Cullen, B. Anasori, E. Long, S. H. Park, A. Seral-Ascaso, A. Shmeliov, D. Krishnan, C. Morant, X. Liu, G. S. Duesberg, Y. Gogotsi and V. Nicolosi, *Chem. Mater.*, 2017, **29**, 4848–4856, DOI: 10.1021/acs.chemmater.7b00745.

91 K. Rasool, R. P. Pandey, P. A. Rasheed, S. Buczek, Y. Gogotsi and K. A. Mahmoud, *Mater. Today*, 2019, **30**, 80–102, DOI: 10.1016/j.mattod.2019.05.017.

92 S. P. Sreenilayam, I. Ul Ahad, V. Nicolosi and D. Brabazon, *Mater. Today*, 2021, **43**, 99–131, DOI: 10.1016/j.mattod.2020.10.025.

93 M. Soleymaniha, M. A. Shahbazi, A. R. Rafieerad, A. Maleki and A. Amiri, *Adv. Healthcare Mater.*, 2019, **8**, 1801137, DOI: 10.1002/adhm.201801137.

94 A. M. Jastrzębska, A. Szuplewska, T. Wojciechowski, M. Chudy, W. Ziemkowska, L. Chlubny, A. Rozmysłowska and A. Olszyna, *J. Hazard. Mater.*, 2017, **339**, 1–8, DOI: 10.1016/j.jhazmat.2017.06.004.

95 A. M. JastrzÈ©bska, A. Szuplewska, A. Rozmysłowska-Wojciechowska, M. Chudy, A. Olszyna, M. Birowska, M. Popielski, J. A. Majewski, B. Scheibe, V. Natu and M. W. Barsoum, *2D Mater.*, 2020, **7**, 025018, DOI: 10.1088/2053-1583/ab6a60.

96 W. Wu, H. Ge, L. Zhang, X. Lei, Y. Yang, Y. Fu and H. Feng, *Chem. Res. Toxicol.*, 2020, **33**, 2953–2962, DOI: 10.1021/acs.chemrestox.0c00232.

97 J. Wu, Y. Yu and G. Su, *Nanomaterials*, 2022, **12**, 828, DOI: 10.3390/nano12050828.

98 J. Yoon, S. Kim, K. H. Park, S. Lee, S. J. Kim, H. Lee, T. Oh and C. M. Koo, *Small Methods*, 2023, **7**, 2201579, DOI: 10.1002/smtd.202201579.

99 X. Wu, J. Gong, H. Zhang, Y. Wang and F. Tan, *Sci. Total Environ.*, 2024, **912**, 169227, DOI: 10.1016/j.scitotenv.2023.169227.

100 S. F. Hansen, M. B. Nielsen, L. M. Skjolding, J. Kaur, N. Desivyana, F. Hermansson, J. Bird, S. Barg, A. Khort, I. Odnevall, B. Fadeel and R. Arvidsson, *Sci. Rep.*, 2024, **14**, 31030, DOI: 10.1038/s41598-024-82063-w.

101 G. K. Nasrallah, M. Al-Asmakh, K. Rasool and K. A. Mahmoud, *Environ. Sci.: Nano*, 2018, **5**, 1002–1011, DOI: 10.1039/c7en01239j.

102 Q. Xiang, Z. Wang, J. Yan, M. Niu, W. Long, Z. Ju and X. Chang, *Aquat. Toxicol.*, 2024, **270**, 106904, DOI: 10.1016/j.aquatox.2024.106904.

103 M. Dadashi Firouzjaei, S. K. Nemani, M. Sadrzadeh, E. K. Wujcik, M. Elliott and B. Anasori, *Adv. Mater.*, 2023, **35**, 2300422, DOI: 10.1002/adma.202300422.

104 K. S. Novoselov, D. Jiang, F. Schedin, T. J. Booth, V. V. Khotkevich, S. V. Morozov and A. K. Geim, *Proc. Natl. Acad. Sci. U. S. A.*, 2005, **102**, 10451–10453, DOI: 10.1073/pnas.0502848102.

105 M. S. Cao, Y. Z. Cai, P. He, J. C. Shu, W. Q. Cao and J. Yuan, *Chem. Eng. J.*, 2019, **359**, 1265–1302, DOI: 10.1016/j.cej.2018.11.051.

106 Y. Gogotsi, *Two-dimensional nanocrystals produced by exfoliation of Ti3AlC2*, CRC Press, 2023. DOI: 10.1201/9781003306511-4.

107 J. Liang, C. Ding, J. Liu, T. Chen, W. Peng, Y. Li, F. Zhang and X. Fan, *Nanoscale*, 2019, **11**, 10992–11000, DOI: 10.1039/c9nr02085c.

108 M. Naguib, J. Halim, J. Lu, K. M. Cook, L. Hultman, Y. Gogotsi and M. W. Barsoum, *J. Am. Chem. Soc.*, 2013, **135**, 15966–15969, DOI: 10.1021/ja405735d.

109 R. B. Rakhi, B. Ahmed, M. N. Hedhili, D. H. Anjum and H. N. Alshareef, *Chem. Mater.*, 2015, **27**, 5314–5323, DOI: 10.1021/acs.chemmater.5b01623.

110 Z. Sun, S. Li, R. Ahuja and J. M. Schneider, *Solid State Commun.*, 2004, **129**, 589–592, DOI: 10.1016/j.ssc.2003.12.008.

111 X. Sang, Y. Xie, M. W. Lin, M. Alhabeb, K. L. Van Aken, Y. Gogotsi, P. R. C. Kent, K. Xiao and R. R. Unocic, *ACS Nano*, 2016, **10**, 9193–9200, DOI: 10.1021/acsnano.6b05240.

112 Y. Gogotsi, *Nat. Mater.*, 2015, **14**, 1079–1080, DOI: 10.1038/nmat4386.

113 X. Xiao, H. Yu, H. Jin, M. Wu, Y. Fang, J. Sun, Z. Hu, T. Li, J. Wu, L. Huang, Y. Gogotsi and J. Zhou, *ACS Nano*, 2017, **11**, 2180–2186, DOI: 10.1021/acsnano.6b08534.

114 M. Ghidiu, M. R. Lukatskaya, M. Q. Zhao, Y. Gogotsi and M. W. Barsoum, *Nature*, 2014, **516**, 78–81, DOI: 10.1038/nature13970.

115 A. Lipatov and A. Sinitskii, *2D Metal Carbides and Nitrides (MXenes): Structure, Properties and Applications*, 2019. DOI: 10.1007/978-3-030-19026-2_16.

116 J. Zhao, L. Zhang, X. Y. Xie, X. Li, Y. Ma, Q. Liu, W. H. Fang, X. Shi, G. Cui and X. Sun, *J. Mater. Chem. A*, 2018, **6**, 24031–24035, DOI: 10.1039/c8ta09840a.

117 M. Naguib, R. R. Unocic, B. L. Armstrong and J. Nanda, *Dalton Trans.*, 2015, **44**, 9353–9358, DOI: 10.1039/c5dt01247c.

118 I. R. Shein and A. L. Ivanovskii, *Comput. Mater. Sci.*, 2012, **65**, 104–114, DOI: 10.1016/j.commatsci.2012.07.011.

119 P. Urbankowski, B. Anasori, T. Makaryan, D. Er, S. Kota, P. L. Walsh, M. Zhao, V. B. Shenoy, M. W. Barsoum and Y. Gogotsi, *Nanoscale*, 2016, **8**, 11385–11391, DOI: 10.1039/c6nr02253g.

120 T. Li, L. Yao, Q. Liu, J. Gu, R. Luo, J. Li, X. Yan, W. Wang, P. Liu, B. Chen, W. Zhang, W. Abbas, R. Naz and D. Zhang, *Angew. Chem., Int. Ed.*, 2018, **57**, 6115–6119, DOI: 10.1002/anie.201800887.

121 T. Li, X. Yan, L. Huang, J. Li, L. Yao, Q. Zhu, W. Wang, W. Abbas, R. Naz, J. Gu, Q. Liu, W. Zhang and D. Zhang, *J. Mater. Chem. A*, 2019, **7**, 14462–14465, DOI: 10.1039/C9TA03254A.

122 S. Yang, P. Zhang, F. Wang, A. G. Ricciardulli, M. R. Lohe, P. W. M. Blom and X. Feng, *Angew. Chem., Int. Ed.*, 2018, **57**, 15491–15495, DOI: 10.1002/anie.201809662.

123 M. R. Lukatskaya, J. Halim, B. Dyatkin, M. Naguib, Y. S. Buranova, M. W. Barsoum and Y. Gogotsi, *Angew. Chem., Int. Ed.*, 2014, **53**, 4877–4880, DOI: 10.1002/anie.201403559.

124 W. Sun, S. A. Shah, Y. Chen, Z. Tan, H. Gao, T. Habib, M. Radovic and M. J. Green, *J. Mater. Chem. A*, 2017, **5**, 21663–21668, DOI: 10.1039/c7ta05574a.

125 Z. Zhang, F. Zhang, H. Wang, C. Ho Chan, W. Lu and J. Y. Dai, *J. Mater. Chem. C*, 2017, **5**, 10822–10827, DOI: 10.1039/c7tc03652c.

126 J. Jia, T. Xiong, L. Zhao, F. Wang, H. Liu, R. Hu, J. Zhou, W. Zhou and S. Chen, *ACS Nano*, 2017, **11**, 12509–12518, DOI: 10.1021/acsnano.7b06607.

127 C. Xu, L. Wang, Z. Liu, L. Chen, J. Guo, N. Kang, X. L. Ma, H. M. Cheng and W. Ren, *Nat. Mater.*, 2015, **14**, 1135–1141, DOI: 10.1038/nmat4374.

128 O. Mashtalir, K. M. Cook, V. N. Mochalin, M. Crowe, M. W. Barsoum and Y. Gogotsi, *J. Mater. Chem. A*, 2014, **2**, 14334–14338, DOI: 10.1039/c4ta02638a.

129 Z. Wei, P. Zhang, W. Tian, Q. Xia, Y. Zhang and Z. Sun, *Mater. Chem. Phys.*, 2018, **206**, 270–276, DOI: 10.1016/j.matchemphys.2017.12.034.

130 C. Peng, P. Wei, X. Chen, Y. Zhang, F. Zhu, Y. Cao, H. Wang, H. Yu and F. Peng, *Ceram. Int.*, 2018, **44**, 18886–18893, DOI: 10.1016/j.ceramint.2018.07.124.

131 Y. Yan, H. Han, Y. Dai, H. Zhu, W. Liu, X. Tang, W. Gan and H. Li, *ACS Appl. Nano Mater.*, 2021, **4**, 11763–11772, DOI: 10.1021/acsanm.1c02339.

132 C. Hao, G. Li, G. Wang, W. Chen and S. Wang, *Colloids Surf., A*, 2022, **632**, 127730, DOI: 10.1016/j.colsurfa.2021.127730.

133 Y. Lei, Y. Cui, Q. Huang, J. Dou, D. Gan, F. Deng, M. Liu, X. Li, X. Zhang and Y. Wei, *Ceram. Int.*, 2019, **45**, 17653–17661, DOI: 10.1016/j.ceramint.2019.05.331.

134 K. Li, G. Zou, T. Jiao, R. Xing, L. Zhang, J. Zhou, Q. Zhang and Q. Peng, *Colloids Surf., A*, 2018, **553**, 372–379, DOI: 10.1016/j.colsurfa.2018.05.044.

135 Y. Li, G. Qu, H. Zhang, L. Xie and Y.-F. Zhang, *Chem. Eng. Sci.*, 2024, **300**, 120648, DOI: 10.1016/j.ces.2024.120648.

136 P. Najibikhah and A. Rahbar-Kelishami, *Chemosphere*, 2024, **350**, 141058, DOI: 10.1016/j.chemosphere.2023.141058.

137 Y. Xu, Z. Zhang, Z. Cui, L. Luo, P. Lin, M. Xie, Q. Zhang, B. Sa and C. Wen, *Chem. Eng. J.*, 2024, **488**, 151078, DOI: 10.1016/j.cej.2024.151078.

138 L. Li, X. Y. Shi, T. Huang, N. Zhang and Y. Wang, *J. Mater. Chem. A*, 2023, **11**, 23089–23096, DOI: 10.1039/d3ta04869a.

139 R. Imsong and D. Dhar Purkayastha, *Sep. Purif. Technol.*, 2023, **306**, 122636, DOI: 10.1016/j.seppur.2022.122636.

140 M. Li, P. Zhang, Q. Wang, N. Yu, X. Zhang and S. Su, *Polymers*, 2023, **15**, 2110, DOI: 10.3390/polym15092110.

141 M. Vakili, G. Cagnetta, J. Huang, G. Yu and J. Yuan, *Molecules*, 2019, **24**, 2478, DOI: 10.3390/molecules24132478.

142 L. Zhang, D. Huang, P. Zhao, G. Yue, L. Yang and W. Dan, *Sep. Purif. Technol.*, 2022, **288**, 120718, DOI: 10.1016/j.seppur.2022.120718.

143 Y. Feng, H. Wang, J. Xu, X. Du, X. Cheng, Z. Du and H. Wang, *J. Hazard. Mater.*, 2021, **416**, 125777, DOI: 10.1016/j.jhazmat.2021.125777.

144 R. Wang, H. Cao, C. Yao, C. Peng, J. Qiu, K. Dou, N. Tsidaeva and W. Wang, *Appl. Surf. Sci.*, 2023, **624**, 157091, DOI: 10.1016/j.apsusc.2023.157091.

145 Z. Zhu, M. Xiang, L. Shan, T. He and P. Zhang, *J. Solid State Chem.*, 2019, **280**, 120989, DOI: 10.1016/j.jssc.2019.120989.

146 G. S. Elgarhy, G. M. El-Subruiti, A. M. Omer and A. S. Eltaweil, *J. Mol. Liq.*, 2024, **396**, 123889, DOI: 10.1016/j.molliq.2023.123889.

147 W. Li, J. Tong and G. Li, *Chemosphere*, 2024, **360**, 142376, DOI: 10.1016/j.chemosphere.2024.142376.

148 Y. Zheng, H. Zhang, S. Yu, H. Zhou, W. Chen and J. Yang, *Sep. Purif. Technol.*, 2024, **349**, 127908, DOI: 10.1016/j.seppur.2024.127908.

149 R. Wang, C. Yao, C. Peng, J. Qiu, Q. Wang, X. Liu, J. Meng and W. Wang, *Chem. Eng. J.*, 2024, **485**, 149916, DOI: **10.1016/j.cej.2024.149916**.

150 X. Wang, A. Zhang, M. Chen, M. K. Seliem, M. Mobarak, Z. Diao and Z. Li, *Chem. Eng. J.*, 2023, **473**, 145385, DOI: **10.1016/j.cej.2023.145385**.

151 H. Yang, J. Lin, Z. Wen, Z. Li, J. Zeng, L. Wang, Y. Tao, D. Gao and D. Wang, *Chemosphere*, 2023, **339**, 139797, DOI: **10.1016/j.chemosphere.2023.139797**.

152 Q. Wang, J. Qiao, Y. Xiong, F. Dong and Y. Xiong, *Environ. Res.*, 2024, **242**, 117568, DOI: **10.1016/j.envres.2023.117568**.

153 G. Song, W. Fan, J. Zhang, T. Xue, Y. Shi, Y. Sun and G. Ding, *Appl. Surf. Sci.*, 2024, **661**, 160036, DOI: **10.1016/j.apsusc.2024.160036**.

154 S. Yu Chen, Y. Fan Deng, T. Huang, N. Zhang and Y. Wang, *Sep. Purif. Technol.*, 2024, **328**, 125040, DOI: **10.1016/j.seppur.2023.125040**.

155 A. Bukhari, I. Ijaz, A. Nazir, S. Hussain, H. Zain, E. Gilani, A. A. Alfseisi and H. Ahmad, *RSC Adv.*, 2024, **14**, 3732–3747, DOI: **10.1039/D3RA07250A**.

156 T. Lv, F. Wu, Z. Zhang, Z. Liu, Y. Zhao, L. Yu, J. Zhang, C. Yu, C. Zhao and G. Xing, *ACS Appl. Nano Mater.*, 2024, **7**, 6798–6809, DOI: **10.1021/acsanm.4c00038**.

157 X. Wang, Q. Xu, L. Zhang, L. Pei, H. Xue and Z. Li, *J. Environ. Chem. Eng.*, 2023, **11**, 109206, DOI: **10.1016/j.jece.2022.109206**.

158 I. Ijaz, A. Bukhari, E. Gilani, A. Nazir, H. Zain, A. Bukhari, A. Shaheen, S. Hussain and A. Imtiaz, *Process Biochem.*, 2023, **129**, 239–253, DOI: **10.1016/j.procbio.2023.03.029**.

159 H. Xue, X. Gao, M. K. Seliem, M. Mobarak, R. Dong, X. Wang, K. Fu, Q. Li and Z. Li, *Chem. Eng. J.*, 2023, **451**, 138735, DOI: **10.1016/j.cej.2022.138735**.

160 W. Zhao, H. Chi, S. Zhang, X. Zhang and T. Li, *Molecules*, 2022, **27**, 4243, DOI: **10.3390/molecules27134243**.

161 M. Khazaei, M. Arai, T. Sasaki, C. Y. Chung, N. S. Venkataramanan, M. Estili, Y. Sakka and Y. Kawazoe, *Adv. Funct. Mater.*, 2013, **23**, 2185–2192, DOI: **10.1002/adfm.201202502**.

162 M. A. Hope, A. C. Forse, K. J. Griffith, M. R. Lukatskaya, M. Ghidiu, Y. Gogotsi and C. P. Grey, *Phys. Chem. Chem. Phys.*, 2016, **18**, 5099–5102, DOI: **10.1039/C6CP00330C**.

163 M. R. Lukatskaya, O. Mashtalir, C. E. Ren, Y. Dall'Agnese, P. Rozier, P. L. Taberna, M. Naguib, P. Simon, M. W. Barsoum and Y. Gogotsi, *Science*, 2013, **341**, 1502–1505, DOI: **10.1126/science.1241488**.

164 I. Persson, L.Å Näslund, J. Halim, M. W. Barsoum, V. Darakchieva, J. Palisaitis, J. Rosen and P.OÅ. Persson, *2D Mater.*, 2018, **5**, 015002, DOI: **10.1088/2053-1583/aa89cd**.

165 A. Abdul Ghani, B. Kim, M. Nawaz, K. C. Devarayapalli, Y. Lim, G. Kim and D. S. Lee, *Chem. Eng. J.*, 2023, **467**, 143473, DOI: **10.1016/j.cej.2023.143473**.

166 A. A. Ghani, A. Shahzad, M. Moztahida, K. Tahir, H. Jeon, B. Kim and D. S. Lee, *Chem. Eng. J.*, 2021, **421**, 127780, DOI: **10.1016/j.cej.2020.127780**.

167 M. Xu, C. Huang, J. Lu, Z. Wu, X. Zhu, H. Li, L. Xiao and Z. Luo, *Molecules*, 2021, **26**, 3150, DOI: **10.3390/molecules26113150**.

168 M. Szlachta and P. Wójtowicz, *Water Sci. Technol.*, 2013, **68**, 2240–2248, DOI: **10.2166/wst.2013.487**.

169 T. Lv, J. Zhang, L. Yu, Y. Zhao, T. Zhao, Y. Yang, C. Yu, C. Zhao and G. Xing, *J. Ind. Eng. Chem.*, 2025, **144**, 454–462, DOI: **10.1016/j.jiec.2024.09.040**.

170 R. Li, X. Tang, J. Wu, K. Zhang, Q. Zhang, J. Wang, J. Zheng, S. Zheng, J. Fan, W. Zhang, X. Li and S. Cai, *Chem. Eng. J.*, 2023, **464**, 142706, DOI: **10.1016/j.cej.2023.142706**.

171 Y. Hu, H. Wang, X. Ren, F. Wu, G. Liu, S. Zhang, H. Luo and L. Fang, *Nanomaterials*, 2024, **14**, 1925, DOI: **10.3390/nano14231925**.

172 J. J. Gao, Y. B. Qin, T. Zhou, D. D. Cao, P. Xu, D. Hochstetter and Y. F. Wang, *J. Zhejiang Univ., Sci., B*, 2013, **14**, 650–658, DOI: **10.1631/jzus.B12a0225**.

173 H. M. El-Bery, M. Saleh, R. A. El-Gendy, M. R. Saleh and S. M. Thabet, *Sci. Rep.*, 2022, **12**, 5499, DOI: **10.1038/s41598-022-09475-4**.

174 K. A. Mohamad Said, M. A. M. Amin, I. Yakub, M. R. Rahman, A. B. H. Kueh, S. Hamdan and M. M. Rahman, *BioResources*, 2023, **18**, 5120–5132, DOI: **10.15376/biores.18.3.5120-5132**.

175 Z. Li, H. Hanafy, L. Zhang, L. Sellaoui, M. Schadeck Netto, M. L. S. Oliveira, M. K. Seliem, G. Luiz Dotto, A. Bonilla-Petriciolet and Q. Li, *Chem. Eng. J.*, 2020, **388**, 124263, DOI: **10.1016/j.cej.2020.124263**.

176 N. N. Marnani, F. H. Tezel and O. D. Basu, *Appl. Sci.*, 2024, **14**, 9811, DOI: **10.3390/app14219811**.

177 N. A. Travlou, G. Z. Kyzas, N. K. Lazaridis and E. A. Deliyanni, *Langmuir*, 2013, **29**, 1657–1668, DOI: **10.1021/la304696y**.

178 T. Madrakian, A. Afkhami, M. Ahmadi and H. Bagheri, *J. Hazard. Mater.*, 2011, **196**, 109–114, DOI: **10.1016/j.jhazmat.2011.08.078**.

179 T. Aysu and M. M. Küçük, *Int. J. Environ. Sci. Technol.*, 2015, **12**, 2273–2284, DOI: **10.1007/s13762-014-0623-y**.

180 B. M. Jun, J. Heo, N. Taheri-Qazvini, C. M. Park and Y. Yoon, *Ceram. Int.*, 2020, **46**, 2960–2968, DOI: **10.1016/j.ceramint.2019.09.293**.

181 E. Ahmed, A. Deep, E. E. Kwon, R. J. C. Brown and K. H. Kim, *Sci. Rep.*, 2016, **6**, 31283, DOI: **10.1038/srep31283**.

182 X. Liu, H. Pang, X. Liu, Q. Li, N. Zhang, L. Mao, M. Qiu, B. Hu, H. Yang and X. Wang, *Innovation*, 2021, **2**, 100076, DOI: **10.1016/j.xinn.2021.100076**.

183 I. Ihsanullah, *Chem. Eng. J.*, 2020, **388**, 124340, DOI: **10.1016/j.cej.2020.124340**.

184 M. Alhabeb, K. Maleski, B. Anasori, P. Lelyukh, L. Clark, S. Sin and Y. Gogotsi, *Chem. Mater.*, 2017, **29**, 7633–7644, DOI: **10.1021/acs.chemmater.7b02847**.

185 N. Bhalla, *Adv. Phys. Res.*, 2025, **4**, 2400205, DOI: **10.1002/apxr.202400205**.

186 K. T. Butler, D. W. Davies, H. Cartwright, O. Isayev and A. Walsh, *Nature*, 2018, **559**, 547–555, DOI: **10.1038/s41586-018-0337-2**.

187 G. R. Schleder, A. C. M. Padilha, C. M. Acosta, M. Costa and A. Fazzio, *J. Phys.: Mater.*, 2019, **2**, 032001, DOI: **10.1088/2515-7639/ab084b**.

188 M. Zhong, K. Tran, Y. Min, C. Wang, Z. Wang, C. T. Dinh, P. De Luna, Z. Yu, A. S. Rasouli, P. Brodersen, S. Sun, O. Voznyy, C. S. Tan, M. Askerka, F. Che, M. Liu, A. Seifitokaldani, Y. Pang, S. C. Lo, A. Ip, Z. Ulissi and E. H. Sargent, *Nature*, 2020, **581**, 178–183, DOI: **10.1038/s41586-020-2242-8**.

189 B. Sanchez-Lengeling and A. Aspuru-Guzik, *Science*, 2018, **361**, 360–365, DOI: **10.1126/science.aat2663**.

190 G. Pilania, A. Mannodi-Kanakkithodi, B. P. Uberuaga, R. Ramprasad, J. E. Gubernatis and T. Lookman, *Sci. Rep.*, 2016, **6**, 19375, DOI: **10.1038/srep19375**.

191 C. T. Chen and G. X. Gu, *MRS Commun.*, 2019, **9**, 556–566, DOI: **10.1557/mrc.2019.32**.

192 M. Hamadache, J. H. Jung, J. Park and B. D. Youn, *JMST Adv.*, 2019, **1**, 125–151, DOI: **10.1007/s42791-019-0016-y**.

193 M. Grieves, *White Paper*, 2014, **1**(2014), 1–7.

194 H. Sable, V. Kumar, V. Singh, S. Rustagi, V. Chaudhary and S. Pandit, *J. Electrochem. Soc.*, 2024, DOI: **10.1149/1945-7111/ad32a1**.

195 B. L. Decost and E. A. Holm, *Comput. Mater. Sci.*, 2015, **110**, 126–133, DOI: **10.1016/j.commatsci.2015.08.011**.

196 S. Hochreiter and J. Schmidhuber, *Neural Comput.*, 1997, **9**, 1735–1780, DOI: **10.1162/neco.1997.9.8.1735**.

197 S. Li, L. Da Xu and S. Zhao, *J. Ind. Inf. Integr.*, 2018, **10**, 1–9, DOI: **10.1016/j.jii.2018.01.005**.

198 R. Talreja, H. Sable, V. Chaudhary, S. Kadian, M. Singh, M. kumar, J. kishore, V. Chaudhary and A. Khosla, *ECS Sens. Plus*, 2024, DOI: **10.1149/2754-2726/ad9f7e**.

199 L. Da Xu, W. He and S. Li, *IEEE Trans. Ind. Inform.*, 2014, **10**, 2233–2243, DOI: **10.1109/TII.2014.2300753**.

200 K. Deb, A. Pratap, S. Agarwal and T. Meyarivan, *IEEE Trans. Evol. Comput.*, 2002, **6**, 182–197, DOI: **10.1109/4235.996017**.

201 J. M. Granda, L. Donina, V. Dragone, D. L. Long and L. Cronin, *Nature*, 2018, **559**, 377–381, DOI: **10.1038/s41586-018-0307-8**.

202 A. Dey, M. Billinghurst, R. W. Lindeman and J. E. Swan, *Front. Rob. AI*, 2018, **5**, 37, DOI: **10.3389/frobt.2018.00037**.